POLITECNICO DI MILANO
DEPARTMENT OF MECHANICAL ENGINEERING

Validation of Atomization and Evaporation Models for Fuel Spray in Constant-Volume Experiments Under Non-Reacting Conditions

Supervisor: Dr. Gianluca D'Errico
Professor, Department of Energy,
Politecnico di Milano.

Masters Graduation Thesis by: Sujib Chandra Sutradhar
Matricola: 765095

Academic Year: 2011-2012

To my father, Rabindra Nath Sutradhar

For his continuous support and inspiration in all possible stages in my life

ABSTRACT

In this work, a numerical investigation has been performed to study the atomization and evaporation of a liquid fuel in non reacting conditions in a constant-volume vessel. Work has been carried out using the capabilities of OpenFOAM©code, which provides an open-source framework for 3D-CFD simulations. The spray is modeled with the Eulerian-Lagrangian approach and KHRT break up model was adopted to describe the primary break-up of the liquid-jet under high injection pressures. As a general methodology, this study is based on simulating free *n*-heptane and dodecane sprays injected into a constant volume vessel. A relevant contribution to the availability of suitable and accessible experimental data is represented by the Engine Combustion Network (ECN) database, which is of great interest for model development and validation because of the well-defined boundary conditions and the wide range of conditions employed. In the current work, we perform measurements of jet global quantities such as vapor-phase penetration, liquid-phase penetration over a range of conditions in a high-temperature, high-pressure vessel. The model predictions also produce local mixture fractions and experimental data of the ECN database were used to validate.

Key Words : n-heptane, spary A, KHRT, blob injector, spray penetration, vapor penetration, mixture fraction, ECN, OpenFOAM.

ACKNOWLEDGMENT

The author of this thesis expresses his gratitude towards his supervisor, Dr. Gianluca D'Errico, Associate Professor of the Department of Energy at Politecnico di Milano for giving me the opportunity to conduct this work under his supervision and for his help, valuable advices, inspiration and continuous friendly support throughout the working time of this thesis. The author extends his thanks to Roberto Torelli, PhD student of Department of Energy from the same university for his collegial support, giving advice and helping through hard times of the research and all his co-operation. Being at this department meant having an excellent working environment in both professional and human terms. Thanks to all other PhD students: Andrea, Marco, Luca in the CFD lab of Department of Energy at Polimi for allways creating an enjoyable environment. Thanks to other professors whoever helped me in this thesis work.

Thanks also to my dear colleagus and friends at the department of Mechanical Engineering, Lecco for all their continuous support during all the time I spend in Lecco. Special thanks to my family, more importantly to my father for allways encouraging me and support me during my stay in italy.

NOMENCLATURE

Symbol	Description	Unit
Re	Reynolds Number	-
υ	Kinematic Viscosity of Fluid	m^2/s
ρ	Fluid Density	Kg/m^3
D	Diameter / Characteristic Length	M
μ	Fluid Viscosity	$N \cdot s/m^2$
We	Weber Number	-
σ	Surface Tension	N/m
Z	Ohnesorge Number	-
U_{inj}	Injection Velocity	m/s
m_{inj}	Fuel mass flow rate in cylinder	Kg/m^3
ΔP_{inj}	Pressure Difference between Sac hole and Combustion Chamber	Pa
$\zeta 1, \zeta 2$	Random Numbers	-
Φ	Spray Cone Angle	Rad
Ψ	Polar Angle in Spray-Cone System	Rad
C_d	Discharge co-efficient	-
Ω	Growth Rate of Most Unstable Wave	s^{-1}
Λ	Wavelength of Fastest Growing Wave	M
T	Taylor Number	-
τ_{bu}	Value of Characterisitics of Time Span	s
B_1, C_1, C_2, C_3	Model Constant	-
C_v	Velocity Co-Efficient	-
ρ_f	Fuel Density	Kg/m^3
ω	Growth Rate	s^{-1}
θ	Spary Cone Angle	rad

TABLE OF CONTENTS

LIST OF FIGURES

LIST OF TABLES

CHAPTER 1

1. Introduction:

Computational Fluid Dynamics (CFD) has an established role in the automobile industry. After being a supplementary tool besides experiments, today it is a widely used as an exclusive instrument for solving flow related problems inside and around an automobile. Diesel engines and also injection systems of diesel engines reached a level of development, where further improvement desires great effort and a high level of technical competence. The use of specialized CFD codes already in the basic research phase of development proliferated. The technical capabilities of these systems today enable not only the partial substitution of experiments, but give also an insight into phenomena characterized by orders of magnitudes in time and space that are currently not accessible even by enhanced measurement technique.

In the case of high-pressure diesel injection for example, the spray break-up near the nozzle is mainly influenced by the flow conditions inside the injection holes. However, because of the small hole diameters (less than 200 μm for passenger cars) and the high flow velocities (about 600 m/s and more), the three-dimensional turbulent and cavitating two-phase flow is not accessible by measurement techniques. One very costly and time-consuming possibility of getting some insight into these processes is to manufacture a glass nozzle in real-size geometry and to use laser-optical measurement techniques. Outside the nozzle in the very dense spray measurements of the three-dimensional spray structure (droplet sizes, velocities etc.) become even more complicated, because the dense spray does not allow any sufficient optical access of the inner spray core. In these and other similar cases numerical simulations can give valuable information and can help to improve and optimize the processes of interest. Finally, the enormous research work which is necessary to develop and continuously improve the numerical models must be mentioned. This research work continuously increases our knowledge about the relevant processes, reveals new and unknown mechanisms, and is also a source of new, unconventional ideas and improvements.

There are three classes of models that can be used in numerical simulations of in-cylinder processes. If very short calculation times are necessary, so-called thermodynamic models are used. These zero-dimensional models, which do not include any spatial resolution, only describe the most relevant processes without providing insight into local sub-processes. Very simple sub-models are used, and a prediction of pollutant formation is not possible. The second class of models are the

phenomenological models, which consider some kind of quasi- spatial resolution of the combustion chamber and which use more detailed sub-models for the description of the relevant processes like mixture formation, ignition and combustion. These phenomenological models may be used to predict integral quantities like heat release rate and formation of nitric oxides (NOx).

The third class of models are the computational fluid dynamics (CFD) models. In CFD codes, the most detailed sub-models are used, and every sub-process of interest is considered. For example, in case of mixture formation, the sub- processes injection, break-up and evaporation of single liquid droplets, collisions of droplets, impingement of droplets on the wall etc. are modeled and calculated for every individual droplet, dependent on its position inside the three-dimensional combustion chamber. Thus, this class of models is the most expensive regarding the consumption of computational power and time. The turbulent three-dimensional flow field is solved using the conservation equations for mass, momentum and energy in combination with an appropriate turbulence model. The CFD codes are especially suited for the investigation of three-dimensional effects on the in-cylinder processes, like the effect of tumble and swirl, the influence of combustion chamber geometry, position of injection nozzle, spray angle, number of injection holes, etc. Although all of the three model categories mentioned above are needed and are being used today, the anticipated further increase of computer power will especially support the use of the more detailed CFD models in the future. As far as modeling of in-cylinder processes is concerned, most of the research work today concentrates on the development of CFD sub-models.

Liquid spray formation concern a lot of physics, starting from breakup of the liquid core into droplets short after the nozzle exit, called primary breakup. In a second stage the formed droplets breakup into smaller droplets, called secondary breakup. In automotive applications, with high ambient pressures and temperatures, the fuel droplets evaporate during their path until the liquid length is reached. From then on the evaporated fuel penetrates further into the surrounding gas, and at some point the spray auto-ignites.

Summarizing the situation today, it must be pointed out that the predictive quality of the models currently used in CFD codes has already reached a very high level, and that the use of CFD simulations for the research and development activities of engine manufacturers with respect to the design of new and enhanced spray breakup concepts is not only practical but already necessary. Today, the complex task of developing advanced spray breakup concepts can only be achieved with a combination of experimental and numerical studies.

The aim of this study is, in the first, place to accurately and efficiently model non-reacting diesel spray formation. A CFD package (OpenFOAM [48]) with a developing spray model. Validation of these spray simulations is done with constant volume, high pressure cell measurements from most renounced engine research group (ECN-Sandia[49]).

CHAPTER 2

2. Fundamentals of Liquid Spray

2.1 Breakup of Fluids

The conversion of bulk liquid into a dispersion of small droplets ranging in size from sub-micron to several hundred microns (micrometers) in diameter is of importance in many industrial processes such as spray combustion, spray drying, evaporation cooling, spray coating, and drop spraying; and has many other applications in medicine, meteorology, and printing. Breakup of fluids can be described as the procedure when bulk liquid disintegrates into droplets by the action of forces both internal and external. In the same way, when an existing droplet break down in at least two smaller droplets or release a number of significantly smaller droplets is also recounted as breakup of fluids. Following discussion will emphasize on the two basic parts of breakup processes: the primary breakup and the secondary one.

2.1.1 Primary Breakup

When a liquid emerges from a plain-orifice atomizer, such as a diesel injector nozzle, and the injection velocity and the level of cavitation does not exceed a certain level, it has a continuum body of cylindrical form. The various internal and external forces competing on the surface of this liquid column create oscillations and perturbations of the surface [Lefebvre, 1989 (1)]. If these oscillations and perturbations are amplified to a critical extent, the liquid body disintegrates into droplets. This process is referred to as primary breakup, and is very important because with initiating the atomization process and determining the extent of the liquid core, it provides the initial conditions for the dispersed flow region.

Depending on the physical conditions, this process can be diverse in nature, exhibiting substantially different characteristics. The categorization of these breakup types can be based on various considerations, however, a fundamental platform is provided by the three most important physical parameters related to spray breakup. [Kadocsa A., 2007(17)].

1. The *Reynolds number* represents ratio of inertial forces to viscous forces and is defined in the spray literature as displayed in Eq. (1) [Lefebvre, 1989 (1); Reitz, 1987 (2)]:

$Re = (u\rho D)/\mu$ (2.1)

2. The *Weber number* represents the ratio of aerodynamic force to the force of surface tension, and can be defined in two ways, depending on the physical mechanisms that are aimed to be described [Sirignano, 1999 (3); Reitz, 1987 (2)]:

$We = (u^2\rho D)/\sigma$ (2.2)

$We = (u^2\rho D)/\sigma$ (2.3)

3. The third significant number is *Ohnesorge number (Z),* often known as viscosity number or Laplace number. *Z* relates the viscous forces to inertial and surface tension forces and is defined as [Pilch & Erdman, 1987(4)]:

$$Z = \frac{\sqrt{We_l}}{Re} = \frac{\mu_l}{\sqrt{\sigma \rho_l D}} \quad (2.4)$$

Large value of 'Z' indicates a great influence of the viscosity. This number is often used to relate to free surface fluid dynamics such as dispersion of liquids in gases and in spray technology. [Lefebvre, Arthur Henry,1989; Ohnesorge, W 1936 (5)]

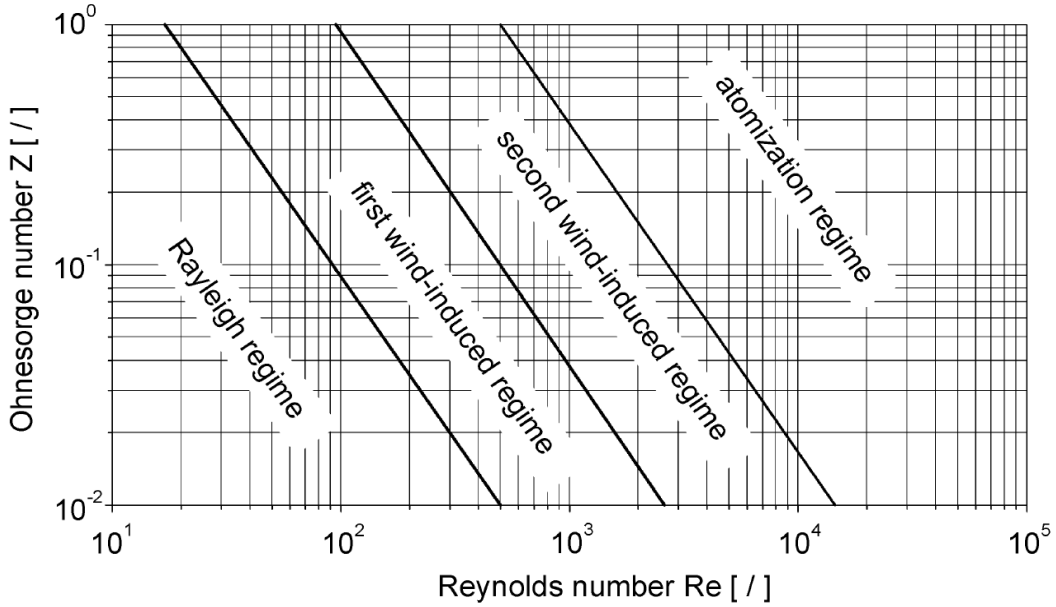

Figure 2.1 : Ohnesorge Diagram : Jet break-up regimes [Baumgarten, 2006(8)].

The most commonly referred categorization of the expected types of primary breakup based

on these numbers was created by Ohnesorge [Ohnesorge in 1936 (6)] and was improved by introduction of a distinction between first and second wind induced breakup by Reitz [Reitz, 1978 (7)].

The physical effects and mechanisms discussed below are all present in each type of primary breakup in a certain extent. It is their dominance that's changing as a result of changes in physical circumstances.

Zone A – Rayleigh breakup

At low jet velocities only the surface tension has a significant impact on the breakup characteristics: it promotes contractions, but on the other hand it impedes flare of the liquid column when the displacement of liquid from the contracted region into neighboring sections occurs. Hence, the smallest perturbations lead to axial-symmetric oscillations, which lead as an end effect to breakup of the liquid column. The resulted droplets are larger than the diameter of the original jet. (Kadocsa A.,2007[17]).

Zone B – First Wind-Induced Breakup

With increase in Weber number (increase of relative jet velocity if other circumstances remain constant), the aerodynamic forces on the surface of the liquid column gain on influence. The pressure distribution resulted from the flow around the surface perturbations contribute to the breakup process. According to observations, the resulted droplets are approximately the same in diameter as the original jet [Lefebvre, 1989(5)].

Zone C – Second Wind-Induced Breakup

With further increase of Weber number, the processes of the first wind-induced breakup still occur, but in a larger extent, and more rapidly, providing droplets somewhat smaller than the diameter of the original jet. Besides that, in a process referred to as surface stripping short surface waves (Kelvin- Helmholtz instabilities) distract also small droplets from jet surface. [Kadocsa A. 2007 (17)].

Zone D – Atomization

Above a certain level of Weber number, the liquid jet immediately starts to get distracted along the entire jet cross section at the exit of the nozzle hole. It means that the unbroken liquid jet section, i.e. the symmetric, undisturbed liquid column characteristic to the former three breakup regimes in a decreasing extent with increase of Weber number, is either absent in this case, or under

circumstances exists in a very short length, not detectable with recent measurement technique. It is unclear in what extent aerodynamic forces and forces stemming from nozzle flow turbulence and cavitation affect the early stage of this type of breakup. [Kadocsa A., 2007 (17)].

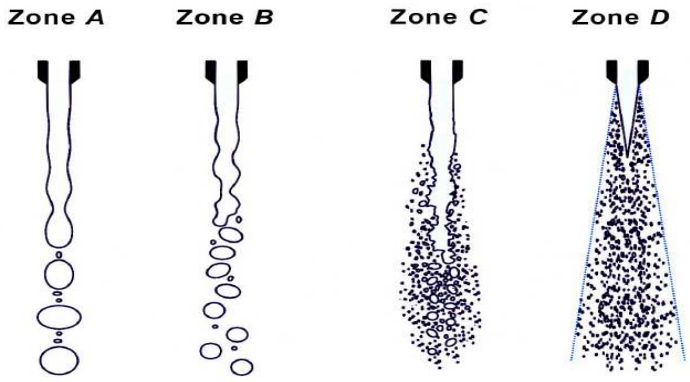

Figure 2.2 : Typical image of the four primary break-up regimes. [Schneider, 2003(16)).

For stationary conditions, the boundaries between the four different jet break-up regimes can be drawn in. However, it has turned out that including only the liquid phase properties in the description of the regimes is not sufficient, because atomization can be enhanced by increasing the gas density [e.g. Torda,1973 (9); Hiroyasu and Arai, 1990 (10)]. Thus, Reitz [Reitz, 1978 (7)] suggested to include the gas-to-liquid density ratio and to extend the two-dimensional Ohnesorge diagram into a three-dimensional one as shown in Fig. 2.2.

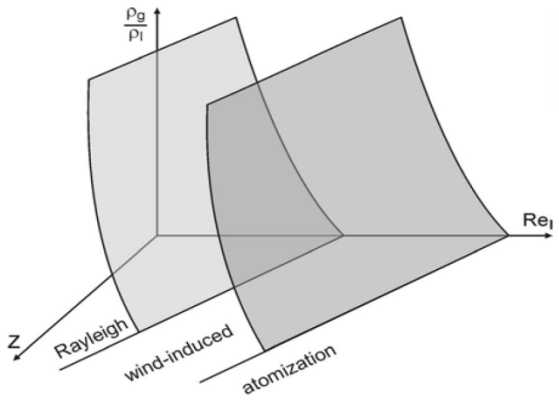

Figure 2.3 : Schematic diagram including the effect of gas density on jet break-up. [Baumgarten, 2006 (8)].

A schematic description of the different jet break-up regimes is given in Fig.2.3. If the nozzle geometry is fixed and the liquid properties are not varied, the only variable is the liquid velocity u . Figure 2.4 shows the corresponding break-up curve, which describes the length of the unbroken jet as a function of jet velocity u.[Baumgarten, 2006 (8)].

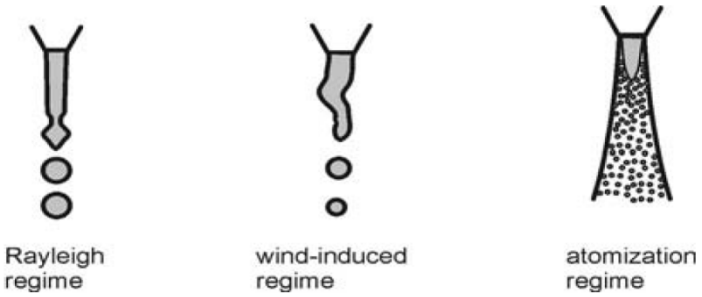

Figure 2.4 : Schematic description of jet break-up regimes.[Baumgarten, 2006(8)].

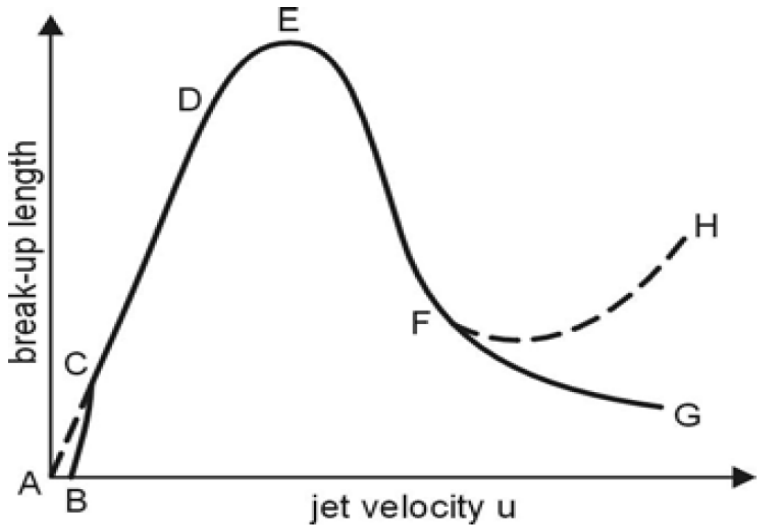

Figure 2.5 : Jet surface breakup length as function of jet velocity u. ABC: Drop flow, CD:Rayleigh break-up, EF: first wind-induced break-up, FG (FH): second wind-induced breakup, beyond G (H): atomization regime.[Baumgarten, 2006(8)].

At very low velocities, drip flow occurs and no jet is formed. An increase of u results in the formation of an unbroken jet length, which increases with increasing velocity. This regime is called Rayleigh break-up. Break-up occurs due to the growth of axis-symmetric oscillations of the complete jet volume, initiated by liquid inertia and surface tension forces. The droplets are pinched off the jet, and their size is greater than the nozzle hole diameter D. This flow has already been described theoretically by Rayleigh, 1878 [11]. Further advanced analyses have been published by Yuen, 1968 [12], Nayfey, 1968 [13], and Rutland and Jameson, 1970 [14] for example.

A further increase in jet velocity results in a decrease of the break-up length, but it is still a multiple of the nozzle diameter. The average droplet size decreases and is now in the range of the nozzle diameter. In this first wind-induced regime, the relevant forces of the Rayleigh regime are amplified by aerodynamic forces. The relevant parameter is the gas phase Weber number Weg =

$u^2_{rel}D\rho_g/\sigma$, which describes the influence of the surrounding gas phase. A detailed theoretical analysis is given in Reitz and Bracco, 1986 [15].

In the second wind-induced break-up regime, the flow inside the nozzle becomes turbulent. Jet break-up now occurs due to the instable growth of short wavelength surface waves that are initiated by jet turbulence and amplified by aerodynamic forces due to the relative velocity between gas and jet. The diameter of the resulting droplets is smaller than the nozzle diameter, and the break-up length decreases with an increasing Reynolds number, line FG in Fig. 2.4. A detailed theoretical analysis is again given in Reitz and Bracco,1986 [15]. The jet now no longer breaks up as a whole. Due to the separation of small droplets from the jet surface, the disintegration process begins at the surface and gradually erodes the jet until it is completely broken up. Now two break-up lengths, the length describing the beginning of surface break-up (intact surface length) and the length describing the end of jet break-up (core length) should be accounted for. While the intact surface length decreases with increasing jet velocity, the core length may increase. However, it must be pointed out that measurements of both lengths become extremely difficult at increased Reynolds numbers, and, for this reason, experimental results from different authors may differ in this regime.

The atomization regime is reached if the intact surface length approaches zero. A conical spray develops, and the spray divergence begins immediately after the jet leaves the nozzle, i.e. the vertex of the spray cone is located inside the nozzle. An intact core or at least a dense core consisting of large liquid fragments may still be present several nozzle diameters downstream the nozzle. This is the relevant regime for engine sprays. The resulting droplets are much smaller than the nozzle diameter. The theoretical description of jet break-up in the atomization regime is much more complex than in any other regime, because the disintegration process strongly depends on the flow conditions inside the nozzle hole, which are usually unknown and of a chaotic nature. The validation of models is also difficult, because experiments are extremely complicated due to the high velocities, the small dimensions, and the very dense spray. [Baumgarten, 2006 (8)].

2.1.2 Secondary Break-Up

The process described so far is generally referred to as primary breakup, detaches droplets and ligaments from the liquid core of the spray. These fluid parts are however, usually not stable and hence are subject to further breakup. This subsequent breakup process is generally referred to as secondary breakup.

The importance of secondary breakup is pronounced in case of typical power and propulsion systems, where due to the conditions prevailing (usually high temperature of ambient gas), the surface tension of droplets becomes very small, and hence the potential for significant effects of droplet deformation and secondary breakup becomes high [Faeth et al, 1995 (18)].

The secondary breakup of fluids occurs mainly through aerodynamic forces. Therefore, the relative velocity of the droplet and the surrounding ambient gas plays an important role in the breakup mechanism.

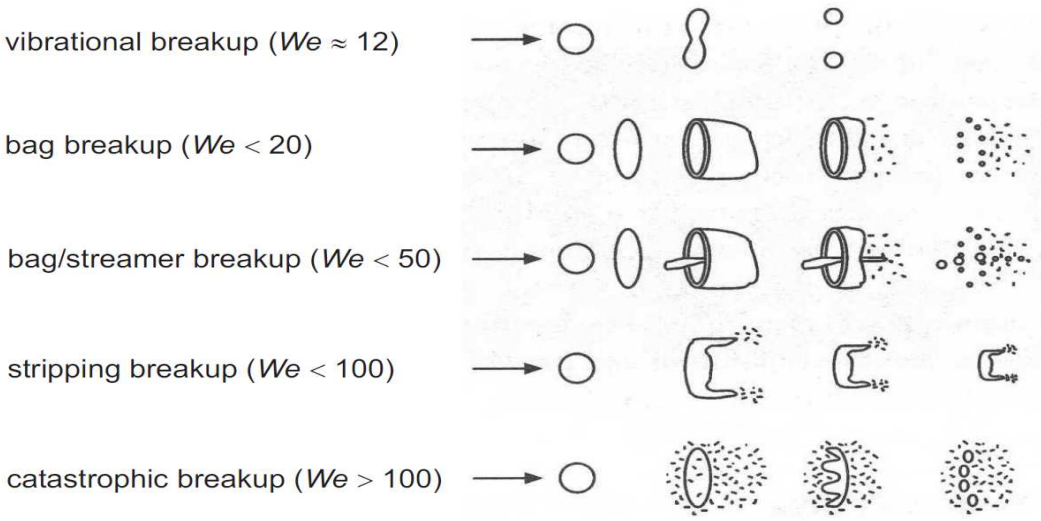

Figure 2.6 : Drop breakup regimes according to Wierzba [Wierzba,1993 (22)].

With increase of the relative velocity (or the increase of the Weber number due to other factors), the forms of secondary breakup are denoted as given in Fig. 2.6.

It must be pointed out that the transition Weber numbers that are published in the literature are not consistent. This holds especially true for break-up mechanisms at high Weber numbers, where some authors also distinguish between additional sub-regimes. While the transition Weber numbers of Wierzba,1993 [22] are in the same range as the ones of Krzeczkowski,1980 [23], Arcoumanis et-al., 1997 [24] distinguish between two different kinds of stripping breakup, Table 2.1, that cover the Weber number range from 100 to 1000, and the chaotic break-up is beyond We_g = 1000.

The vibrational mode occurs at very low Weber numbers near the critical value of $We_g \approx 12$, below which droplet deformation does not result in break-up. Bag break-up results in a disintegration of the drop due to a bag-like deformation. The rim disintegrates into larger droplets,

while the rest of the bag breaks up into smaller droplets, resulting in a bimodal size distribution. An additional jet appears in the bag-streamer regime. In the stripping regime, the drop diameter gradually reduces because very small droplets are continuously shed from the boundary layer due to shear forces. This break-up mode also results in a bimodal droplet size distribution. Catastrophic break-up shows two stages: Because of a strong deceleration, droplet oscillations with large amplitude and wavelength lead to a disintegration in a few large product droplets, while at the same time surface waves with short wavelengths are stripped off and form small product droplets.

Table 2.1 : Transition Weber numbers of different drop break-up regimes.

Wierzba,1993 [22]		Weber number	Arcoumanis et al.,1997 [24]		Weber number
1	Vibrational	≈ 12	1	Vibrational	≈ 12
2	Bag	< 20	2	Bag	< 18
3	Bag-jet (Bag-streamer)	< 50	3	Bag-jet (Bag-streamer)	< 45
			4	Chaotic break-up	< 100
4	Catastrophic	< 100	5	Sheet stripping	< 350
			6	Wave crest stripping	< 1000
5	Catastrophic	> 100	7	Catastrophic	> 1000

In engine sprays, all of these break-up mechanisms occur. However, most of the disintegration processes take place near the nozzle at high Weber numbers, while further downstream the Weber numbers are significantly smaller because of reduced droplet diameters due to evaporation and previous break up, and because of a reduction of the relative velocity due to drag forces. [Baumgarten, 2006 (8)].

2.1.3 Atomization in Diesel Spray

Atomization and spray process is a typical gas-liquid two-phase flow of great practical relevance in applications such as the fuel injection in gas-turbine combustors of aircraft engines and in internal combustion engines. The combustion performance and emissions are mainly influenced by the atomization of the liquid fuel, the motion and evaporation of the fuel droplets and mixing of fuel with air. The dynamics of spray and its combustion characteristics are extremely important in determining, for instance, the flame stability behavior at widely varying loads, the safe and efficient

utilization of energy, as well as the mechanisms of pollutants formation and destruction. Understanding and controlling atomization and spray combustion is becoming an essential part of the industrial applications, which have been driven by increasingly urgent demands to improve fuel and energy efficiencies, and to drastically reduce the emission of pollutants. The spray combustion process may be divided into several elements, such as atomization, liquid transport, vaporization, and combustion. In general, liquid fuel is injected through a nozzle system into the combustion chamber and is atomized to form a spray of droplets before gas-phase combustion takes place in the vaporized fuel. Fig.2.7 shows a schematic of a simple liquid spray plume structure.

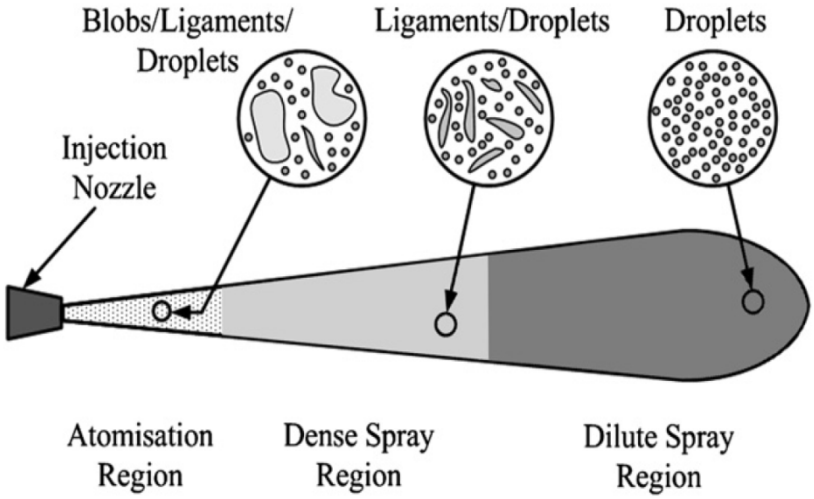

Figure 2.7: A Schematic of liquid spray. [X. Jiang, G.A. Siamas, K. Jagus, T.G. Karayiannis, 2009 (25)]).

In the atomization region, the liquid dominates the flow and the liquid fuel disintegrates into ligaments and droplets. Large liquid blobs which are bulks of continuous liquids present in the atomization region. The dense spray region has lower but still significant liquid volume fraction and includes secondary breakup of drops and ligaments as well as dropdrop interactions, such as collisions and coalescence. Liquid ligaments normally present in the atomization and dense spray regions, which are non-spherical liquid sheets, sheared off the liquid jet column. In the dilute spray region, spherical droplets are well formed and have a strong interaction with the turbulent airflow. In general, the spray structure depends on the injection pressure difference, injector size, fuel viscosity and fuel density. With the initial injection velocity, liquid-fuel droplets penetrate into the ambient gaseous environment which is usually air or more often mixture of air and hot combustion gas. The fuel spray advances with time until droplets are vaporized by the hot combustion gas. [X. Jiang, G.A. Siamas, K. Jagus, T.G. Karayiannis, 2009 (25)].

There are different technical methods of achieving atomization. Carburetors, airbrushes, and

spray bottles are only a few examples of atomizers used ubiquitously. Essentially, all that is needed is a force such as a high pressure or a large shear force from the high relative velocity between the liquid to be atomized and the surrounding air or gas to overcome the surface tension of the liquid. Most practical atomizers are of the pressure, rotary or twin-fluid type. In a pressure type of atomizer used frequently in fuel injection in combustion engines, the pressure force overcomes the liquid surface tension. In a rotary or twin-fluid type atomizer (all nozzle types in which atomization is achieved using high-velocity air, gas or steam), the shear force or the centrifugal force overcomes the liquid surface tension. Many other forms of atomizers have also been developed that are useful in special applications, including electrostatic atomizer where electrical force is used to overcome surface tension forces and achieve atomization, impinging jet atomizer where liquid jets collide outside the nozzle to achieve atomization, ultrasonic atomizer in which high frequency (2050 kHz) vibration is utilized to produce narrow drop size distribution and low velocity spray from a liquid, whistle atomizer in which sound waves are used to shatter a liquid jet into droplets, and windmill atomizer which is a rotary atomizer used for aerial application of pesticides with a unique feature of using wind forces to provide rotary motion. Most commonly used atomizers for spray combustion applications include mainly plain-orifice atomizers for fuel injection in combustion engines and gas-turbine combustors, pressure-swirl and air-blast atomizers and effervescent flow atomizers for combustors, engines and propulsion applications. The plain orifice
is the most common type of atomizer and the most simply made. However, there is nothing simple about the physics of the internal nozzle flow and the external atomization. In the plain-orifice atomizer, the liquid is accelerated through a nozzle due to high injection pressure, forms a liquid jet, and then forms droplets. This apparently simple process is impressively complex in physics. The plain orifice may operate in single-phase or cavitating flow regime. The transition between regimes is abrupt, producing dramatically different sprays. The internal regime determines the velocity at the orifice exit, as well as the initial droplet size and the angle of droplet dispersion. Combustion applications for plain-orifice atomizers include diesel engines, turbojet afterburners, ramjets, and rocket engines.

Another important type of atomizer is the pressure-swirl atomizer, sometimes referred to by the gas-turbine community as a simplex atomizer. This type of atomizer accelerates the liquid through nozzles known as swirl ports into a central swirl chamber. The swirling liquid pushes against the walls of the swirl chamber and develops a hollow air core. It then emerges from the orifice as a thinning sheet, which is unstable, breaking up into ligaments and droplets. The pressure-swirl atomizer is very widely used for liquid-fuel combustion in gas turbines, oil furnaces, and direct injection spark-ignited automobile engines as well. In order to accelerate the breakup of

liquid sheets from an atomizer, an additional air stream is often directed through the atomizer. The liquid is formed into a sheet by a nozzle, and the air is then directed against the sheet to promote atomization. This technique is called air-assisted atomization or air-blast atomization, depending on the quantity of air and its velocity. The addition of the external air stream past the sheet produces smaller droplets than without the air. The exact mechanism for this enhanced performance is not completely understood. It is thought that the assisting air may enhance the sheet instability.

The air may also help disperse the droplets, preventing collisions between them. Air-assisted atomization is used in many of the same fields as pressure-swirl atomization, where fine atomization is especially required. The merits of the air-blast atomizer have led to its installation in a wide variety of aircraft, marine, and industrial gas turbines. Similar to the pressure swirl atomizer, there is also a type of atomizer referred to as the flat-fan atomizer which makes a flat sheet and does not use swirl. In addition to the commonly used atomizers, effervescent atomization is the injection of liquid infused with a super-heated (with respect to downstream conditions) liquid or propellant. As the volatile liquid exits the nozzle, it rapidly changes phase. This phase change quickly breaks up the stream into small droplets with a wide dispersion angle. It also applies to cases where a very hot liquid is discharged. Effervescent atomization involves bubbling a small amount of gas into the liquid and the physics of effervescence atomization has not been fully understood. [X. Jiang, G.A. Siamas, K. Jagus, T.G. Karayiannis, 2009 (25)].

2.2 Structure of Engine Spray

2.2.1 Full-Cone Spray

A schematic description of a full-cone high-pressure spray is given in Fig. 2.8 The graphic shows the lower part of an injection nozzle with needle, sac hole, and injection hole. Modern injectors for passenger cars have hole diameters of about 180 μm and less, while the length of the injection holes is about 1 mm.

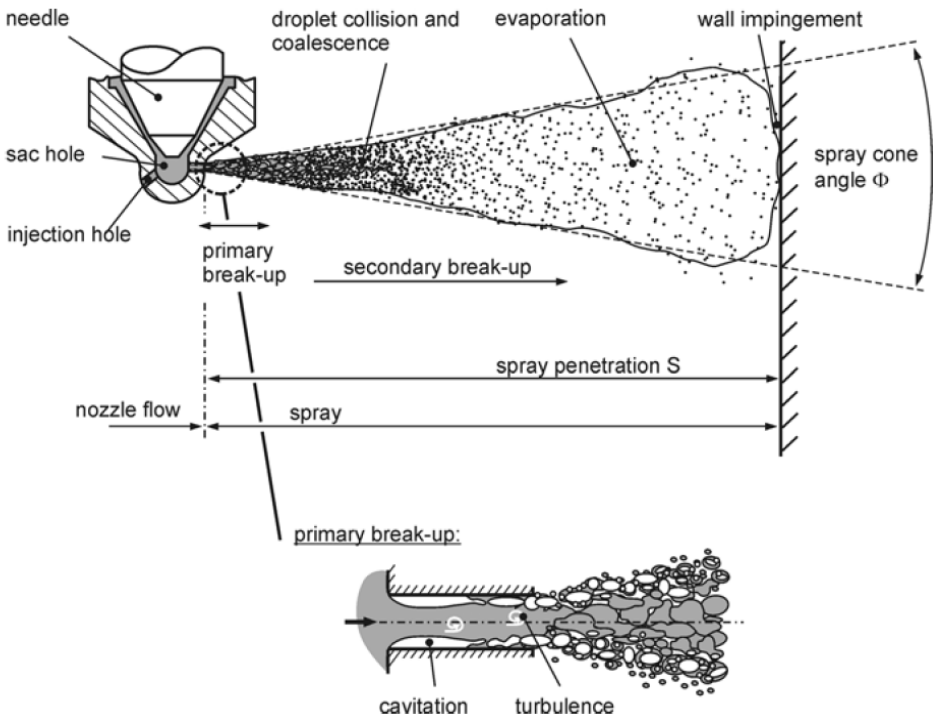

Figure 2.8: Break-up of a full-cone diesel spray . [Baumgarten, 2006 (8)].

Today, injection pressures of up to 200 MPa are used. The liquid enters the combustion chamber with velocities of 500 m/s and more, and the jet breaks up according to the mechanisms of the atomization regime. Immediately after leaving the nozzle hole, the jet starts to break up into a conical spray. This first break-up of the liquid is called primary break-up and results in large ligaments and droplets that form the dense spray near the nozzle. In case of high-pressure injection, cavitation and turbulence, which are generated inside the injection holes, are the main break-up mechanisms. The subsequent break-up processes of already existing droplets into smaller ones are called secondary break-up and are due to aerodynamic forces caused by the relative velocity between droplets and surrounding gas.

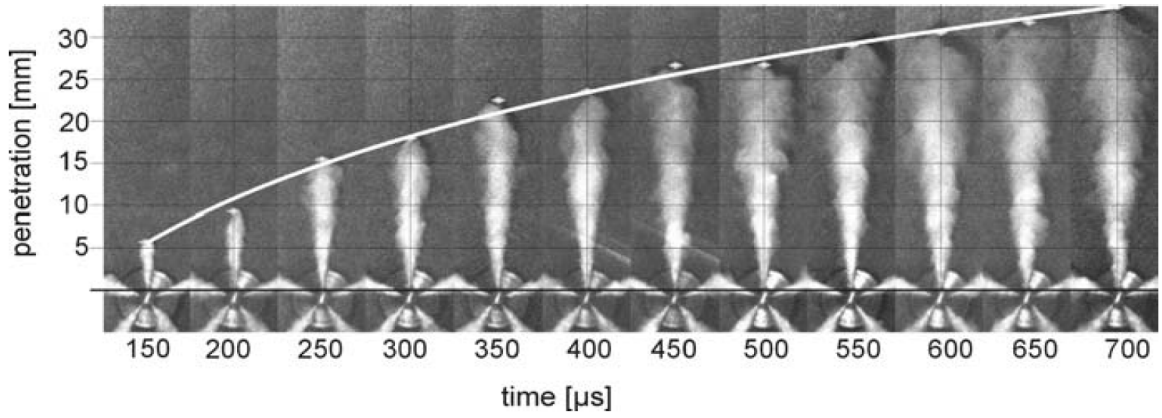

Figure 2.9 : Spray development during injection (Stegemann J, Seebode J, Baltes J, Baumgarten C, Merker GP, 2002 [26]), P_{rail} = 70 MPa, P_{back} = 5 Mpa, T_{air} = 890 K . . [Baumgarten, 2006 (8)].

In the following, the mechanisms of primary break-up of high-pressure fullcone sprays shall be described through figure. Primary break-up is the first disintegration of the coherent liquid into ligaments and large drops. Figure 2.10 summarizes possible break-up mechanisms.

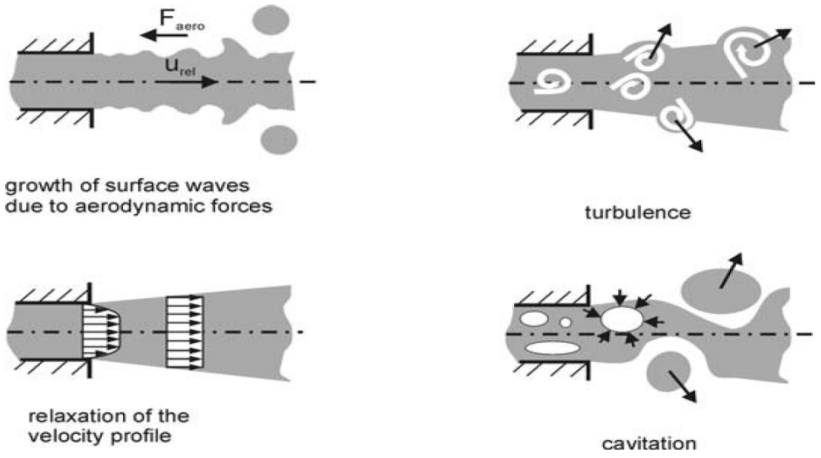

Figure 2.10: Mechanism of primary breakup for a full-cone diesel spray. . [Baumgarten, 2006 (8)].

2.2.2 Hollow-Cone Spray

In order to achieve maximum dispersion of the liquid at moderate injection pressures and low ambient pressures, hollow-cone sprays are usually used. Hollow-cone sprays are typically characterized by small droplet diameters, effective fuel-air mixing, reduced penetration, and consequently high atomization efficiencies. These sprays are used in conventional gasoline engines, where the fuel is injected into the manifold, and in direct injection spark ignited (DISI) engines.

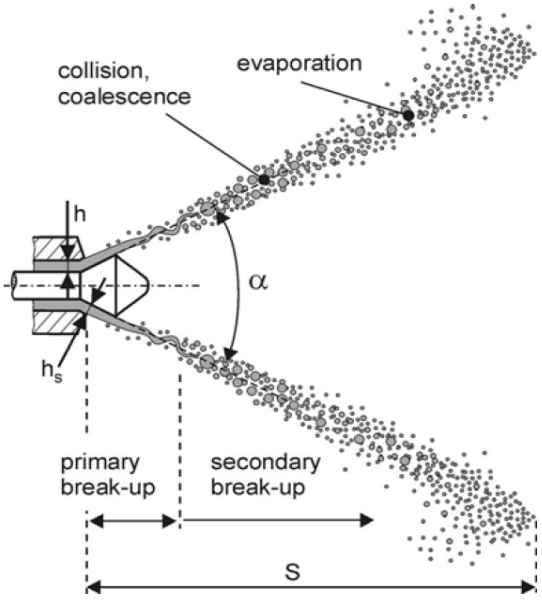

Figure 2.11: Hollow-cone diesel spray. Example: outward opening nozzle . [Baumgarten, 2006 (8)].

Figures 2.12 and 2.13 show the temporal development of a typical spray produced by a pressure-swirl atomizer. Fig. 2.14 represents a schematic illustration of the fully developed spray.

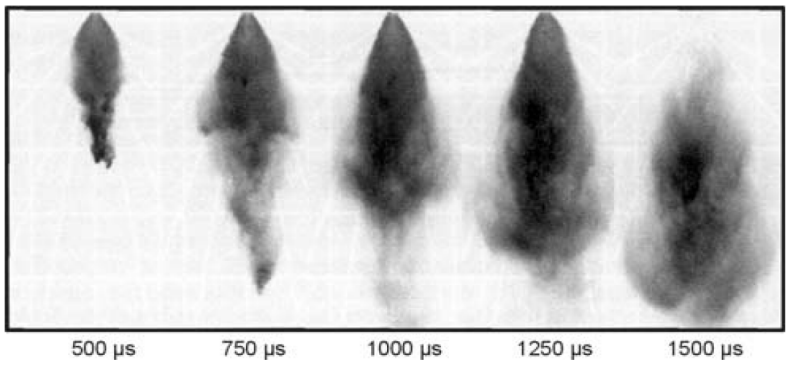

Figure 2.12: Temporal development of a spray from a pressure-swirl atomizer (Homburg A, 2002[27]), P_{rail} = 10 MPa, $P_{chamber}$ = 0.24 MPa, $T_{chamber}$ = 393 K. [Baumgarten, 2006 (8)].

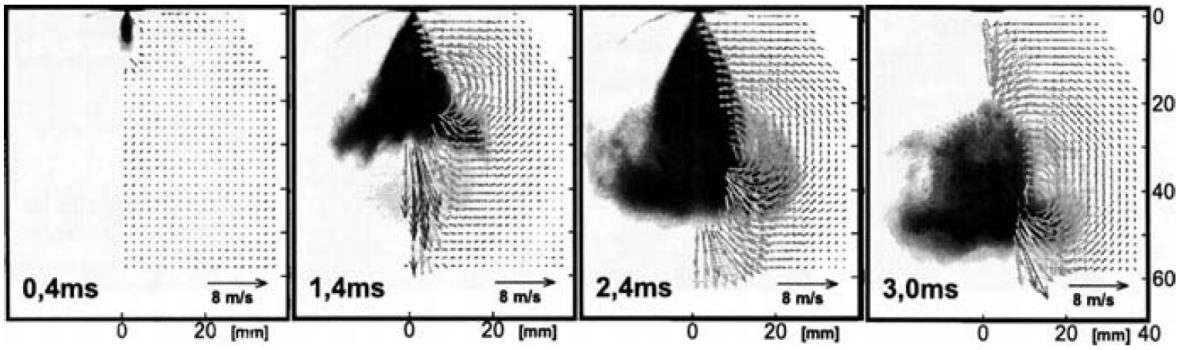

Figure 2.13: Temporal development of the secondary gas flow around a spray from a pressure-swirl atomizer. (Gindele J, 2001 [28]), P_{rail} = 7 MPa, $P_{chamber}$ = 0.102 MPa, $T_{chamber}$ = 298 K (Baumgarten, 2006[8]).

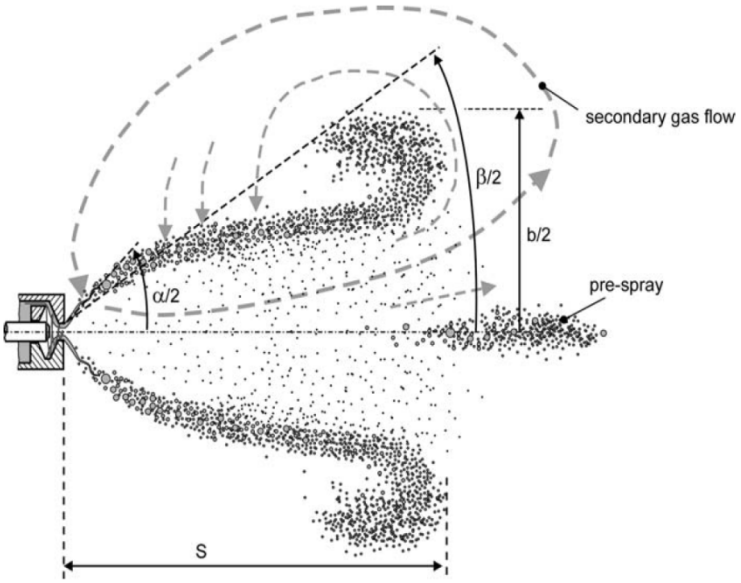

Figure 2.14: Typical spray from a pressure-swirl atomizer (schematic illustration) [Baumgarten, 2006 (8)].

CHAPTER 3

3. Modeling of Spray and Mixture Formation

The atomization of IC-engine fuel sprays can be divided into two main processes, primary and secondary break-up. As discussed in the previous chapter, the former takes place in the region close to the nozzle at high Weber numbers. It is not only determined by the interaction between the liquid and gaseous phases but also by internal nozzle phenomena like turbulence and cavitation. Atomization that occurs further downstream in the spray due to aerodynamic interaction processes and which is largely independent of the nozzle type is called secondary break-up. The classic break-up models like TAB (Taylor Analogy Break-up), RD (Reitz and Diwakar) and WAVE do not distinguish between the two processes [v. Künsberg et al, 1998 (37)]. The parameters of these models are usually tuned to match experimental data further downstream in the region of the secondary break-up. Originally, these parameters are supposed to depend only on nozzle geometry, in reality they also account for numerical effects. Other models like ETAB (Enhanced TAB), FIPA (Fractionnement Induit Par Acceleration) or KH-RT (Kelvin Helmholtz - Rayleigh Taylor) treat the primary break-up region separately [v. Künsberg et al, 1998 (37)]. Hence, they in principle offer the possibility to simulate both break-up processes independently. The correct values for the additional set of parameters, however, are not easy to determine due to the lack of experimental data for the primary break-up region.

Despite the sometimes tedious tuning of these model parameters the use of break-up models is generally advantageous compared to the initialisation of measured droplet distributions at the nozzle orifice. In the first approach the droplets are simply initialised with a diameter equal to the nozzle orifice (blob injection), the droplet spectrum automatically evolves from the subsequent break-up processes. The latter approach gives satisfying results only as long as injection pressure and droplet Weber numbers are low. [Reinhard et al.,2002 (36)]. Different modeling mainly which are used in this thesis and CFD coding are illustrated below.

3.1 Primary Break-Up

The primary break-up process provides the starting conditions for the calculation of the subsequent mixture formation inside the cylinder, and for this reason a detailed modeling of the

transition from the nozzle flow into the dense spray is essential. Because the Lagrangian description of the liquid phase requires the existence of drops, the simulation of spray formation always begins with drops starting to penetrate into the combustion chamber. The task of a primary break-up model is to determine the starting conditions of these drops, such as initial radius and velocity components (spray angle), which are mainly influenced by the flow conditions inside the nozzle holes.

There are only very few detailed models for the simulation of primary break-up of high-pressure sprays. One reason is that the experimental investigation is extremely complicated because of the dense spray and the small dimensions. Thus, it is difficult to understand the relevant processes and to verify primary break-up models. On the other hand, it is now possible to simulate the flow inside high pressure injectors, but because of different mathematical descriptions of the liquid phase inside (Eulerian description) and outside the nozzle (Lagrangian description), it is not possible to calculate the primary break-up directly, and models must be used.

Different classes of break-up models exist concerning the way the relevant mechanisms like aerodynamic-induced, cavitation-induced and turbulence-induced break-up are treated. The simpler the model, the less input data is required, but the less the nozzle flow is linked with the primary spray and the more assumptions about the upstream conditions have to be made. This results in a significant loss of quality concerning the prediction of structure and starting conditions of the first spray near the nozzle. On the other hand, an advantage of the simpler models is that their area of application is wider because of the more global modeling. Furthermore, detailed models often require a complete CFD simulation of the injector flow as input data. This results in an enormous increase of computational time, but the close linking of injector flow and spray guarantees the most accurate simulation of the primary break-up process and its effect on spray and mixture formation in the cylinder that is possible today. It must be pointed out that all kind of models have their special field of application. Depending on the available input data, the computational time, the relevant break-up processes of the specific configuration as well as the required accuracy of the simulation, the appropriate model has to be chosen. [Baumgarten, 2006 (8)].

3.1.1 Blob Method

The simplest and most popular way of defining the starting conditions of the first droplets at the nozzle hole exit of full-cone diesel sprays is the so-called blob method. This approach was developed by Reitz and Diwakar, 1987 [2, 29]. The blob method is based on the assumption that

atomization and drop break-up within the dense spray near the nozzle are indistinguishable processes, and that a detailed simulation can be replaced by the injection of big spherical droplets with uniform size, which are then subject to secondary aerodynamic induced break-up, see Fig. 3.1. The diameter of these blobs equals the nozzle hole diameter D (mono-disperse injection) and the number of drops injected per unit time is determined from the mass flow rate. Although the blobs break up due to their interaction with the gas, there is a region of large discrete liquid particles near the nozzle, which is conceptually equivalent to a dense core. Assuming slug flow inside the nozzle hole, the conservation of mass gives the injection velocity U_{inj} (t) of the blobs

$$U_{inj}(t) = m_{inj}(t) / A_{hole}\,\rho_l \qquad (3.1)$$

Where $A_{hole} = (\pi D^2/4)$ is the cross-sectional area of the nozzle hole, ρ_l is the liquid density, and m_{inj} (t) is the fuel mass flow rate (measurement).

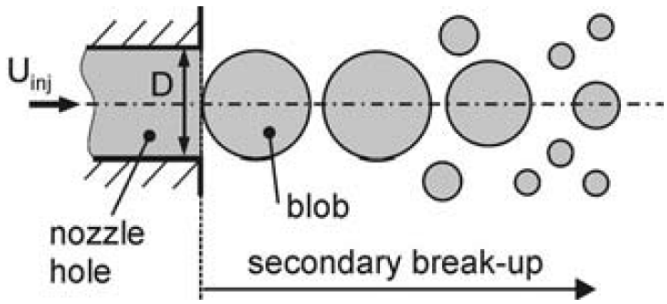

Figure 3.1: Blob method . [Baumgarten, 2006 (8)].

If there are no measurements about the injected mass flow, the Bernoulli equation for frictionless flow can be used in order to calculate an upper limit of the initial velocity,

$$U_{inj,max} = \sqrt{\frac{2\Delta p_{inj}}{\rho_l}} \qquad (3.2)$$

Where Δp_{inj} is the difference between the sac hole and combustion chamber pressures. Because the flow is not frictionless, $U_{inj,max}$ is reduced by energy losses.

According to measurements of Schugger et al., 2000 [30], Walther et al., 2000 [31], and Meingast et al., 2000 [32] the flow velocity at the nozzle hole exit is about 70%–90% of the Bernoulli velocity.

In order to define the velocity components of each blob, the spray cone angle Φ must be known from measurements or has to be estimated using semi-empirical relations [e.g. Hiroyasu and Arai, 1990 (33)]. The direction of the resulting velocity U_{inj} of the primary blob inside the 3D spray cone is randomly chosen by using two random numbers ξ1 and ξ2 in the range of [0, 1] in order to predict the azimuthal angle Φ and the polar angle ψ in the spherical coordinate system, see Fig. 3.2:

$\Phi = 2\pi\ \xi 1$ (3.3)

$\psi = (\Phi/2)\ \xi 2$ (3.4)

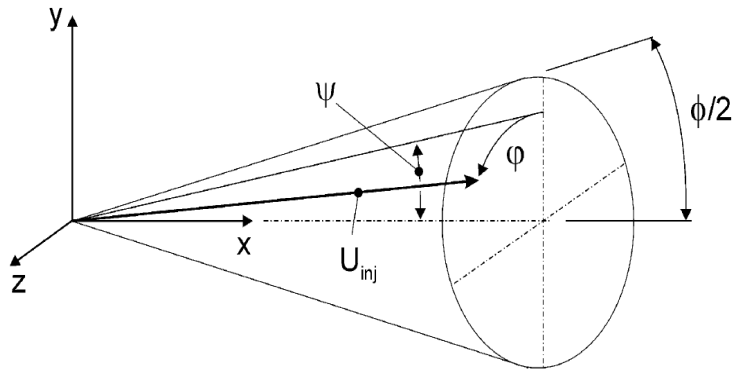

Figure 3.2: 3D spray cone angle and coordinate system . [Baumgarten, 2006 (8)].

Kuensberg et al., 1999 [34] have developed an enhanced blob-method that calculates an effective injection velocity and an effective blob diameter dynamically during the entire injection event taking the reduction of nozzle flow area due to cavitation into account. The given mass flow and the nozzle geometry (length L, diameter D, radius of inlet edge r) are used as input parameters for a one-dimensional analytical model of the nozzle hole flow. During injection, this model determines for every time step whether the nozzle hole flow is turbulent or cavitating.

The static pressure p1 at the vena contracta (point 1 in Fig. 3.3), which can be estimated using the Bernoulli equation for frictionless flow from point 0 to point 1, must be lower than the vapor pressure pvap in the case of cavitating flow and higher in the case of turbulent flow. In Eq.

$$p_1 = p_0 - \frac{\rho_l}{2} u_{vena}^2 \qquad (3.5)$$

3.5, the inlet pressure P_0 and the velocity u_{vena} at the smallest flow area are unknown. The inlet pressure P_0 is estimated using again the Bernoulli equation

$$p_0 = p_2 + \frac{\rho_l}{2}\left(\frac{2(p_0 - p_2)}{\rho_l}\right) = p_2 + \frac{\rho_l}{2}\left(\frac{u_{mean}}{C_d}\right)^2 \qquad (3.6)$$

where $U_{mean} = m_{inj} /(A_{hole} \rho_l)$ is the average velocity inside the hole assuming slug flow and

$$C_d = \frac{\dot{m}_{inj}}{\dot{m}_{Bernoulli}} = \frac{\rho_l A_{hole} u_{mean}}{\rho_l A_{hole} u_{Bernoulli}} = \frac{u_{mean}}{\left(2(p_0 - p_2)/\rho_l\right)^{0.5}} \tag{3.7}$$

is the discharge coefficient. By using tabulated inlet loss coefficients (k_{inlet}) and the Blasius or the laminar equation for wall friction, the discharge coefficient is given by

$$C_d = \left(k_{inlet} + f \cdot L/D + 1\right)^{-0.5}, \tag{3.8}$$

$$f = \max\left(0.316 \cdot Re^{-0.25}, 64/Re\right) \tag{3.9}$$

Assuming a flat velocity profile and using Nurick's expression for the size of the contraction at the vena contracta [Nurick WH, 1976 (35)].

$$A_{vena} = A_{hole} C_c, \quad C_c = \left[\left(\frac{1}{C_{c0}}\right)^2 - 11.4\frac{r}{D}\right]^{-0.5} \tag{3.10}$$

where $C_{c0} = 0.61$. Mass conservation gives the velocity at the smallest flow area:

$$u_{vena} = \frac{\dot{m}_{inj}}{A_{hole} C_c \rho_l} = \frac{u_{mean}}{C_c} \tag{3.11}$$

At the beginning and end of injection, the flow is usually turbulent, the blob size equals the nozzle hole diameter D, and the injection velocity is calculated using Eq. 3.1. During the main injection phase, the flow is usually cavitating, see Fig. 3.3. In this case, the effective cross-sectional area of the nozzle hole exit A_{eff} is smaller than the geometrical area A_{hole} resulting in a decrease of the blob diameter,

$$D_{eff} = \sqrt{\frac{4A_{eff}}{\pi}} \tag{3.12}$$

While the injection velocity is increased. A momentum balance from the vena contracta (point 1) to the hole exit (point 2), together with the conservation of mass,

$$\dot{m}_{inj} = \rho_l u_{vena} A_{hole} C_c = \rho_l u_{eff} A_{eff} \tag{3.13}$$

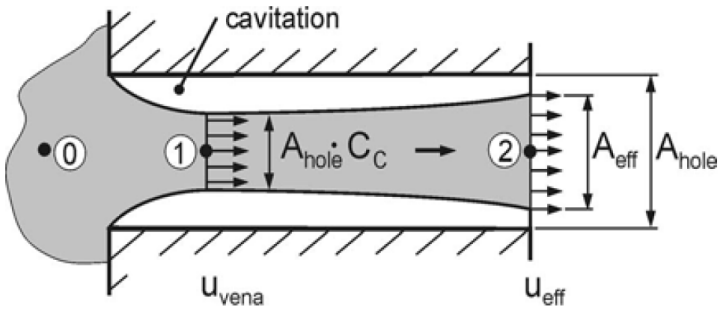

Figure 3.3: One Dimensional cavitating nozzle hole flow . [Baumgarten, 2006 (8)].

gives the injection velocity

$$u_{eff} = \frac{A_{hole}}{\dot{m}_{inj}}\left(p_{vap} - p_2\right) + u_{vena} \tag{3.14}$$

where

$$u_{vena} = \frac{\dot{m}_{inj}}{\rho_l A_{hole} C_c} \tag{3.15}$$

The effective flow area in Eq. 3.12 is

$$A_{eff} = \dot{m}_{inj} / \left(u_{eff}\, \rho_l\right) \tag{3.16}$$

Compared to the original blob-method, the dynamic calculation of blob size and injection velocity during the whole injection event introduces the effect of cavitation by decreasing the initial blob size and estimating a more realistic initial velocity. However, only the passive effect of cavitation, the reduction of flow area, is considered. The increase of turbulence and break-up energy due to cavitation bubble implosions is not included.

Altogether, the blob method is a simple and well-known method of treating the primary break-up in Eulerian-Lagrangian CFD codes. As far as there is no detailed information about the composition of the primary spray, and measurements about the spray cone angle are available, it is the best way to define the initial starting conditions for the liquid entering the combustion chamber. Nevertheless, this method does not represent a detailed physical and satisfying modeling of the relevant processes during primary break-up. The most important disadvantage is that the influence of the 3D nozzle hole flow on 3D spray angle and drop size distribution cannot be mapped and that the promotion of primary break-up by turbulence and by implosions of cavitation bubbles outside the nozzle is not regarded at all. [Baumgarten, 2006 (8)]. Blob-method is of our great interest hence part of the simulation and analysis were done for this research based on this method.

3.1.2 Other Methods

Distribution function method is another way of model atomization both for full-cone spray and hollow-cone spray. This method assumes that the fuel is already fully atomized at the nozzle exit andthat the distribution of drop sizes can be described by mathematical functions. In this case, a distribution of droplet sizes is injected. In high-pressure sprays, neither the droplet sizes nor their distribution in the dense spray near the nozzle could be quantified experimentally up to now. Thus the droplet size distribution must be guessed and iteratively adjusted until the measured drop sizes in the far field of the nozzle are similar to the simulated ones. This of course does not represent a detailed modeling of the relevant processes during primary break-up, but can be used as an alternative to the mono-disperse injection of the blob-method. [Baumgarten, 2006 (8)].

Turbulence-induced break up method is another one. Huh and Gosman, 1991 [38] have published this phenomenological model of turbulence induced atomization for full-cone diesel sprays, which is also used to predict the primary spray cone angle. The authors assume that the turbulent forces within the liquid emerging from the nozzle are the producers of initial surface perturbations, which grow exponentially due to aerodynamic forces and form new droplets. The wavelength of the most unstable surface wave is determined by the turbulent length scale. The turbulent kinetic energy at the nozzle exit is estimated using simple overall mass, momentum, and energy balances. [Baumgarten, 2006 (8)].

Arcoumanis et al., 1997 [24] have developed a primary break-up model for full-cone diesel sprays that takes cavitation, turbulence, and aerodynamic effects into account. In order to link the spray characteristics with the nozzle hole flow which is known as cavitation induced breakup. [Baumgarten, 2006 (8)].

Nishimura and Assanis, 2000 [39] have presented a cavitation and turbulence-induced primary break-up model for full-cone diesel sprays that takes cavitation bubble collapse energy into account.

Sheet atomization model for hollow cone sprays is another method for direct Injection spark ignition (DISI) engines.

3.2 Secondary Breakup

Secondary break-up is the disintegration of already existing droplets into smaller ones due

to the aerodynamic forces that are induced by the relative velocity u_{rel} between droplet and surrounding gas. These forces result in an instable growing of waves on the droplet surface or of the whole droplet itself, and finally lead to its disintegration. The surface tension force on the other hand tries to keep the droplet spherical and counteracts the deformation force. As discussed in the previous chapter, this behavior is expressed by a non-dimensional number, the gas phase Weber number. The models used in order to simulate secondary break-up processes in full-cone as well as hollow-cone fuel sprays are described in the next sections.

3.2.1 Kelvin-Helmholtz Break-Up Model

The Kelvin-Helmholtz model (KH model) was proposed by Reitz, 1987 [2]. The model is based on a first order linear analysis of a Kelvin-Helmholtz instability growing on the surface of a cylindrical liquid jet with initial diameter r_0 that is penetrating into a stationary incompressible gas with a relative velocity u_{rel}. Both the liquid and the gas are assumed to be incompressible, and the gas is assumed to be in viscid. Furthermore, it is assumed that due to the turbulence generated inside the nozzle hole the jet surface is covered with a spectrum of sinusoidal surface waves with an infinitesimal axis-symmetric displacement $\acute{\eta} = \acute{\eta}_0 \cdot e^{\omega t}$ ($\acute{\eta} << r$) causing small axis-symmetric fluctuating pressures as well as axial and radial velocity components in both liquid and gas. These surface waves grow because of aerodynamic forces due to the relative velocity between liquid and gas (shear flow waves), Fig. 3.4. The motion of liquid and gas are described by the linearized Navier-Stokes equations for both phases. The solution is found by transforming the equations of motion into stream and potential functions.

The analysis, which is described in detail in Reitz and Bracco, 1986 [15], yields a dispersion equation relating the growth rate ω (increase of amplitude per unit time) of a perturbation to its wavelength $\lambda = 2\pi / k$:

$$\begin{aligned}
&\omega^2 + 2\nu_l k^2 \omega \left(\frac{I_1'(kr_0)}{I_0(kr_0)} - \frac{2kl}{k^2+l^2} \frac{I_1(kr_0)}{I_0(kr_0)} \frac{I_1'(lr_0)}{I_1(lr_0)} \right) \\
&= \frac{\sigma k}{\rho_l r_0^2} \left(1 - r_0^2 k^2\right) \left(\frac{l^2 - k^2}{l^2 + k^2} \right) \frac{I_1(kr_0)}{I_0(kr_0)} \\
&+ \frac{\rho_g}{\rho_l} \left(u_{rel} - \frac{i\omega}{k} \right)^2 k^2 \left(\frac{l^2 - k^2}{l^2 + k^2} \right) \frac{I_1(kr_0) K_0(kr_0)}{I_0(kr_0) K_1(kr_0)} ,
\end{aligned} \tag{3. 17}$$

Where I_0 and I_1 are modified Bessel functions of the first kind, K_0 and K_1 are modified Bessel functions of the second kind, $k = 2\pi/\lambda$ is the wave number, σ is the surface tension, $l^2 = k^2 + \omega / \upsilon_l$, $\upsilon_l = \mu_l / \rho_l$ (kinematic viscosity), and the prime indicates differentiation.

The numerical solution of the dispersion function shows that there is a single maximum in the wave growth rate curve ω = ω(k). It is assumed that the wave with the highest growth rate ω = Ω will finally be sheared off the jet and form new droplets. Curve fits were generated from the numerical solutions to Eq. 3.17 for the growth rate Ω of the fastest growing and thus most unstable surface wave,

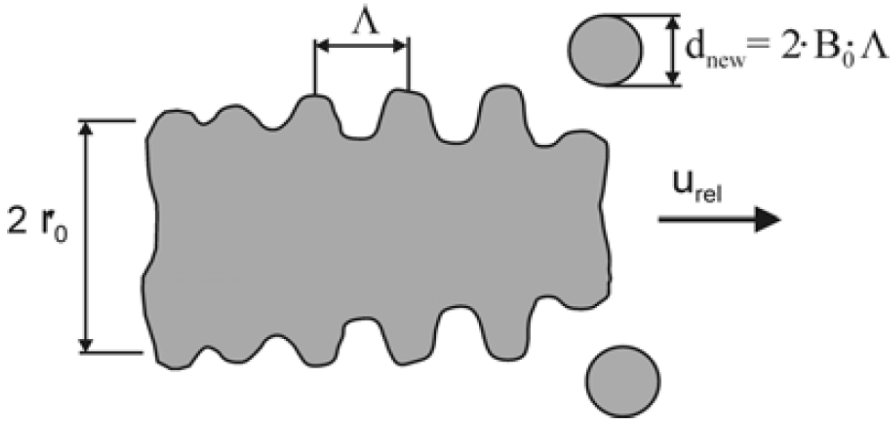

Figure 3.4: Schematic Illustration of the Kelvin-Helmholtz Model. . [Baumgarten, 2006 (8)].

$$\Omega\left[\frac{\rho_l r_0^3}{\sigma}\right]^{0.5} = \frac{0.34 + 0.38 \cdot We_g^{1.5}}{(1+Z)\left(1+1.4 \cdot T^{0.6}\right)} \tag{3.18}$$

and the corresponding wavelength Λ,

$$\frac{\Lambda}{r_0} = 9.02 \frac{\left(1+0.45 \cdot Z^{0.5}\right)\left(1+0.4 \cdot T^{0.7}\right)}{\left(1+0.865 \cdot We_g^{1.67}\right)^{0.6}} \tag{3.19}$$

Where

$$Z = \frac{\sqrt{We_l}}{Re_l},\ T = Z\sqrt{We_g},\ We_g = \frac{\rho_g r_0 u_{rel}^2}{\sigma},\ We_l = \frac{\rho_l r_0 u_{rel}^2}{\sigma},\ Re_l = \frac{\rho_l r_0 u_{rel}}{\eta_l}.$$

Z and T are the Ohnesorge number and the Taylor number, and r_0 is the radius of the undisturbed jet. These curve fits are shown in Figs. 3.5 and 3.6.

Reitz, 1987[2] applied this theory to the break-up modeling of liquid droplets with radius r. Again, waves grow on the drop surface with growth rate Ω and wavelength Λ. Because the new child drops are formed from the surface waves that are sheared off the parent drops, it is assumed that the size of the new droplets is proportional to the wavelength Λ,

$r_{new} = B_0.\Lambda$ (3.20)

where $B_0 = 0.61$ is a constant, the value of which is fixed. A new parcel containing product drops of size r_{new} is created and added to the computations. In contrast to the TAB model, the parent drop does not perform a complete break-up, but continuously looses mass while penetrating into the gas. This results in a shrinking radius whose rate of reduction at a certain time t depends on the difference between the actual value of droplet radius r and an equilibrium droplet size (which is equal to the child droplet radius r_{new}) as well as on the value of a characteristic time span τ_{bu}, (Reitz, 1987 [2], Ricart et al., 1997 [40]):

$$\frac{dr}{dt} = -\frac{r - r_{new}}{\tau_{bu}}, \qquad \tau_{bu} = 3.788 \cdot B_1 \frac{r}{\Lambda \cdot \Omega}. \tag{3.21}$$

If the KH model is used in combination with the blob method, the influence of the nozzle hole flow on primary break-up is not modeled satisfactorily. In this case, B1 is an adjustable model constant including the influence of the nozzle hole flow like turbulence level and nozzle design on spray break-up. Values between $B_1 = 1.73$ and $B_1 = 60$ are proposed in the literature [Patterson MA, Reitz RD , 1998(41); Reitz, 1987(2)]. A higher value of B_1 leads to reduced break-up and increased penetration, while a smaller value on the other hand results in increased spray disintegration, faster fuel-air mixing, and reduced penetration.

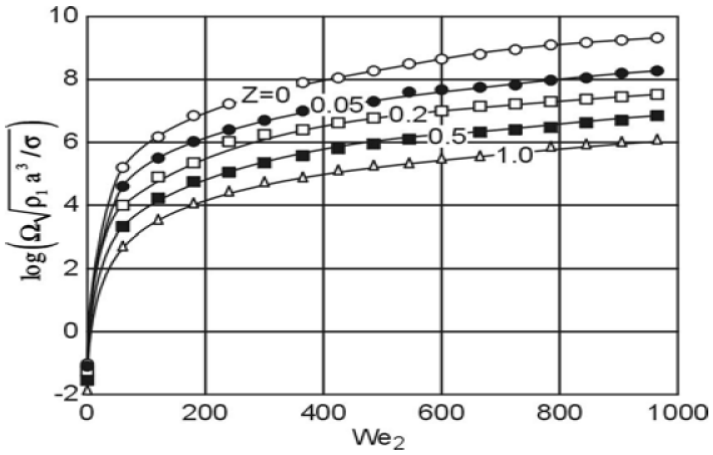

Figure 3.5: Growth rate of the most unstable surface wave versus Weg as a function of Ohnesorge number Z. . [Baumgarten, 2006 (8)].

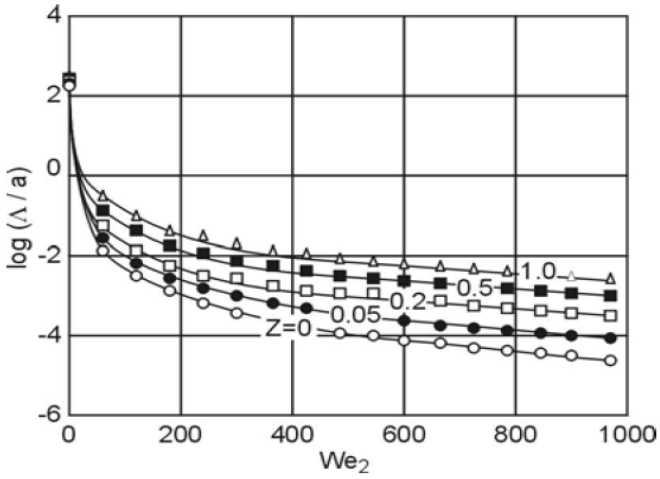

Figure 3.6: Wavelength of the most unstable surface wave versus Weg as a function of Ohnesorge number Z. . [Baumgarten, 2006 (8)].

The number of new child droplets per time step can be calculated from the decrease of radius of the parent drop (Eq. 3.21) and the size of the new child drops (Eq. 3.22). The new child droplets become parent drops in a new parcel and are subject to further break-up. [Baumgarten, 2006 (8)].

The KH model predicts a bimodal size distribution consisting of a small number of big parent drops, the radius of which is slowly shrinking, and an increasing number of small child droplets. Although stripping break-up is one of the most important break-up mechanisms in the case of high-pressure injection, experiments (Hwang SS, Liu Z, Reitz RD, 1996 [42]) have shown that the formation of strong bimodal droplet size distributions is unrealistic, and that another important mechanism, the sudden disintegration of the complete drop into droplets with diameter much bigger that the Khchild droplets is important near the nozzle. For this reason, the KH-model is usually combined with the Rayleigh-Taylor model, which is described in the following section.

3.2.2 Rayleigh-Taylor Break-Up Model

The Rayleigh-Taylor model (RT model) is based on the theoretical work of Taylor, 1963 [43], who investigated the instability of the interface between two fluids of different densities in the case of an acceleration (or deceleration) normal to this interface. If the two fluids are liquid and gas, the interface is stable when the acceleration is directed into the liquid, and instable disturbances can grow if the acceleration is directed into the gas. Regarding droplet and gas moving with velocity urel relative to each other, the deceleration of the drop (in the forward direction) due to drag forces can also be treated as an acceleration of the drop in the direction of the airflow (backward

direction). Thus, unstable waves can grow on the back side of the drop, see Fig. 3.7. The disintegration of the drop is induced by the inertia of the liquid if drops and ligaments leaving the nozzle with high velocities are strongly decelerated by the aerodynamic drag force

$$F_{aero} = \pi r^2 c_D \frac{\rho_g u_{rel}^2}{2} \tag{3.22}$$

Dividing the drag force by the mass of the drop, the acceleration of the interface can be found,

$$a = \frac{3}{8} c_D \frac{\rho_g u_{rel}^2}{\rho_l r} \tag{3.23}$$

where C_D is the drag coefficient of the drop. Using a linear stability analysis (Chang, 1991 [44]) and neglecting liquid viscosity (Bellmann and Pennington, 1954 [45]), the growth rate Ω and the corresponding wavelength Λ of the fastest growing wave are:

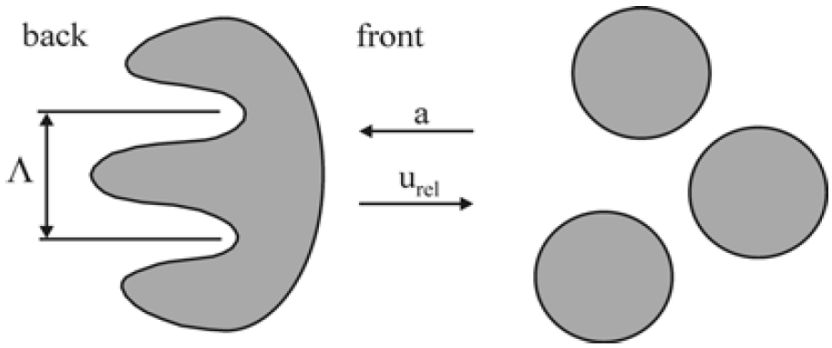

Figure 3.7: Rayleigh-Taylor instability on a liquid drop . [Baumgarten, 2006 (8)].

$$\Omega = \sqrt{\frac{2}{3\sqrt{3\sigma}} \frac{\left[a\left(\rho_l - \rho_g\right)\right]^{3/2}}{\rho_l + \rho_g}} \tag{3.24}$$

and

$$\Lambda = C_3 2\pi \sqrt{\frac{3\sigma}{a\left(\rho_l - \rho_g\right)}}\,. \tag{3.25}$$

In many applications, the gas density is neglected because it is much smaller than the liquid density. The break-up time $t_{bu} = \Omega^{-1}$ is found to be the reciprocal of the frequency of the fastest growing wave. At $t = t_{bu}$ the drop disintegrates completely into small droplets whose radius $d_{new} = \Lambda$ is

assumed to be proportional to the wavelength. The drop is only allowed to break up if Λ is smaller than its diameter. The number of new drops is calculated using the mass conservation principle (Patterson MA, Reitz RD, 1998 [107]). In contrast to this method, Su et al., 1996 [46] determine the number of new droplets as the ratio of maximum diameter of the deformed drop to Λ , and the size of the new droplets is calculated using mass conservation. [Baumgarten, 2006 (8)].

The adjustable constant C_3 is introduced in order to allow a modification of the effective wavelength. Similar to the constant B1 in the KH model, it includes the unknown effects of initial conditions like turbulence and cavitation inside the nozzle hole on the secondary break-up. C_3 changes the size of the new product droplets and the likelihood of break-up events. By increasing its value, break-up is reduced (break-up is only allowed if $\Lambda < d_{drop}$), and the size of the new droplets is increased. Patterson and Reitz, 1998 [41] use values in the range of $C_3 = 1.0–5.33$.

It has been observed that drag-deceleration and shear flow induced instabilities are simultaneous phenomena in the droplet break-up process (Hwang et al., 1996 [42]). The drag-deceleration induced RT break-up only results in effective and rapid disintegration near the nozzle, where the very high relative velocities between drop and gas result in a strong deceleration. Further downstream, the shear flow induced KH break-up becomes the dominant process. Hence, the RT model is always used in combination with a second break-up model, usually the KH model. [Baumgarten, 2006(8)].

3.3 Combined Model

Because a single break-up model is usually not able to describe all relevant classes of break-up processes and break-up regimes of engine sprays, the use of combined models, consisting of a combination of at least two different break-up models, is becoming more and more popular in order to improve the accuracy of prediction. Usually such a model is composed of a primary and a secondary break-up model. The most important hybrid models for full-cone and hollow-cone sprays are presented in the following.

3.3.1 Blob KH/RT Model (Full Cone Spray)

The experimental investigations of Hwang et al., 1996 [42] revealed that the break-up mechanism in the catastrophic break-up regime consists of a series of characteristic processes. The aerodynamic force on the drop flattens it into the shape of a liquid sheet, and the decelerating sheet

breaks into large-scale fragments by means of RT instability. KH waves with a much shorter wavelength originate at the edges of the fragments, and these waves break up into micrometer-size drops as illustrated in Fig. 3.8. If the blob-method is utilized in order to inject initial drops into the numerical grid, usually two secondary break-up models are used. The first one describes the relevant processes of the spray disintegration near the nozzle (part of the primary break-up that is not correctly described by the blob-method), and the second one is responsible for the remaining spray region. In the case of the KH-RT model, both models are implemented in CFD codes in a competing manner. Both models are allowed to grow unstable waves simultaneously, and if the RT-model predicts a break-up within the actual time step, the disintegration of the whole drop according to the RT mechanism occurs. Otherwise the KH model will produce small child droplets and reduce the diameter of the parent drop. [Baumgarten, 2006 (8)].

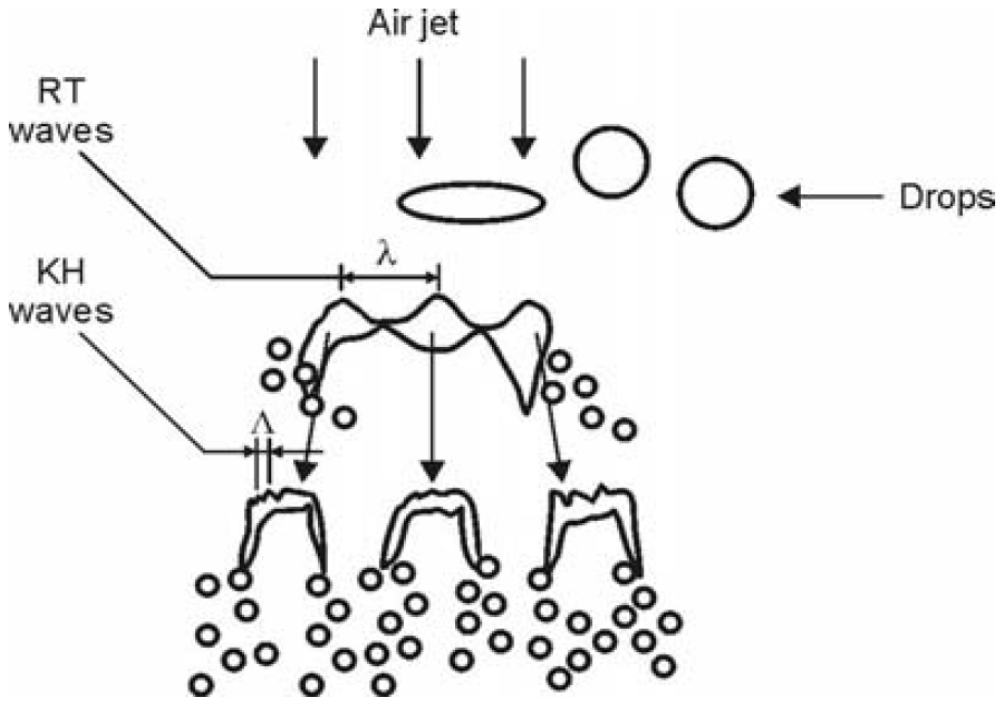

Figure 3.8: A Schematic diagram of break-up mechanisms in the catastrophic break-up regime. . [Baumgarten, 2006 (8)].

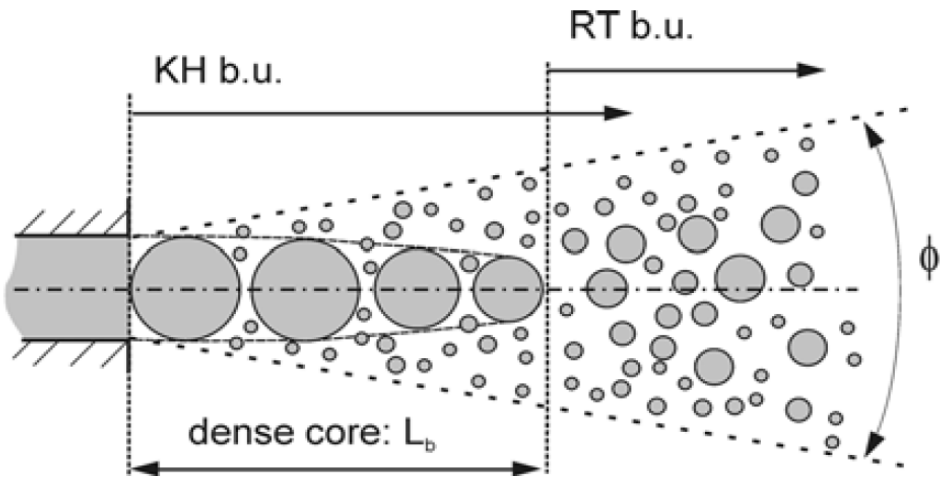

Figure 3.9: A Combined blob KH/RT model . [Baumgarten, 2006 (8)].

However, the reduction of droplet size by the RT model is too fast if it is applied to drops just leaving the nozzle hole. Thus, the model is applied to spray break-up beyond a certain distance from the nozzle, the break-up length L_b of the dense fragmented core and only KH stripping break-up is allowed to occur near the nozzle as shown in Fig. 3.9. Hence, the secondary break-up process can be adjusted by modifying the break-up length, L_b as well as the constants of the KH model and the RT model. Compared to the single use of the KH model, a faster disintegration of big drops is achieved, and an increased evaporation as well as a reduced penetration are calculated allowing a better matching of experimental data. Another positive effect of the combination of RT and KH model is that the RT model counteracts the formation of a strong bimodal droplet size distribution, because RT break-up always results in a number of equally sized droplets with intermediate size.

The KH-RT model is the most popular of all hybrid models used today. It has been successfully validated against experimental data and used by many authors in order to predict the disintegration process of high-pressure diesel sprays. [Baumgarten, 2006 (8)].

3.4 Huh's Model

In the present study, developed atomization models for round hole diesel injectors are employed named as Huh's atomization model (Huh and Gosman, 1991 [38]).

This model couples effects of two phenomena relevant in spray atomisation, namely, the turbulent fluctuations in the liquid jet and the unstable wave growth at the jet surface by

aerodynamic effects between the jet and surrounding gas at their interface The conceptual picture of the atomisation process takes it to proceed in two stages:

1. Turbulence developed in the nozzle hole induces initial perturbations on the jet surface when it leaves the hole.
2. Once the perturbations have reached a certain level, they grow by the action of aerodynamic forces until they become detached from the jet surface as droplets; these droplets will, from now on, be called secondary droplets.

An one-dimensional analysis of the single phase flow in the nozzle the cavitation phenomenon is at this stage neglected gives the initial values of turbulence length and time scales in the jet at the nozzle exit. However, both scales are subjected to changes since the jet turbulence decays with time as the jet travels downstream This is because there are no mechanisms in the jet which can generate turbulence once it has left a nozzle In the nozzle hole, due to the no-slip condition at the hole wall, the liquid experiences tangential stresses from the wall, leading to turbulence generation. It is postulated that the turbulence causes perturbations at the jet surface with wavelengths proportional to the turbulence length scales. Under the action of surrounding gas i.e. its normal pressure, stresses at the jet surface, the amplitude of these perturbations starts to rise. The rate of this amplitude amplification is characterized by a corresponding time scale, called a wave growth time. This time scale, together with the aforementioned turbulence time scale, determine the atomization time scale. Both atomization scales, time and length, together with the average injection velocity, are used to estimate a spray cone angle. The sizes of secondary droplets are determined by a random choice from an assumed probability distribution function (pdf). It is taken that the pdf for the droplet sizes is proportional to the spectrum of the turbulence kinetic energy in the jet, and inversely proportional to the atomization time scale. The initial velocities of secondary droplets are taken to be equal to their parent drops. Under normal diesel conditions cavitation usually occurs within the nozzle in validating the assumed single phase flow assumption. In order to allow for this effect to some extent simple overall mass, momentum and energy balances are used to estimate the exit jet characteristics. Also, the determination of a number of model coefficients by reference to measurements for the real diesel conditions, implicitly accounts for cavitation.

3.5 CFD And Modeling For Spray

The use of detailed physical and chemical models has become a fundamental pre-requisite for a realistic simulation of the combustion process in Diesel engines [G. D'errico, T. Lucchini (2011)(47)]. Advanced spray models with reduced grid dependency are required to describe the fuel-air mixing processes, together with detailed chemistry to predict the complex oxidation of multi-component fuel mixtures under conventional and new combustion modes. Computational Fluid Dynamics (CFD) usually integrates the experimental activity carried out at the test-bench to investigate the combustion process and is now part of the industrial design and analysis. The use of detailed chemistry seems absolutely necessary to describe new combustion modes, predict the main pollutant emissions [3] and evaluate the effects of multiple injections. Furthermore, a fundamental prerequisite for a successful CFD simulation is a correct prediction of the fuel-air mixing process because it influences both the auto-ignition and mixing-controlled combustion phases. The need to keep an acceptable compromise in terms of computational time and accuracy justifies the wide use of the Eulerian-Lagrangian approach, where the spray is composed by a discrete number of computational parcels, each one formed by an arbitrary number of droplets with the same properties. Each parcel evolves in the computational mesh according to the mass, momentum and energy exchange with the continuous gas phase which is treated in an Eulerian way. [G. D'errico, T. Lucchini (2011)(47)].

3.5.1 OpenFOAM as a CFD Tool

OpenFOAM is first and foremost a C++ library, used primarily to create executables, known as applications. The applications fall into two categories: solvers, that are each designed to solve a specific problem in continuum mechanics; and utilities, that are designed to perform tasks that involve data manipulation. The OpenFOAM distribution contains numerous solvers and utilities covering a wide range of problems.

One of the strengths of OpenFOAM is that new solvers and utilities can be created by its users with some pre-requisite knowledge of the underlying method, physics and programming techniques involved. OpenFOAM is supplied with pre- and post-processing environments. The interface to the pre- and post-processing are themselves OpenFOAM utilities, thereby ensuring consistent data handling across all environments. The overall structure of OpenFOAM is shown in Figure 3.10.

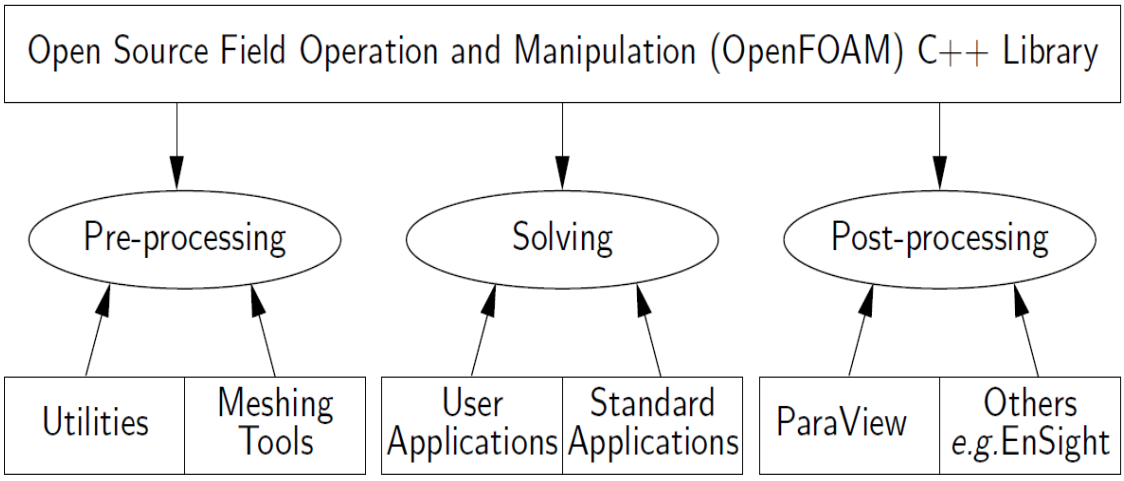

Figure 3.10: Overview of OpenFOAM structure. [48].

3.5.2 Computational Models and Numerical Set Up

As mentioned in the previous section, OpenFOAMÂ©[48] is the tool which is being used here in this work to perform CFD calculations and simulation.This code has a wide range of preimplemented capabilities such as discretisation, numerical and physical models, mesh management and so on. The main advantage of this open-source code is the possibility to implement different models on the same platform and easily compare them. DieselFoam is the solver choosen for this work in which the gas phase is solved in an Eulerian framework, where the equations are considered to be continuous in space and time. On the other hand, the liquid spray is treated by a standard discrete droplet method (DDM) approach, where there is a set of differential equations along the trajectory of

each particle that is solved in order to calculate the change of the location and velocity components of the parcels. Each parcel represents a class of identical, non-interacting droplets, and they are tracked through the physical space in a Lagrangian manner according to the mass, momentum and energy exchange with the gas phase. [R. Novella et all, 2011 (51)].

3.5.2.1 Turbulence Model

In dieselFoam code, turbulent flow is modelled via RANS, a time-averaged version of the Navier–Stokes equations. There are no source terms in the turbulence equations in this solver due to spray interaction and then, turbulence is only influenced by the Lagrangian phase through the momentum transfer and generation of velocity gradients. The turbulence model used in this study was the standard k–ϵ model. The two equations in the k–ϵ model, the turbulence kinetic energy, k,

and its rate of dissipation, ϵ, are obtained from the following transport equations:

$$\frac{\partial}{\partial t}(\rho k) + \frac{\partial}{\partial x_j}(\rho k u_j) = \frac{\partial}{\partial x_j}\left[\left(\mu + \frac{\mu_t}{\sigma_k}\right)\frac{\partial k}{\partial x_j}\right] + G - \rho\epsilon + S_k \tag{3.26}$$

$$\frac{\partial}{\partial t}(\rho\epsilon) + \frac{\partial}{\partial x_j}(\rho\epsilon u_j) = \frac{\partial}{\partial x_j}\left[\left(\mu + \frac{\mu_t}{\sigma_\epsilon}\right) + \frac{\partial\epsilon}{\partial x_j}\right] + \frac{\epsilon}{k}(C_1 G - C_2\rho\epsilon) + S_\epsilon \tag{3.27}$$

where G represents the generation of turbulent kinetic energy due to mean velocity gradients, C_1 and C_2 are empirical coefficients and μ_t is the turbulent viscosity. Even though standard k–ϵ produces higher turbulent viscosity than RNG k–ϵ version, and therefore, the penetrations are on occasion underestimated with standard k–ϵ model, subsequent validations showed that standard k–ϵ fitted the experimental data well if model constants are tuned according to its approximation for round jets. [R. Novella et all, 2011 (51)].

3.5.2.2 Spray Sub Models

The adoption of submodels to describe the spray atomization, breakup and dispersion is necessary while using a DDM [J. Dukowicz, 1980 (52)]. approach. As it is well-known, the atomisation process consists of the liquid core breakup into tiny droplets at the nozzle exit, and together with the secondary droplet breakup, they are one of the most complex phenomena taking place in diesel sprays. At the same time, they have a primary effect on spray behaviour and then on air–fuel mixture formation.

The Kelvin–Helmholtz/Rayleigh–Taylor (KH–RT) hybrid model was adopted in this work. The fundamental mechanisms that govern such spray breakup in the model are the Kelvin–Helmholtz and Rayleigh–Taylor disturbances. In the Kelvin–Helmholtz model the stability analysis provides a dispersion equation that relates the growth of an initial perturbation of infinitesimal amplitude on a liquid surface to its wavelength, and other physical and dynamic parameters of both the injected liquid and the ambient gas. The rate of change of the radius of the parent droplet is calculated using equation 3.21.

The Rayleigh–Taylor model is based on a second type of instability associated with the rapid deceleration of the droplets. If the wavelength of the faster growing wave is smaller than the droplet diameter, the RT waves start to grow on droplet's surface. The life time of the growing RT waves is then tracked from then on, and when the life time exceeds the characteristic breakup time defined in section 3.2.2, a catastrophic break-up occurs and the radii of the new droplet is given by (Eq. 3.25).

CHAPTER 4

4. Experimental Data and Comparison with Simulation

4.1 ECN Sandia

The proposed approaches were validated with different sets of experimental data at non-reacting conditions, which were selected within the Engine Combustion Network (ECN) database. Among the wide range of available experiments, the two conditions which received significant attention from the CFD community correspond to experiments conducted in an optical, constant-volume vessel using as fuel C7H16 (baseline n- heptane) and C12H26 (Spray A).

The purpose of ECN website is to provide an open forum for international collaboration among experimental and computational researchers in engine combustion. Patterned after the Turbulent Non-premixed Flame Workshop, the objectives of the Engine Combustion Network (ECN) are to:

> Establish an internet library of well-documented experiments that are appropriate for model validation and the advancement of scientific understanding of combustion at conditions specific to engines.

> Provide a framework for collaborative comparisons of measured and modeled results.

> Identify priorities for further experimental and computational research.

Maintained by the Engine Combustion Department of Sandia National Laboratories, data currently available on the website includes reacting and non-reacting sprays at conditions typical of diesel combustion, some information regarding engine flows, as well as some information regarding Hydrogen Engine combustion. The website will be expanded in the future to include datasets and modeling results of scientific interest to participants in the ECN. [49].

4.2 Environmental Condition for Experimental Data and Set Up

The Engine Combustion Network collaborates with various institutions to share experimental data, diagnostics, and computational results. Constant Flow test rigs are high temperature and high pressure test chambers, which can simulate the thermodynamic conditions obtained in a Diesel engine, under steady conditions. CMT and Caterpillar both use constant flow

test rigs. The facilities at 'Caterpillar' and 'CMT-Motores Térmicos' have vessels that are able to reach ambient gas temperatures and pressures up to 1000 K and 150 bar.

Pre-burn Combustion vessels are used to generate high temperature, high pressure gases. The ambient pressure, temperature and species at the time of injection are varied by igniting a premixed combustible-gas mixture that burns to completion. Following the spark-ignited premixed combustion, the combustion products cool over a relatively long time (~500 ms) due to heat transfer to the vessel walls and the vessel pressure slowly decreases. IFPEN, Sandia, and TU/e use pre-burn type combustion vessels.

The facility at Sandia National Laboratories has a vessel that is able to range ambient gas temperatures from 450 K to 1400 K, densities from 1 kg/m^3 to 60 kg/m^3 and pressures up to 350 bar.

4.2.1 Spray Combustion

Fuel spray injection is expected to be one of the key elements for enabling high-efficiency, low-emission engines of the future. Understanding the details of the spray combustion process is therefore now more important than ever. But investigating engine combustion processes is challenging due to the many factors that affect the in-cylinder environment where mixing with fuel sprays occurs. The temperature, pressure, density, and composition of the in-cylinder gases as well as fuel injector conditions have a direct effect on combustion and emission-formation processes.

The CRF's Spray Combustion Vessel can simulate a wide range of ambient (charge gas) environments at the time of fuel injection, allowing researchers to assess the effect of each variable with more control than can be achieved in an engine. The capabilities of the combustion vessel are unique in the world. With full optical access, the following ambient conditions can be simulated:

> Ambient gas temperatures from 450 K to 1400 K.

> Ambient gas densities from 1 kg/m^3 to 60 kg/m^3

> Ambient gas oxygen concentrations from 0% to 21%.

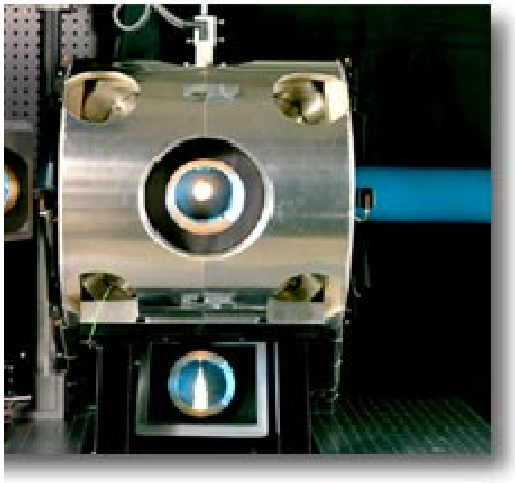

Figure 4.1: Optically accessible high-temperature, high-pressure spray chamber.(American's Combustion research facility [50]).

Advanced optical diagnostics are used to study the sprays in a fundamental manner. The data obtained in this facility are used both to guide engine design and to help improve computational fluid dynamic models, which in turn are used to optimize engine designs. The wide range of conditions employed in the chamber permit model validation with many different boundary conditions. An extensive dataset from this laboratory is available to download at the Engine Combustion Network, which seeks to advance the state of the art in engine combustion modeling.

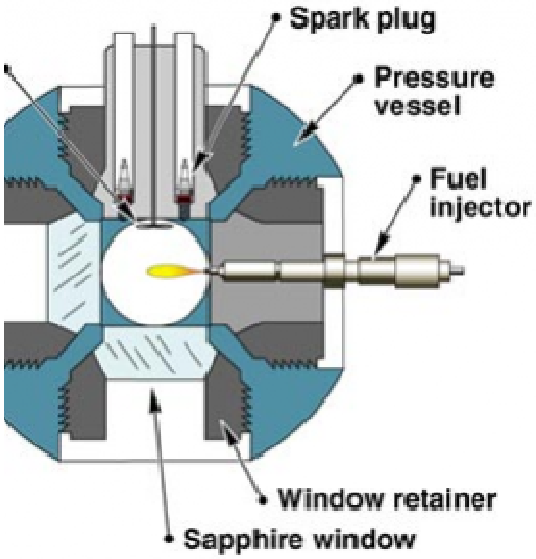

Figure 4.2: Schematic of combustion vessel. (American's Combustion research facility [50]).

A picture of the inside of the combustion vessel is shown in Fig. 4.3 Visible objects include the spark plugs, mixing fan, injector, intake valves, and a beaded thermocouple. Two spark plugs

are used to produce consistent combustion in the high-density, fuel-lean environment. The spark gap located is 16.5 mm below the vessel top and at a radius of 31.8 mm relative to center of vessel. Electrode diameter is 3.2 mm. Ground strap diameter is 1.6 mm. Ground strap leads (in-line with the electrode) are separated by 21 mm (Engine Combustion Network [49]).

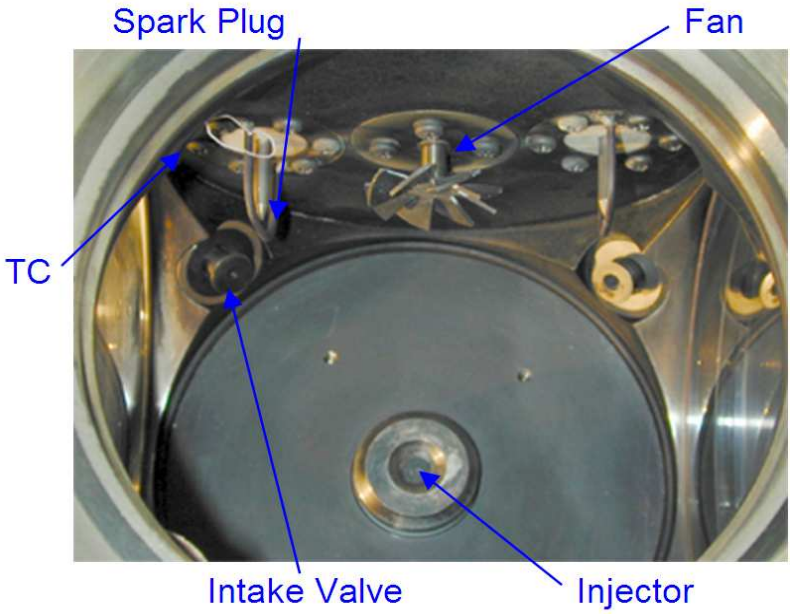

Figure 4.3: Inside of the combustion vessel. (Engine Combustion Network [49]).

The mixing fan at the center is operated at 8000 rpm to ensure uniform ambient conditions at the time of injection. The bottom of the fan is approximately 15 mm below the vessel top. The outer diameter of the fan is 25 mm. There are eight fan blades, oriented at a 30 degree angle relative to horizontal, attached to a 7 mm disk at the center. Fan blades are 0.85 mm thick.

Intake and exhaust valves, or instruments such as pressure transducers or thermocouple inputs, are mounted at the corners of the cubical-shaped combustion chamber. Figure 4.3 and the solid model of the chamber volume (Fig. 4.4) show that the edge of the cube is an extension of the 105 mm cylindrical ports with a 19.05 mm port hole going exactly through the corner of the cube. Closed valves are recessed a depth of 4 mm from the highest part of the extended cylinder ports. Note that the windows are recessed some from the 105 mm bored port diameter, so that the effective cube dimension is 108 mm. The injector protrudes into the vessel consequently affecting the vessel geometry.

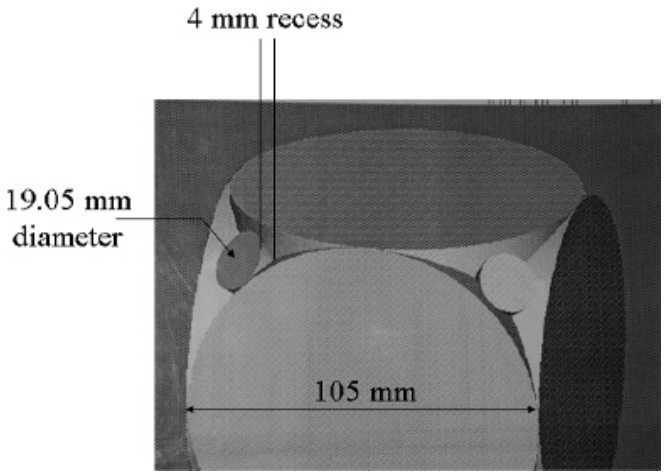

Figure 4.4: The solid model of the chamber volume. (Engine Combustion Network [49]).

This combustion vessel has been operational at Sandia since 1997 and is currently in use. Prior to this time, a disk-shaped combustion vessel was used. The disk-shaped combustion will not be described here but the ambient conditions generated were similar to the current facility and data obtained in the disk-shaped chamber (jet penetration) is included in the ECN database. (Engine Combustion Network [49]).

4.2.2 Details of the Thermal and Fluid Mechanic Conditions in the Combustion Vessel

Prior to an experiment, the vessel is heated to 458 K. This is the approximate temperature of combustible gases prior to spark ignition. A mixing fan mounted in the upper surface of the vessel runs throughout the entire simulation process. The fan serves to keep the temperature in the vessel uniform before and after spark ignition and up to the time of the diesel injection event. A fan that pulls gas from the center of the vessel and ejects it along the walls was found to provide the optimal uniformity in the core region of the vessel. Without the mixing fan, more significant temperature non uniformities develop as a result of vertical thermal stratification of the gas in the vessel.

Velocity Estimates of the mean gas velocity induced by the fan were made using a particle tracking technique used to visualize the flow in the chamber. The mean swirl velocity was approximately 0.7 m/s. This velocity is comparable to the velocity measured with LDV in the disk-shaped chamber, where the same mixing fan and fan speed were used. LDV measurements from this disk-shaped chamber also showed that the rms velocity was 0.7 m/s in the central core region of the vessel. Note that these gas velocities are small when compared to liquid (high-momentum)

spray velocities (~400 to 600 m/s) and therefore, have little effect on the sprays.

Temperature The thermal environment during the pressure decrease in the combustion vessel was measured with a fine wire (0.05 mm diameter) platinum/platinum-rhodium (type-R) thermocouple. The thermocouple reading was corrected for radiation errors and transient response to temperature changes, but the corrections had little effect (<0.5% of mean) on the ambient temperatures of interest for diesel combustion (800-1200 K). This temperature range is well below that of combustion flame temperatures where radiation corrections are more of a concern. (Engine Combustion Network [49]).

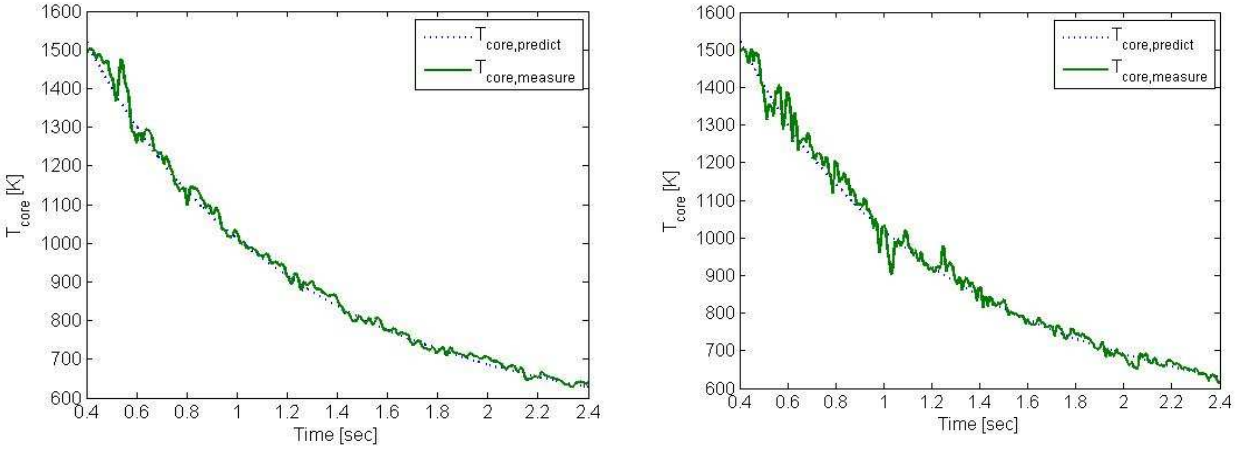

Figure 4.5.1 & 4.5.2: The measured temperature is shown as function of time. (Engine Combustion Network [49]).

The measured temperature is shown as function of time in Fig. 4.5.1 & 4.5.2 for an ambient density of 14.8 kg/m^3 and ambient oxygen concentration of 0%. The measurement position was at x = 20 mm, y = 0 mm, z = 0 mm, where x is axial distance, y is vertical cross-stream position (up or down), and z is horizontal cross-stream position (left or right), all relative to the injector wall. This location is in the "core" region of the vessel, defined as the initial location of gases that mix with the spray during injection. Temperature measurements are shown for two different cool-down events in the figure.

The measured core temperature is compared to a predicted average core temperature for the vessel. The predicted core temperature (*Tc*), which is the temperature reported as the ambient gas temperature for a given dataset (i.e. Ta), is obtained by first calculating the mass-averaged bulk temperature (*Tb*). The bulk temperature is determined from the real-gas equation of state (*P* =

$Z \cdot R \cdot \rho b \cdot Tb/MW$) using the measured pressure and initial mass-averaged bulk density (bulk density is constant for an experiment), and the molecular weight (*MW*) and compressibility factor (*Z*) of the ambient gas. *Z* varies from 1.0 to 1.05 for conditions experienced in the combustion vessel. Note that the core temperature is higher than the bulk temperature because cooler, higher density gases exist in boundary layers of the vessel. This point is often overlooked in engine or combustion vessel experiments. A related point is that the core density is lower than bulk density. For comparison, bulk temperatures and densities are therefore also included in the database (i.e. T_{Bulk}).

A simple relationship, considering the cooler vessel wall temperature (*Tw*), is used to relate*Tb* to*Tc* , as shown in Eq. (4.1)

$$\frac{T_c}{T_b} = 1 + a \cdot \left(1 - \frac{T_w}{T_b}\right) + b \cdot \left(\frac{T_b}{T_w} - 1\right). \qquad (4.1)$$

The second term on the right accounts for cooler, higher density gases in the boundary layers and the third term on the right accounts for cooler, higher density gases in the crevices and corners of the vessel. Values for a and *b* were determined from an empirical fit to the average measured temperature for many cool-down events at a given ambient gas density. For the ambient density of Fig. 4.5.1 & 4.5.2 (14.8 kg/m^3), *Tc/Tb* ranges from a value of 1.05 at 1300 K, to 1.02 at 700 K. Figures 4.5.1 & 4.5.2 shows that local gas temperature, measured with a thermocouple at a single location, fluctuates about the predicted core temperature during the cool-down process. In addition, the magnitude of the temperature fluctuations may change from one simulation to the next at a given time in the cool down.

The temperature fluctuations are the result of time-dependent differences in the initial combustion process as well as heat transfer processes during the cool down event as the fan stirs the contents of the vessel-temperature variations are therefore expected. The magnitude of the temperature variation is shown in the histogram of the measured temperature normalized by the predicted temperature (Fig. 4.6). The histogram is for instantaneous temperature measurements from 10 cool-down events for predicted core temperatures ranging from 700-1300 K. The histogram is based on core temperature, rather than time, to give equal weighting for each temperature. The histogram reflects a normal

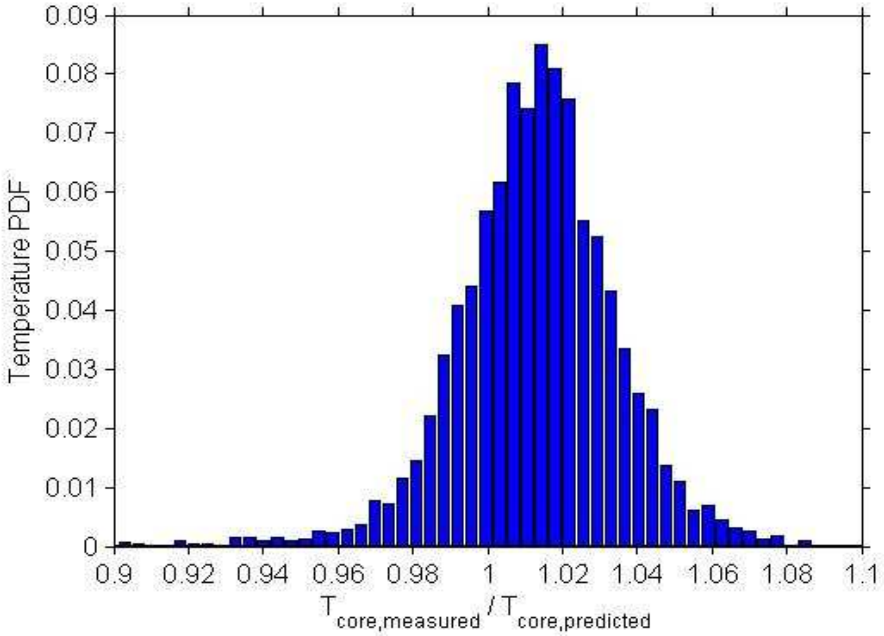

Figure 4.6: The magnitude of the temperature variation of the measured temperature normalized by the predicted temperature. (Engine Combustion Network [49]).

distribution with a standard deviation (σ) of 2.1% of the mean. Related to the normal distribution, 70% of the measured temperatures are within ±2.1% of the mean (±σ) and 95% of the measured temperatures are within ±4.2% of the mean (±2σ). These temperature fluctuations are one likely explanation for any variation in system performance from injection to injection.

For this particular measurement station and density, the measured mean temperature is 1% higher than the predicted core temperature. However, there is some variation in mean temperature for different combustion vessel locations. The normalized measured temperature along the spray axis (y = 0, z = 0) before injection is shown in Fig. 4.7 for six different axial positions for an ambient gas density of 20 kg/m^3. The mean temperature from 40 cool-down events is plotted against bulk temperature. The measurements show that the mean temperature varies by ± 1% along the axis of the spray, with slightly cooler regions near the injector or back walls. The ratio of predicted core temperature to measured temperature also changes by less than ± 1%. Temperature measurements outside of the spray axis are shown in Fig. 4.8. There is little change in temperature to the right, left, or along the x-axis direction, except near the vessel wall. The most significant variation is in the vertical direction where the temperature varies by ± 2% for a vertical change of ± 25 mm. Note, however, that sprays typically spread less than ± 15 mm from the spray axis over the length of the vessel so the vertical temperature variation may be less significant. Moreover, systematic combustion asymmetries in the vertical direction (i.e. ignition site, or lift-off length)

have not been found. (Engine Combustion Network [49]).

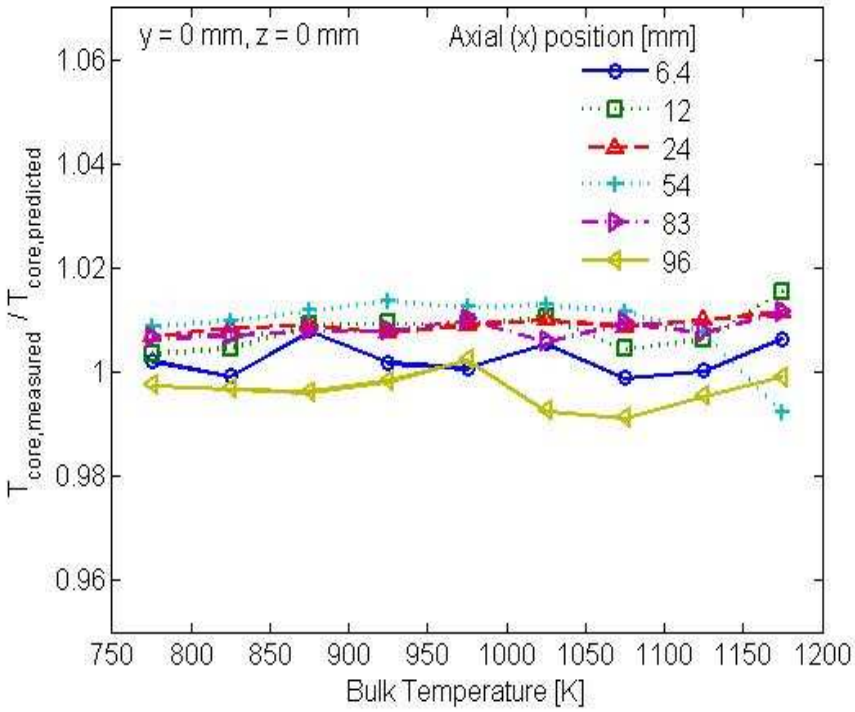

Figure 4.7: The normalized measured temperature along the spray axis (y = 0, z = 0) before injection. (Engine Combustion Network [49]).

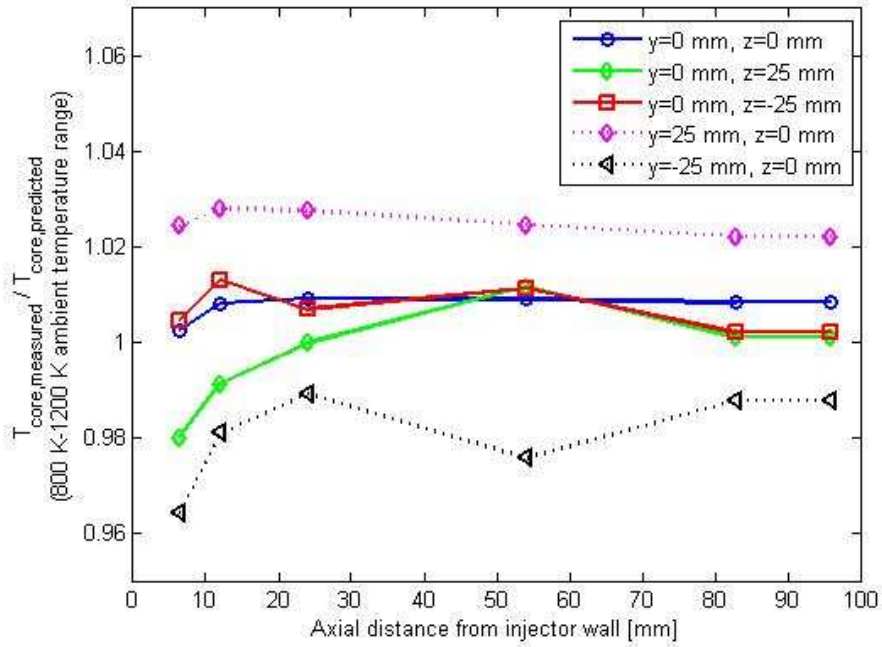

Figure 4.8: Temperature measurements outside of the spray axis. (Engine Combustion Network [49]).

In summary, a large core region exists in the combustion vessel where mean temperatures are uniform for an extensive range of ambient temperatures. Instantaneous fluctuations in temperature (shown Fig. 4.5.1 & 4.5.2) do exist, however, and are likely to affect the diesel combustion process, as well as injection-to-injection variability.(Engine Combustion Network [49]).

4.2.3 Ambient Conditions at the Time of Fuel Injection

The procedure for simulating diesel experimental conditions is illustrated by a combustion vessel pressure history shown in Fig. 4.9. To begin the simulation procedure, the vessel is filled to a specified density with a premixed, combustible-gas mixture. This mixture is then ignited with spark plugs, creating a high-temperature, high-pressure environment through an initial premixed combustion. As the products of combustion cool over a relatively long time (~1 s) due to heat transfer to the vessel walls, the pressure slowly decreases. When the desired experimental conditions are reached, the diesel fuel injector opens and auto ignition and combustion processes ensue as shown by the second pressure rise in Fig. 4.9 at 930 ms. The ambient gas temperature, density, and composition at injection are determined by the pressure at the time of fuel injection and the initial mass and composition of gas within the vessel. (Engine Combustion Network [49]).

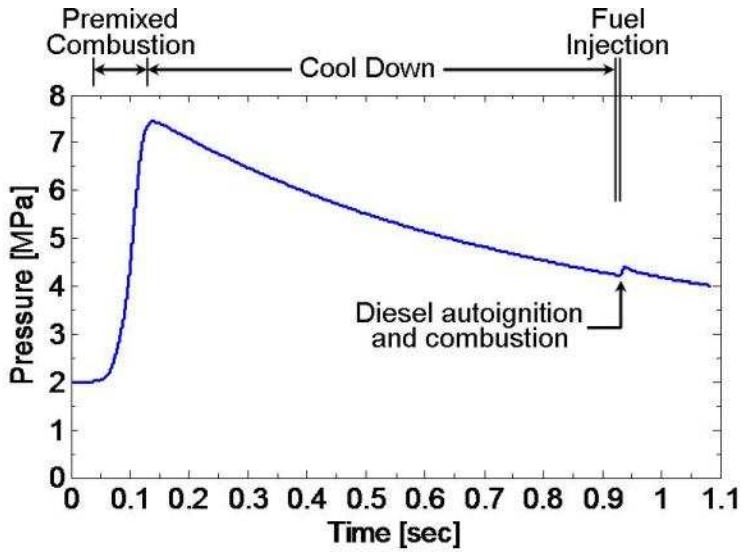

Fig. 4.9. Simulation to produce core ambient conditions of 1000 K, 14.8 kg/m^3, 21% O2 at the time of diesel fuel injection. (Engine Combustion Network [49]).

For Fig. 4.9, the ambient conditions were intended to simulate air (21% O2). The following reaction gives the reactant and product compositions of the premixed combustible gas mixture used to generate the high-pressure, high-temperature, 21%-O2 environment:

$$3.053 \cdot C2H2 + 0.509 \cdot H2 + 28.888O2 + 69.33 \cdot N2 \rightarrow 21.00 \cdot O2 + 69.33 \cdot N2 + 6.11 \cdot CO2 + 3.56 \cdot H2O \quad (4.2)$$

The reactants consist of acetylene (C2H2), hydrogen (H2), oxygen (O2) and nitrogen (N2). The reaction is normalized to produce 100 moles of product and assumes that complete-combustion products are generated.

Other environments, such as exhaust-gas-recirculation use in engines, or an inert ambient (0% O2), were simulated by changing the reactant O2 and N2 concentrations. Table 4.1 shows the mole fraction and molecular weight of the reactants and products for a given ambient oxygen concentration. Like Eq. (4.2), the products listed in Table 4.1 are assumed to be complete-combustion products.

Table 4.1. Percentages of ambient gas at the time of diesel injection and reactants prior to spark ignition. (Engine Combustion Network [49]).

Products (composition at diesel injection time)					**Reactants (prior to spark ignition)**			
O2	N2	CO2	H2O	MW	rC2H2	rH2	rO2	rN2
21	69.33	6.11	3.56	29.47	3	0.5	28.38	68.12
20	70.3	6.13	3.57	29.43	3.01	0.5	27.42	69.07
19	71.27	6.15	3.58	29.4	3.02	0.5	26.46	70.02
18	72.24	6.17	3.59	29.36	3.03	0.5	25.5	70.97
17	73.21	6.19	3.6	29.32	3.04	0.5	24.54	71.92
16	74.18	6.21	3.61	29.28	3.05	0.5	23.59	72.87
15	75.15	6.23	3.62	29.24	3.06	0.5	22.63	73.82
14	76.12	6.24	3.63	29.21	3.07	0.5	21.67	74.77
13	77.09	6.26	3.64	29.17	3.08	0.5	20.71	75.72
12	78.06	6.28	3.65	29.13	3.09	0.5	19.75	76.67
11	79.04	6.3	3.66	29.09	3.1	0.5	18.79	77.61
10	80.01	6.32	3.67	29.06	3.1	0.5	17.83	78.56
9	80.98	6.34	3.68	29.02	3.11	0.5	16.87	79.51
8	81.95	6.36	3.69	28.98	3.12	0.5	15.91	80.46
7	82.92	6.38	3.7	28.94	3.13	0.5	14.96	81.41
6	83.89	6.4	3.71	28.91	3.14	0.5	14	82.36
5	84.86	6.42	3.72	28.87	3.15	0.5	13.04	83.31
4	85.83	6.44	3.73	28.83	3.16	0.5	12.08	84.26
3	86.8	6.46	3.74	28.79	3.17	0.5	11.12	85.21
2	87.77	6.48	3.75	28.75	3.18	0.5	10.17	86.15

To investigate the assumption of complete-combustion products in this simulation procedure, gas sampling of the exhaust from the combustion vessel (without diesel fuel injection) was performed and shows agreement with values given in Table 4.1. In addition, single-zone,

closed-reactor (Senkin module of Chemkin) simulations were performed using detailed chemistry (52 species, GRI Mech. 3.0) to determine if other minor species are likely present at the time of diesel injection. The simulation was initialized using the above reactants and initial temperature and pressure of Fig. 4.9. The closed-reactor was held at constant-volume shortly before ignition and then changed to a slowly expanding volume to simulate the vessel cool-down process. Figure 4.10 shows temperature (top) and mole fraction of OH (middle) and all minor species (bottom) (all species except CO2, H2O, O2, and N2) during the cool down. Two different product-gas simulations are shown: 21% O2 and 0% O2. The closed-reactor predictions indicate that minor species mole fraction decreases as temperature decreases. For typical diesel conditions (800-1000 K), the OH mole fraction drops below 1 ppm and less than 0.02% of all combustion products are minor species—indicating that the product compositions given in Table 4.1 for major species are close approximations for boundary conditions at the time of diesel injection.

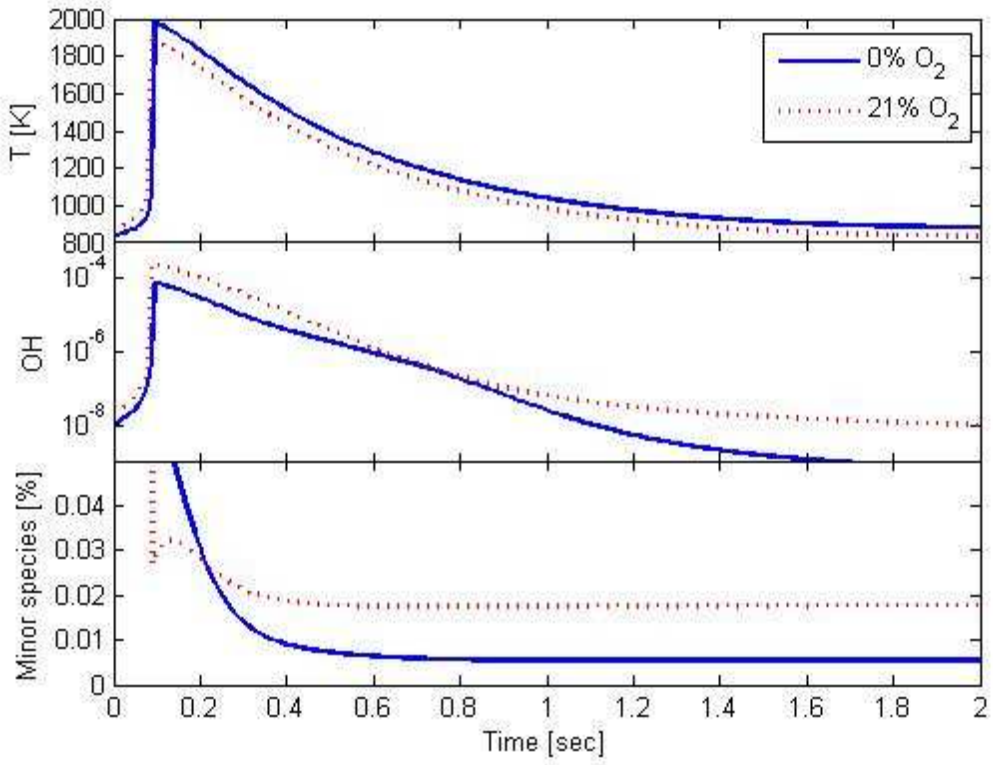

Figure 4.10: temperature (top) and mole fraction of OH (middle) and all minor species (bottom) (all species except CO2, H2O, O2, and N2) during the cool down. (Engine Combustion Network [49]).

As shown in Fig. 4.9, the pressure rise caused by the diesel fuel injection is typically small relative to the premixed burn pressure rise. This is because of the large mass of ambient gas in the vessel relative to the mass of fuel injected. However, the pressure rise during the time of fuel

injection does compress surrounding (unmixed) ambient gases, however, which increases the ambient temperature and density. Estimates for the change in ambient temperature can be made using isentropic compression, as performed to process lift-off length measurements obtained after the time of combustion. Therefore, two ambient temperatures may be given in the database: one before ignition and the other after ignition. For the conditions of Fig. 4.9, heat release from the diesel injection causes only a small change (less than 2%) in estimated ambient temperature. Conditions where the temperature rise is more significant include low ambient density (low mass in vessel) or large-nozzle, high-injection-pressure conditions (high mass of fuel injected). (Engine Combustion Network [49]).

4.2.4 Details of the Thermal and Fluid Mechanic Conditions in the Combustion Vessel for Spray-A

Figure 4.11 shows the average gas temperature at various positions in the "core" region of the vessel, relative to predictions based on a single relationship between Tcore and Tbulk (i.e., using only the measured pressure to predict Tcore). Along the axis of the spray, the gas temperature is uniform within 1%, except for a measurement point in the boundary layer only 1 mm in front of the injector tip. Temperature is also uniform along the same horizontal plane (z = 0, y = ±15 mm) outside of the spray. The most significant variation is in the vertical direction (z = ±15 mm, y = 0) where the temperature varies by ± 4% for a vertical change of ± 15 mm. This vertical stratification is obviously caused by buoyancy effects. (Engine Combustion Network [49]).

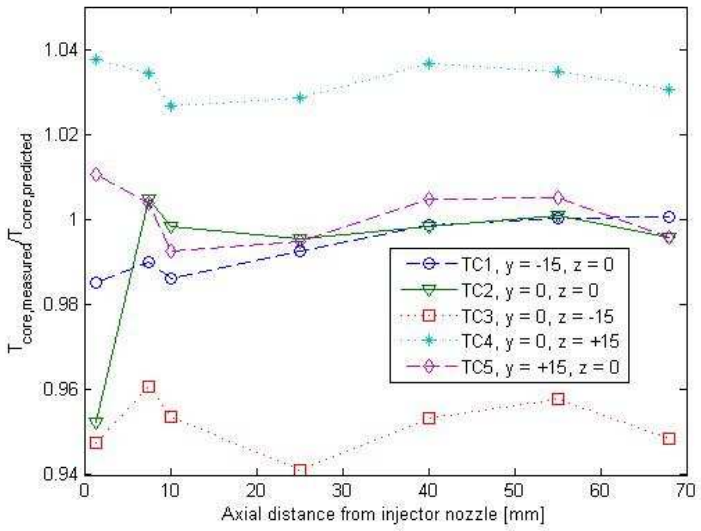

Figure 4.11: Average gas temperature in the "core" region of the combustion vessel at Spray A conditions, 0% O2.(Engine Combustion Network [49]).

4.2.5 Injector Characterization

Injection rate profiles, and the discharge and area-contraction coefficients were measured by injecting onto a force transducer and simultaneously collecting and weighing injected fuel. The experimental method and explanation of the orifice coefficients is discussed below. As the development of a spray is dependent on both the mass and momentum flow rates from an orifice, two orifice coefficients are needed to characterize these flow rates. The discharge coefficient is the product:

$$C_d = C_a \cdot C_v \,. \tag{4.3}$$

where Cv is the velocity coefficient. Using Cv and Ca, the mass flow rate (mf) and momentum flow rate (Mf) from an orifice are given by the following:

$$\dot{m}_f = C_a \cdot A_f \cdot \rho_f \cdot C_v \cdot U_b \,, \tag{4.4}$$

$$\dot{M}_f = \dot{m}_f \cdot C_v \cdot U_b \,, \tag{4.5}$$

where U_b is given by Bernoulli's equation:

$$U_b = \sqrt{2 \cdot [P_f - P_a]/\rho_f} \,. \tag{4.6}$$

The term ρ_f is the fuel density, Af is the orifice exit area, and Pf and Pa are the fuel and ambient gas pressures, respectively. The velocity U_b is the maximum potential fluid velocity at the orifice exit, while the product $Cv \cdot U_b$ is the average velocity at the orifice exit over the area $Ca \cdot A_f$. The orifice area-contraction coefficients were determined from the spray momentum measured with a force transducer and the following relationship derived from Eqs.(3-6):

$$C_a = 2 \cdot A_f \cdot C_d^2 \cdot [P_f - P_a]/\dot{M}_f \tag{4.7}$$

The spray momentum was measured with a piezoelectric pressure transducer calibrated to measure the force (i.e., the momentum) induced by a spray impinging on the transducer diaphragm. The transducer was placed approximately 3mm in front of the orifice. This distance was close enough to the orifice that the entire spray impinged on the central region of the transducer diaphragm, but far enough away that the flow through the orifice was not restricted.

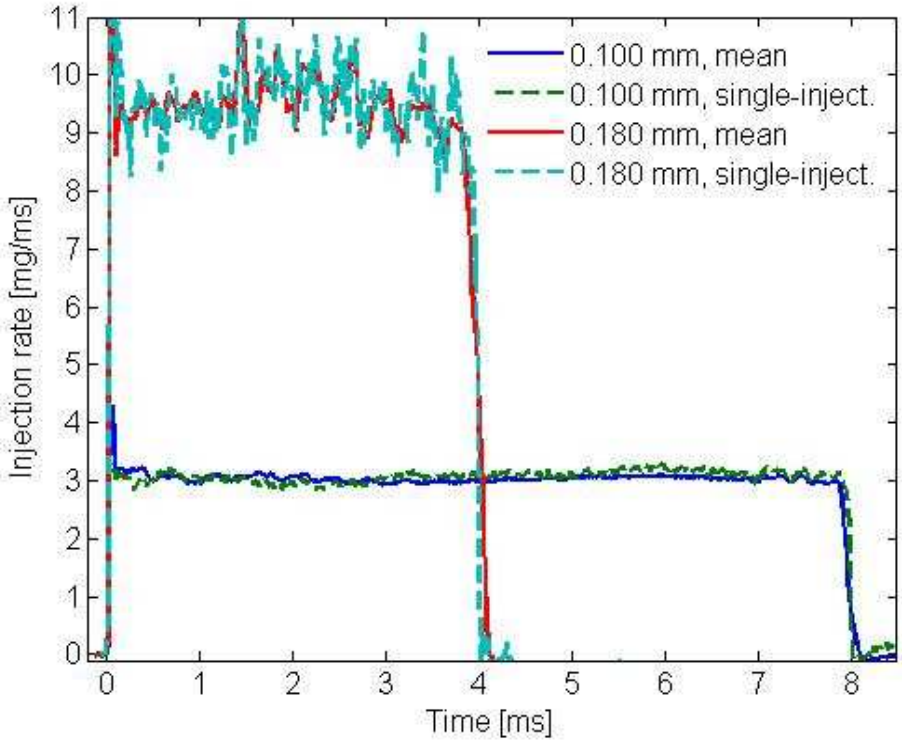

Figure 4.12: Injection rates for two orifices with an injection pressure above ambient of 138 MPa and using diesel fuel at room temperature (300 K). (Engine Combustion Network [49]).

Figure 4.12 shows injection rates for two orifices with an injection pressure above ambient of 138 MPa and using diesel fuel at room temperature (300K). The injection period is much longer for the small orifice to inject approximately the same total mass. Injection rates are shown for a single injection, as well as the average of 60 injections. The injection rate profiles show that the opening and closing of the injector occurs in less than 0.1 ms. (The spike at the beginning of injection may be an artifact of mass accumulation at the head of the spray, as the force transducer was a finite distance away from the orifice.) The closing time is shorter for a single injection compared to the mean because of small injection-to-injection variability. Injection is nearly steady during the time of injection, creating a square-wave injection rate shape. The square-wave shape was also found for the off-axis injector tips. As opening and closing times are small, the average momentum (Mf) during the steady-flow period was used to determine the orifice coefficients (e.g. Eq. 4.7). (Engine Combustion Network [49]).

4.3 Comparison with Simulations

4.3.1 Methodology

The general methodology followed in this work consists mainly of comparing the CFD modeling results against those obtained experimentally available at the well-validated public database for n-heptane and dodecane (Spray A) fuel generated by Sandia National Laboratories [49] for non reacting case. In this research, the additional complexity related to modeling real engines is avoided by simulating a single n-heptane spray and single spary A injected individually into a constant volume vessel.

The comparisons are being made in terms of liquid and vapor penetration. Mixture fraction along axial and radial directions are also compared.

As mentioned in the previous section, OpenFOAM©[48] is the tool which is being used here in this work to perform CFD calculations and simulation.This code has a wide range of pre implemented capabilities such as discretisation, numerical and physical models, mesh management and so on. The main advantage of this open-source code is the possibility to implement different models on the same platform and easily compare them. DieselFoam is the solver choosen for this work in which the gas phase is solved in an Eulerian framework, where the equations are considered to be continuous in space and time. On the other hand, the liquid spray is treated by a standard discrete droplet method (DDM) approach, where there is a set of differential equations along the trajectory of each particle that is solved in order to calculate the change of the location and velocity components of the parcels. Each parcel represents a class of identical, non-interacting droplets, and they are tracked through the physical space in a Lagrangian manner according to the mass, momentum and energy exchange with the gas phase. [R. Novella et all, 2011 (51)].

CHAPTER 5

5. Results and Discussion

The proposed approaches were validated with different sets of experimental data at non-reacting conditions, which were selected within the Engine Combustion Network database. Among the wide range of available experiments, the two conditions which received significant attention from the CFD community correspond to experiments conducted in an optical, constant-volume vessel using as fuel C7H16 (baseline n-heptane) and C12H26 (Spray A). The vessel has a cubical-shaped combustion chamber, whose characteristic dimension is 108. The fuel injector is located in one side port using a metal insert that forms the right wall of the combustion chamber. Optical access is provided by four sapphire windows with clear apertures of 102 mm located in the other four ports [49]. This combustion vessel has been operational at Sandia since 1997 and is currently in use [G. D'errico, T. Lucchini (2011) (47)].

The combustion chamber (108 mm X 108 mm X 108 mm) which is considered for our simulation is shown below.

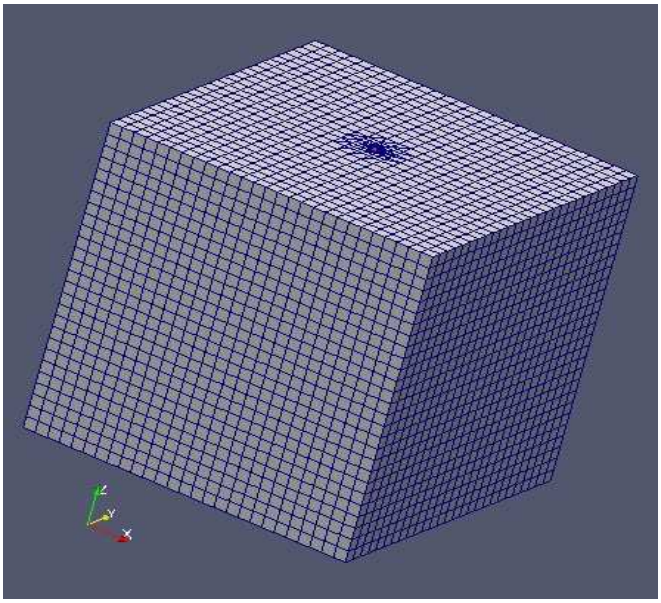

Figure-5.1: Combustion Chamber and Position of Fuel Injector for the simulation.

A cutting plane in the middle of the combustion chamber with the spray can be overviewed like below

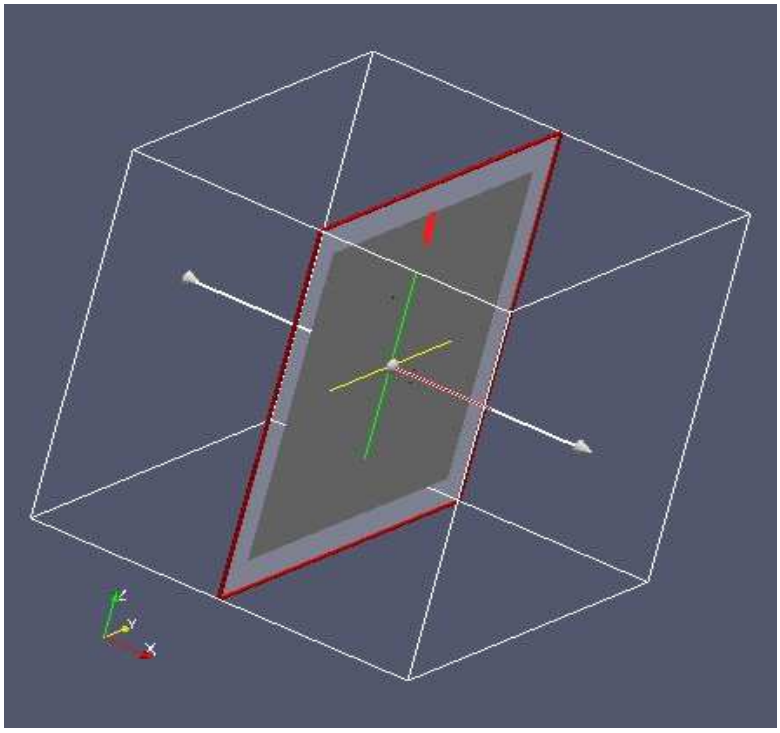

Fugure- 5.2 : Cutting plane on the combustion chamber to analyze post processing data in paraview.

In this paper we will validate our simulation with corresponding some experimental data for following two cases:

a) Using KHRT model

b) Using Huh-Gosman methodology

We also change the terbulence model constant for both the cases. As discussed before in section 3.5.2.1 of chapter 3 we can understand that k–ϵ tubulence model can be expressed by following transport equations

$$\frac{\partial}{\partial t}(\rho k) + \frac{\partial}{\partial x_i}(\rho k u_i) = \frac{\partial}{\partial x_j}\left[\left(\mu + \frac{\mu_t}{\sigma_k}\right)\frac{\partial k}{\partial x_j}\right] + P_k + P_b - \rho\epsilon - Y_M + S_k \quad (5.1)$$

$$\frac{\partial}{\partial t}(\rho\epsilon) + \frac{\partial}{\partial x_i}(\rho\epsilon u_i) = \frac{\partial}{\partial x_j}\left[\left(\mu + \frac{\mu_t}{\sigma_\epsilon}\right)\frac{\partial \epsilon}{\partial x_j}\right] + C_{1\epsilon}\frac{\epsilon}{k}(P_k + C_{3\epsilon}P_b) - C_{2\epsilon}\rho\frac{\epsilon^2}{k} + S_\epsilon \quad (5.2)$$

Equation (5.1) is known as turbulent kinetic energy (k) equation and equation (5.2) as dissipation rate (ϵ) equation. The standard value of model constants are as follows:

$C_1 = C_{1\epsilon} = 1.49 \sim 1.52$

$C_2 = C_{2\epsilon} = 1.92$

$C_3 = C_{3\epsilon} = -0.33$ (only for compressible case)

In our simulation we changed the value of C_1 as 1.49 and 1.52. Consequently, by doing this we are changing turbulence effect. We will increase the intensity of turbulence by changing the value from 1.49 to 1.52. The main purpose of doing this is to describe the mixture process accurately. Other constants like C_2, C_3 always remains constant and same as mentioned above.

5.1 Baseline n-Heptane

The so-called baseline n-heptane is not currently active experimentally, but it has been the focus of several previous studies. A blob fuel injector with a single, axial hole is used. The orifice has a 0.1 mm diameter, a discharge coefficient Cd equal to 0.8, a area-contraction coefficient Ca equal to 0.91 at 72 MPa and 0.86 at 138 Mpa. The length-to-diameter ratio, L/d, is equal to 4.0. In the non-reacting conditions the oxygen concentration is equal to 0 and the ambient temperature and density are respectively equal to 1000 k and 14.8 kg/m3. Simulation were carried out using Huh Injector as well.

If the vapor penetration is correctly predicted for a long time, the combustion model will probably succeed for most of the operating conditions which can be encountered in Diesel engines (Idicheria, C. A., Pickett, L. M., 2007[53]). First-order numerical schemes were used for these simulations to preserve the results stability and to be consistent with the typical case setup which is used for the simulations of Diesel engines.[G. D'errico, T. Lucchini (2011) (47)].

All the different cases taking fuel as n-heptane along with simulated and experimental results are described below:

5.1.1 Results for Different Conditions

5.1.1.1 Using KHRT Model

For KHRT model we use two different injectors in the simulation. Once it is done using Blob injector which is really popular due to its easy and accurate prediction. Again KHRT model simulation has been performed by using blob injector.

5.1.1.1.1 Using Blob Injector

The first observed quantity for our simulation case is spray penetration. As discussed above, using blob KHRT model we perform our simulation for two different values of $C_{1.}$ The results were compared with the experimental value. Figure 5.3 shows the comparison with the simulated and experimental values.

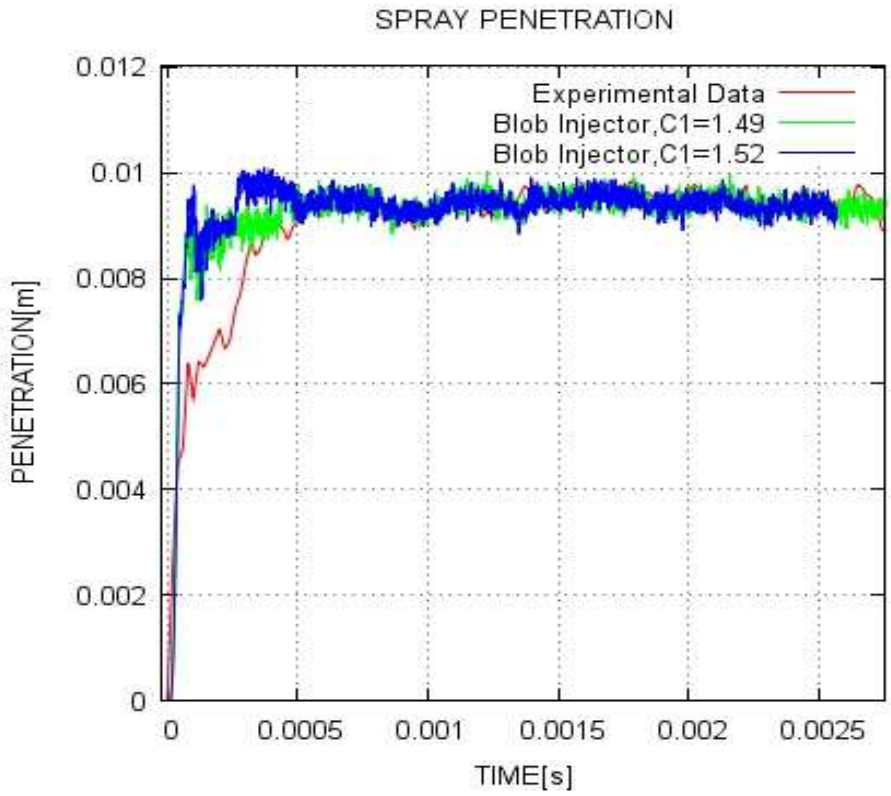

Figure 5.3 :Validation of Spray penetration comparing with experimental data (ECN Sandia [49]) and simulated data for Blob injector model with two different values of constant C_1 of k–ϵ turbulence model.

From figure 5.3 we can obseve that change of the turbulent model constant, C_1 has no affect for the simulation for a steady spary. For both the cases we get very good similarity with the experimental values. Taking C_1 = 1.52 has a better similarity in the transient condition though if we deeply compare with the spray pattern that we got taking C_1 value as 1.49.

Validation were also performed taking consideration of vapor penetration data. And like previous case for different values of turbulence model constant we get the following result as shown in figure 5.4.

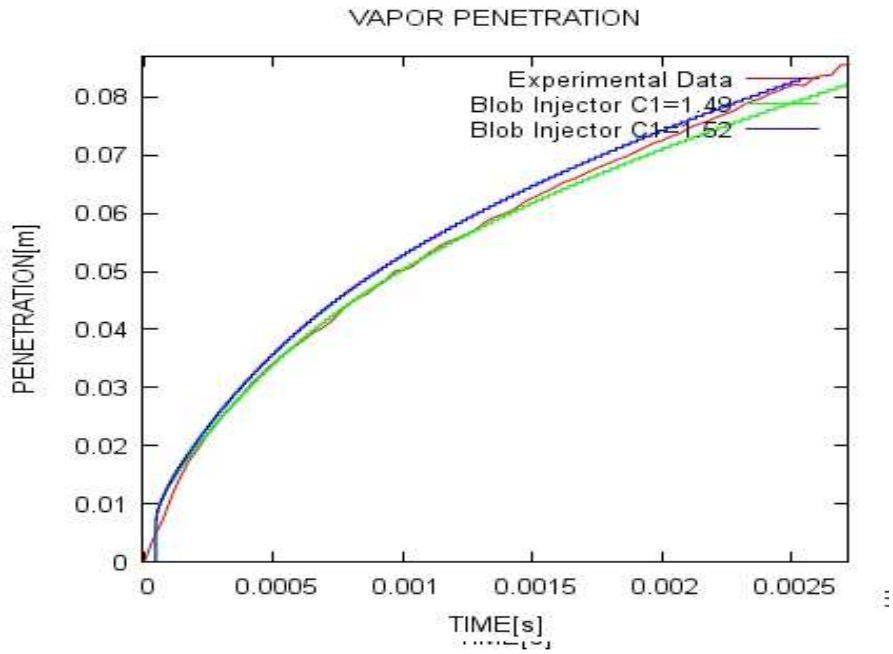

Figure 5.4 :Validation of vapor penetration comparing with experimental data (ECN Sandia [49]) for Blob injector model with two different values of constant C_1 of k–ϵ model.

From figure 5.4 we can obserb that simulated results have almost exact similarity with the experimental data. For validating a spray model vapor penetration data has a greater importance. If the vapor peretration data matches with the experimental data for so long time, the model can be concluded as a valid one.

To assess the model capability to correctly reproduce both the auto-ignition and the mixing controlled combustion phases, not only the spray and vapor tip penetrations must be considered, since these data are not completely representative of the fuel-air mixing process, but, when possible, radial distributions of the mixture fraction at different distances from the injector must be compared [53]. Consequently, our model was compared with the experimental data of both the axial and radial mixture fraction. For comparison, data are taken for both transient and steady state condition of spray. We took the data different time steps like 0.5 milisecond (ms), 0.7 ms, 0.9ms and 1.15 ms. The corresponding experimental data were taken for 0.49 ms, 0.68 ms, 0.9 ms and 1.13 ms respectively. We can represent our data in the following figures:

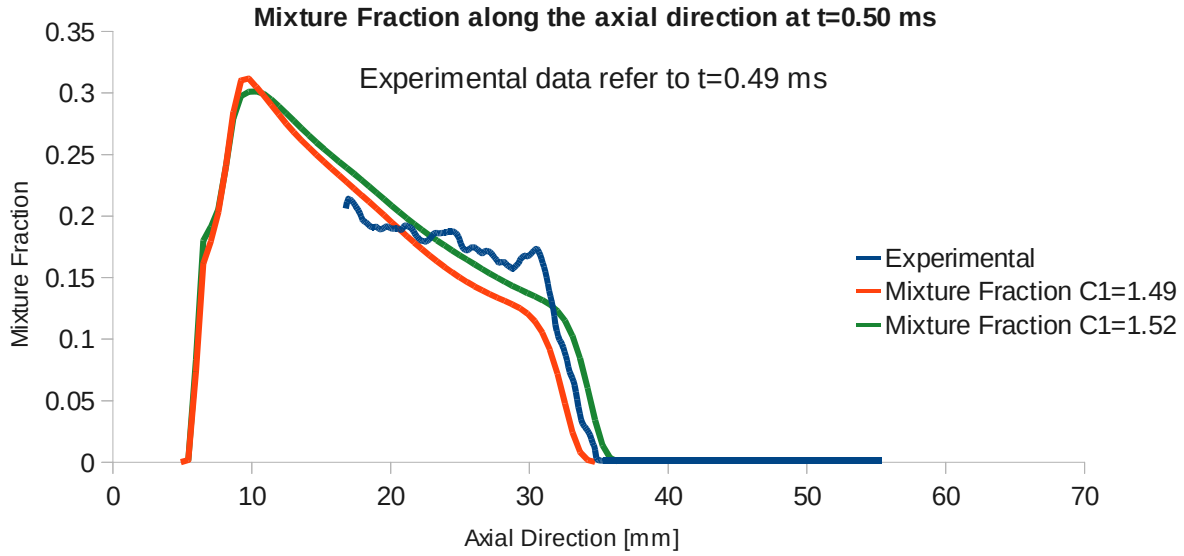

Figure: 5.5 [A]

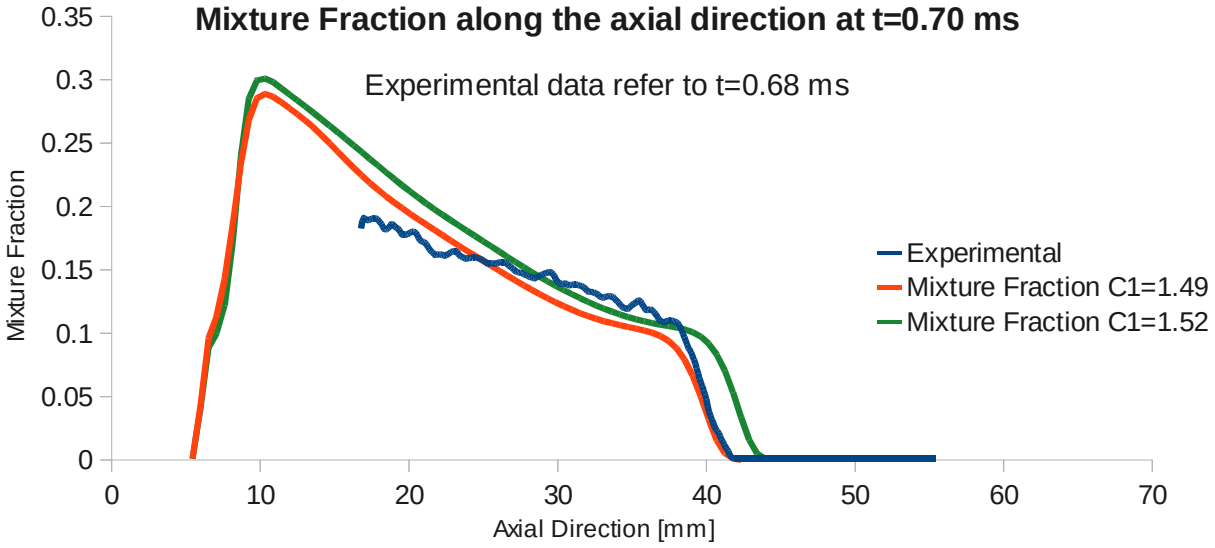

Figure-5.5 [B]

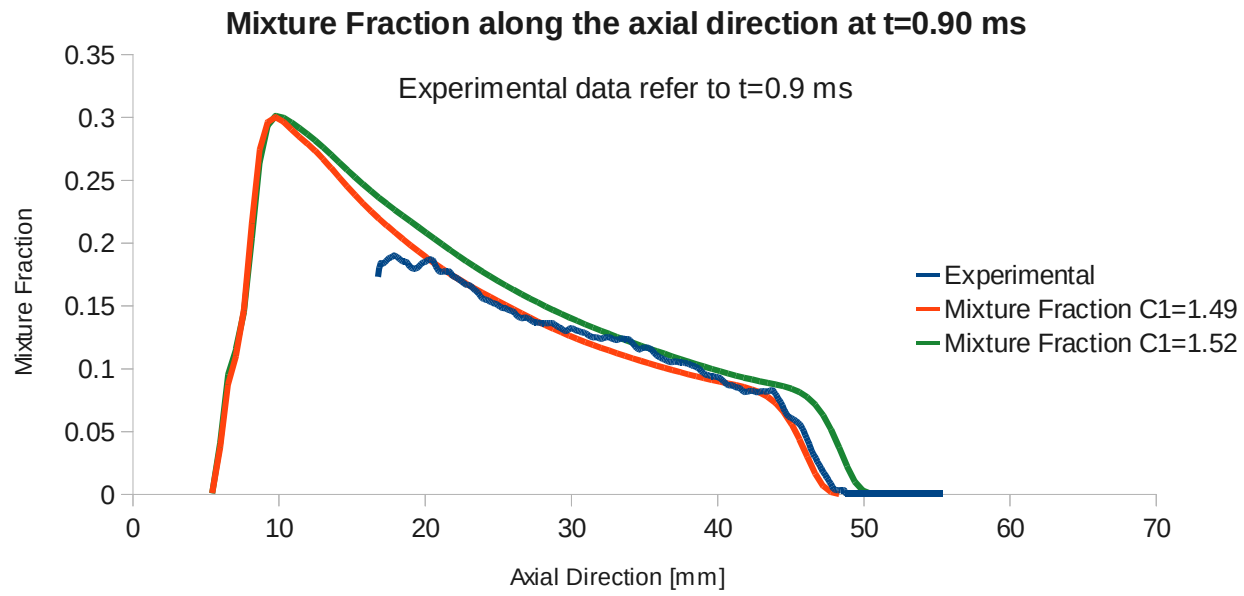

Figure: 5.5 [C]

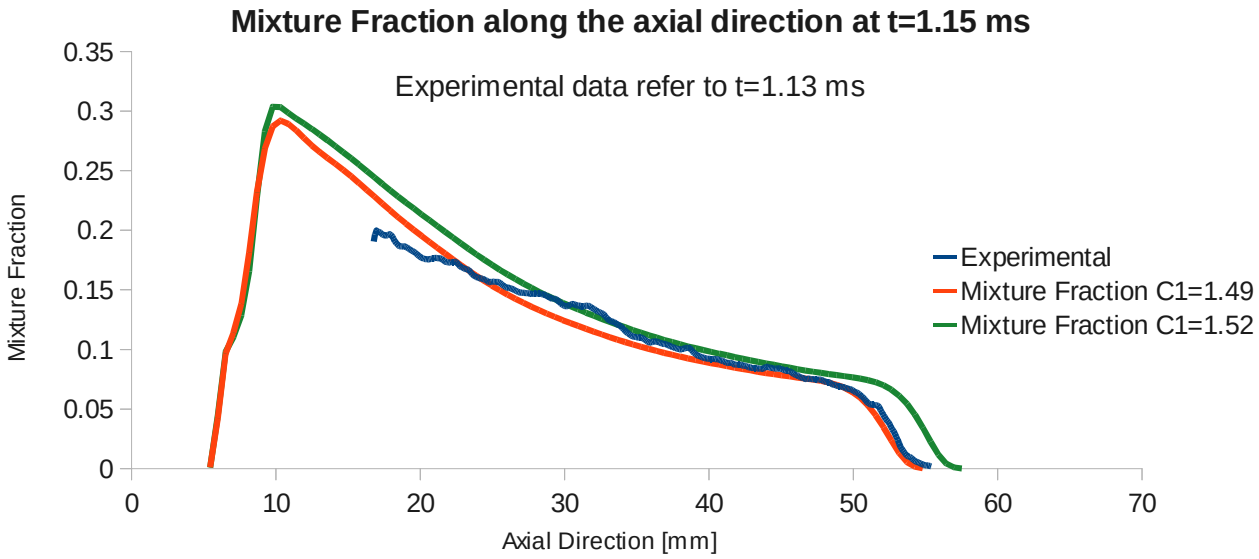

Figure: 5.5 [D]

Figure 5.5: Validation of Mixture Fraction along axial direction in case of both values of C1 for [A] = 0.5 ms, [B] = 0.7 ms, [C] = 0.9 ms, [D] = 1.15 ms

We can conclude a lot of comment on figure 5.5. First, as we obserbed in liquid and vapor penetration data, here also our simulation data is matching with the experimental values. Before the

spray reaches in steady state condition, i.e. when spray is in transient condition the simulated data were slighly deviating compared with fully developed spray (at time t = 1.15 ms). As the time is icreasing the spray becoming steady, and our simulated data were predicting more accuracy in comparison with experimental values.

In the same way we will consider the mixture fraction in radial direction (direction perpendicular to the injector axis) to compare with the experimental data. Figure 5.6 to figure 5.9 will give an idea about the spray mixture fraction in radial direction. Here again we take the simulated and experimental data for 0.5 ms, 0.7 ms, 0.9 ms and 1.15 ms. Data were taken in various axial position like from 20 mm to 50 mm with a 10 mm step from the injector. The results that we got can be illustrated as below:

Considering time t = 0.5 ms:

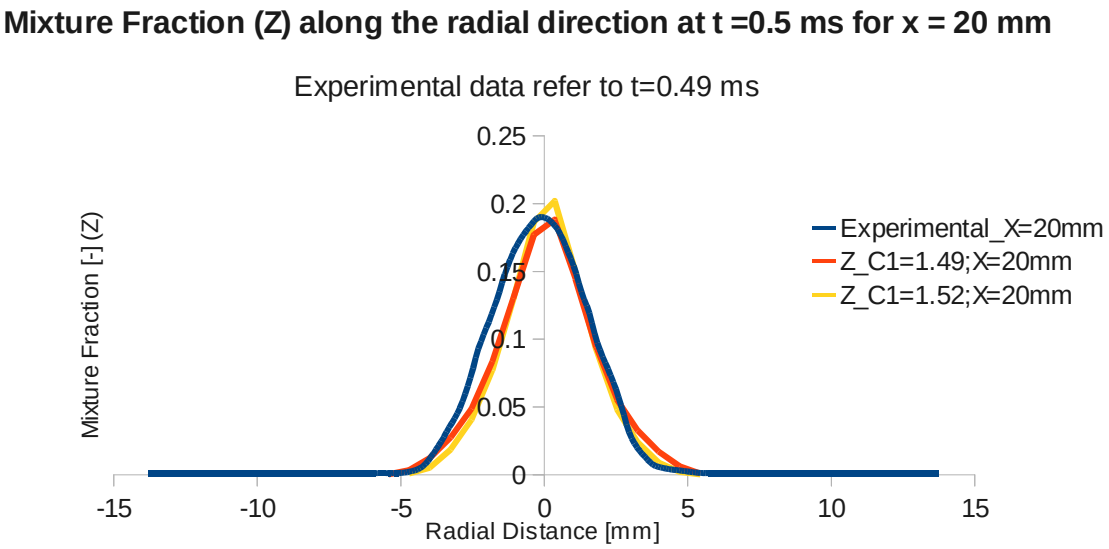

Figure 5.6 [A]

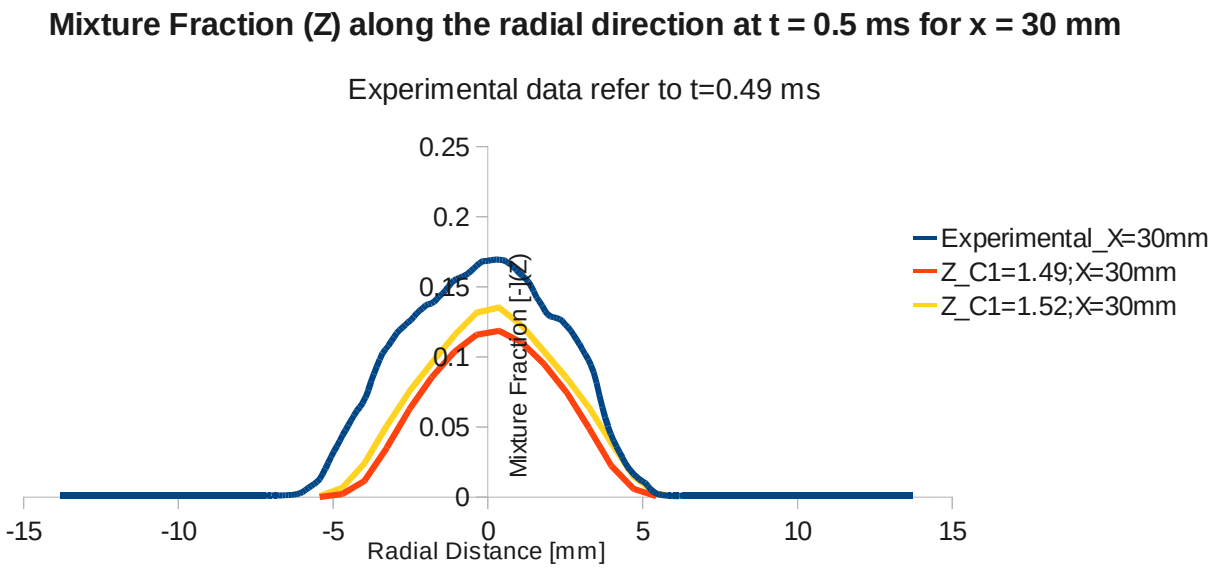

Figure 5.6 [B]

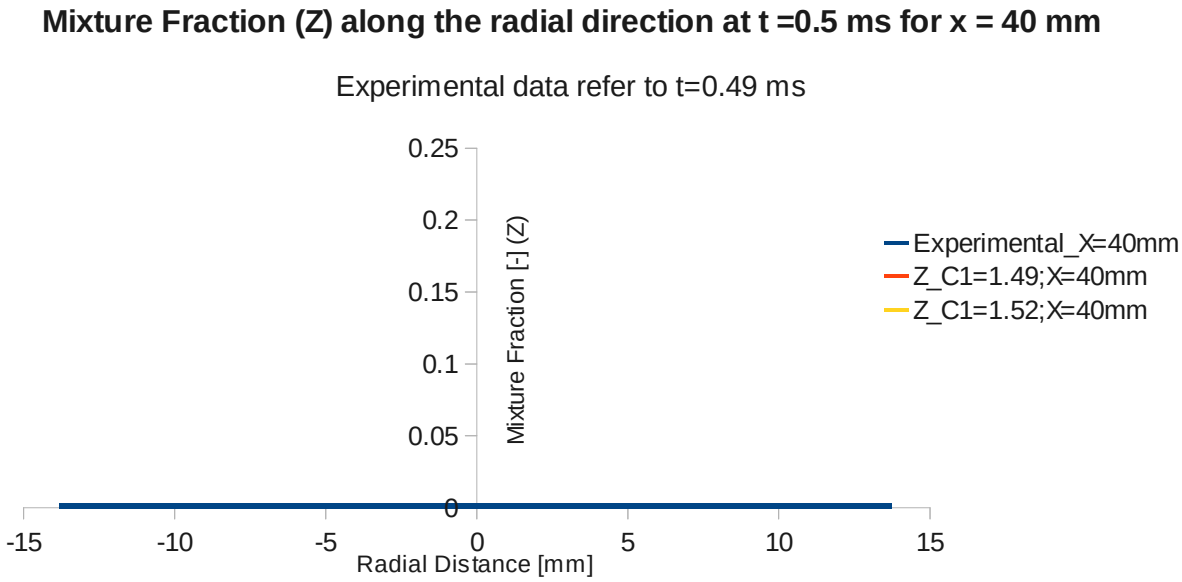

Figure 5.6 [C]

Figure 5.6 : Radial Mass fraction comparison at time t = 0.5 ms for the axial distances of [A] X = 20 mm [B] X = 30 mm [C] X = 40 mm

From Figure 5.6 we can say that at a distance of 20 mm from the injector along the injector direction the radial mixture fraction were comparable with the experimental data. As we go further along the injector axis, we will see that the simulation data is not matching experimental data.

Actually the reason is that in this short time spray is not developed yet. Spray did not get enough time to travel upto distance 40 mm. And in 20 mm distance, our simulated data is not propagated like experimental one for the lacking of time which will be recovered when we will take data for higher values of time (in figure 5.7 to 5.9). From figure 5.6 (B) we can illustrate that taking turbulence model constant, C_1 as 1.52 gives the better prediction with the experimental values.

In the same way for 0.7 milisecond we get the radial mixture fraction data as follows:

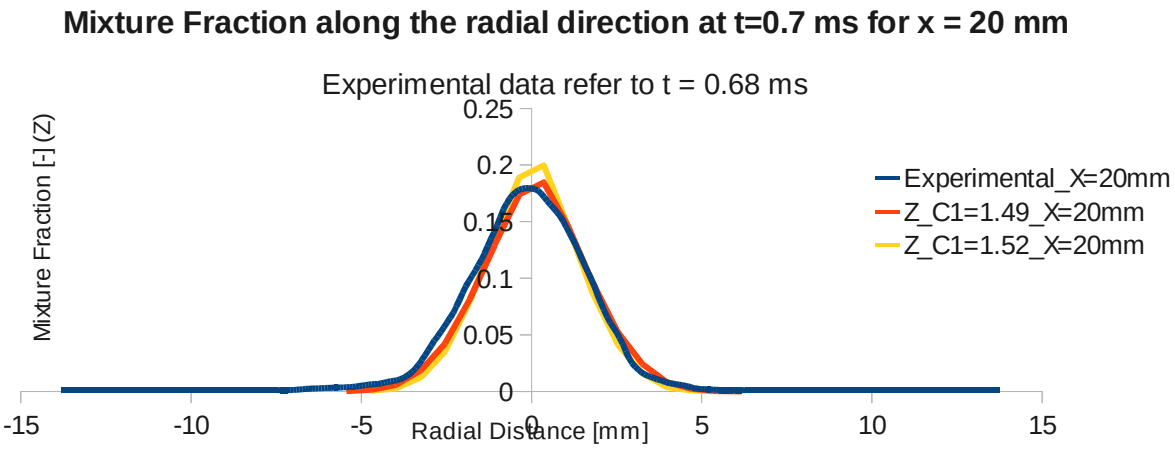

Figure 5.7 [A]

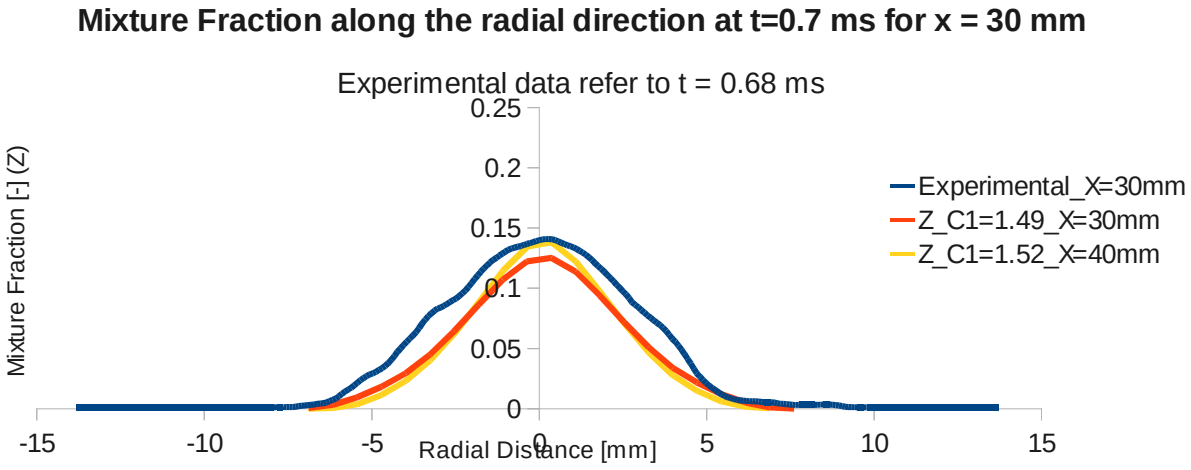

Figure 5.7 [B]

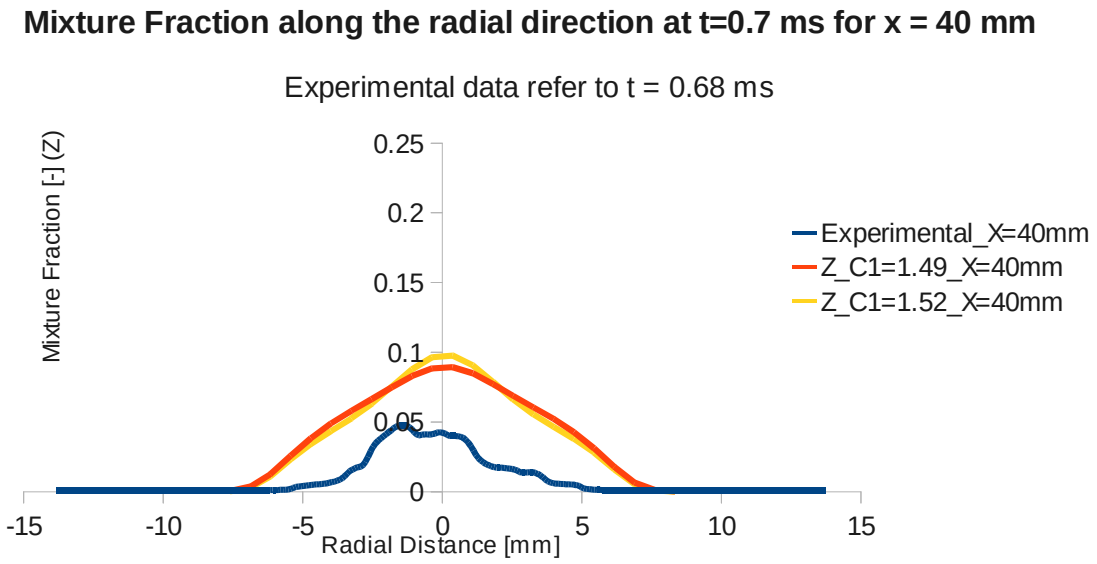

Figure 5.7 [C]

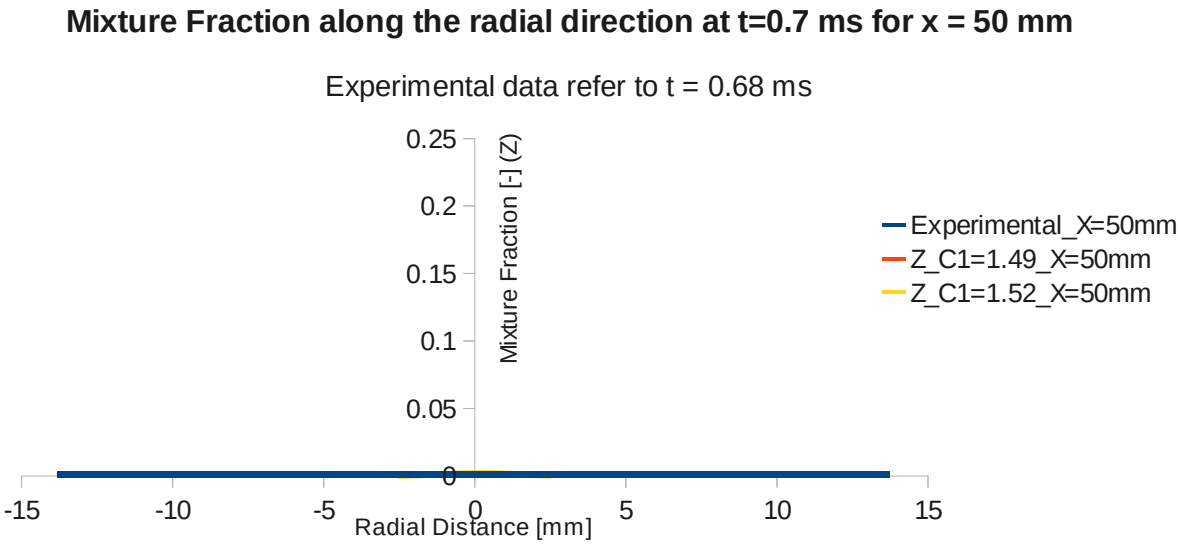

Figure: 5.7 [D]

Figure 5.7: Radial Mass fraction comparison at time t = 0.7 ms for a distance of [A] X = 20 mm [B] X = 30 mm [C] X = 40 mm [D] = 50 mm

If we have a look in figure 5.7, we will find the similarity between the experimental data with simulation one until 30 mm axial distance. Then at 40 mm distance the simulated value get more penitrated than the experimental one. For the case of 50 mm distance i.e. figure 57 (D) we will not see any development of mixture fraction because 0.7 ms is not enough for propagating mixture in

such long distance.

We can consider now the radial mixture fraction data for 0.9 millisecond. The results that we found are shown below:

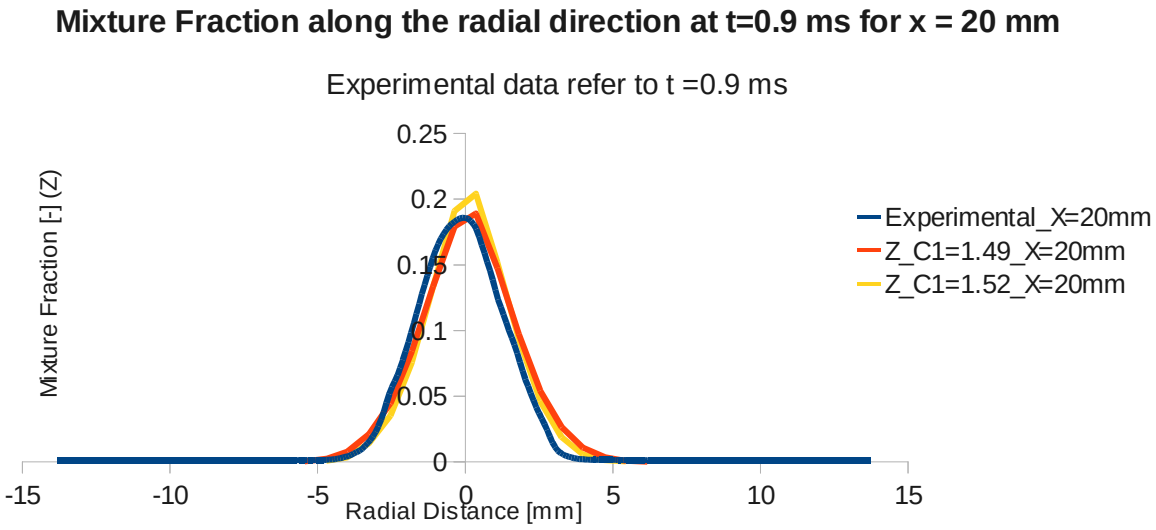

Figure: 5.8 [A]

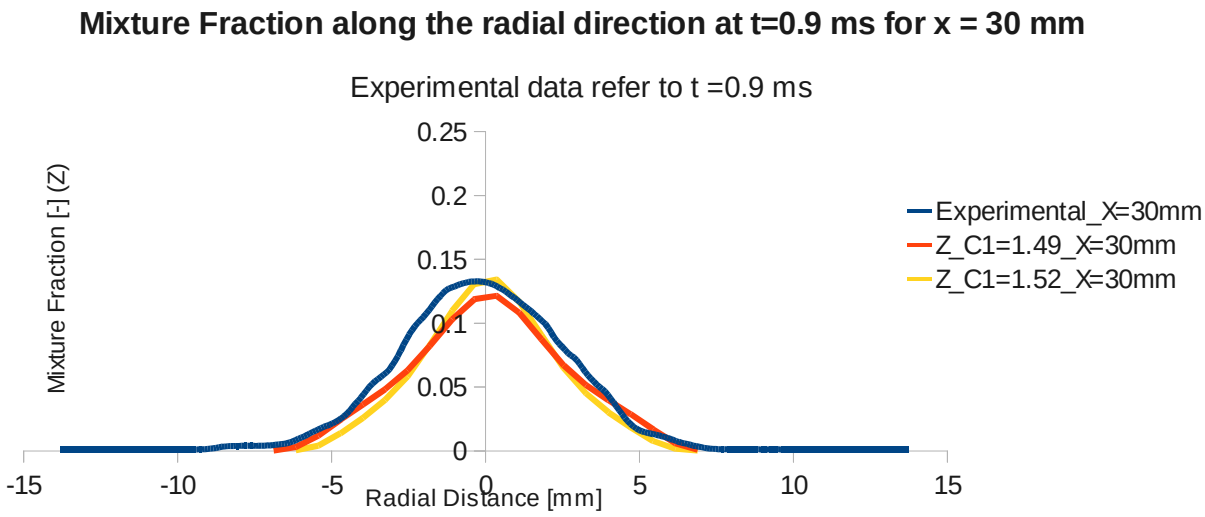

Figure: 5.8 [B]

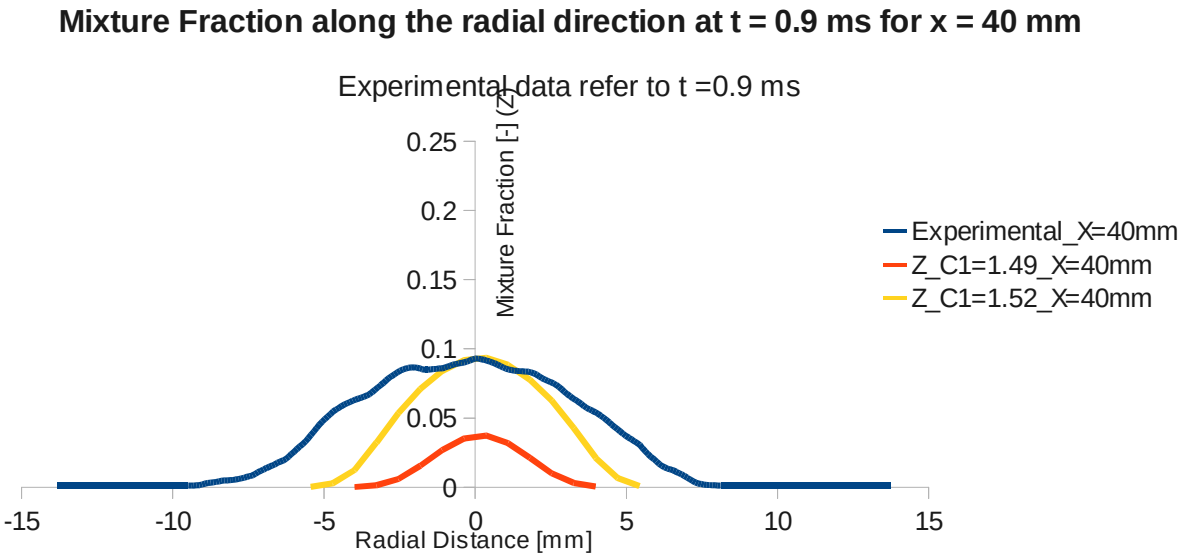

Figure: 5.8 [C]

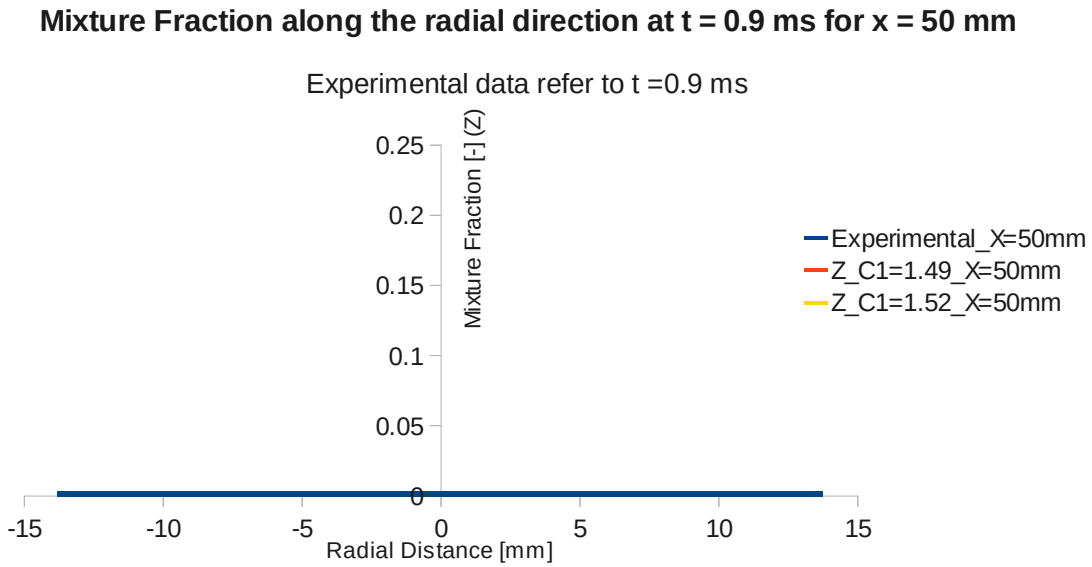

Figure: 5.8 [D]

Figure 5.8 : Radial Mass fraction comparison at time t = 0.9 ms for a distance of [A] X = 20 mm [B] X = 30 mm [C] X = 40 mm [D] = 50 mm

As we found before, same findings can be illustrate here also. For figure 5.8 (C) more turbulence effect is shown is case of C_1 = 1.52. For 50 mm distance we will not see any development of spray in radial direction.

Now let consider the radial mixture fraction data for time 1.15ms. Now the spray is fully in steady

state condition and we can compare the value upto 50 mm distance along the axial direction. The corresponding figures are shown here:

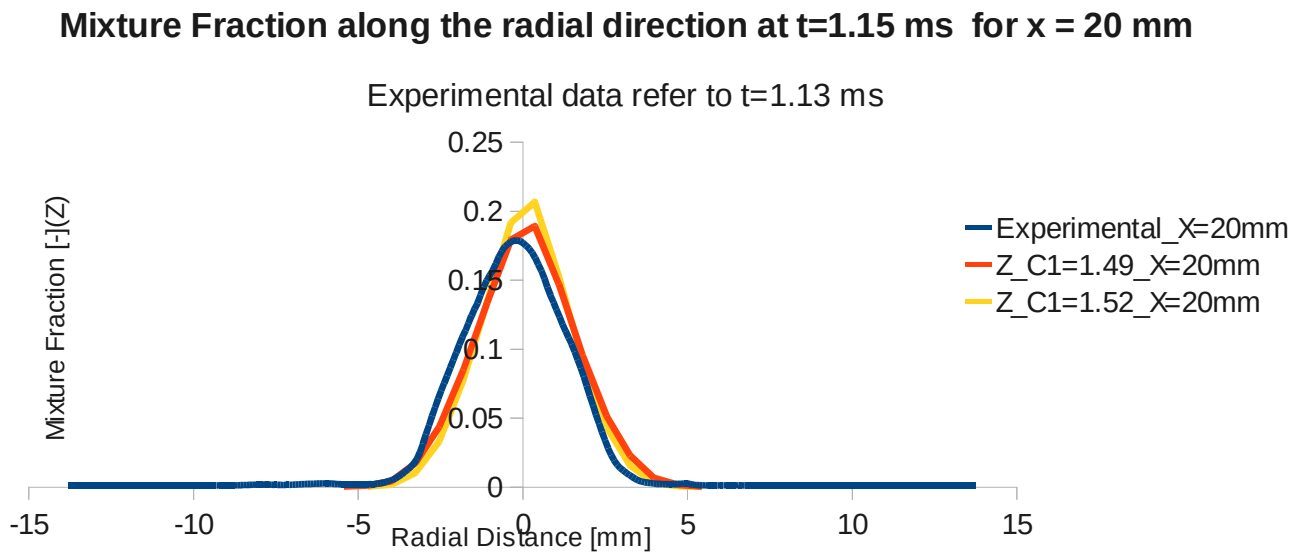

Figure: 5.9 [A]

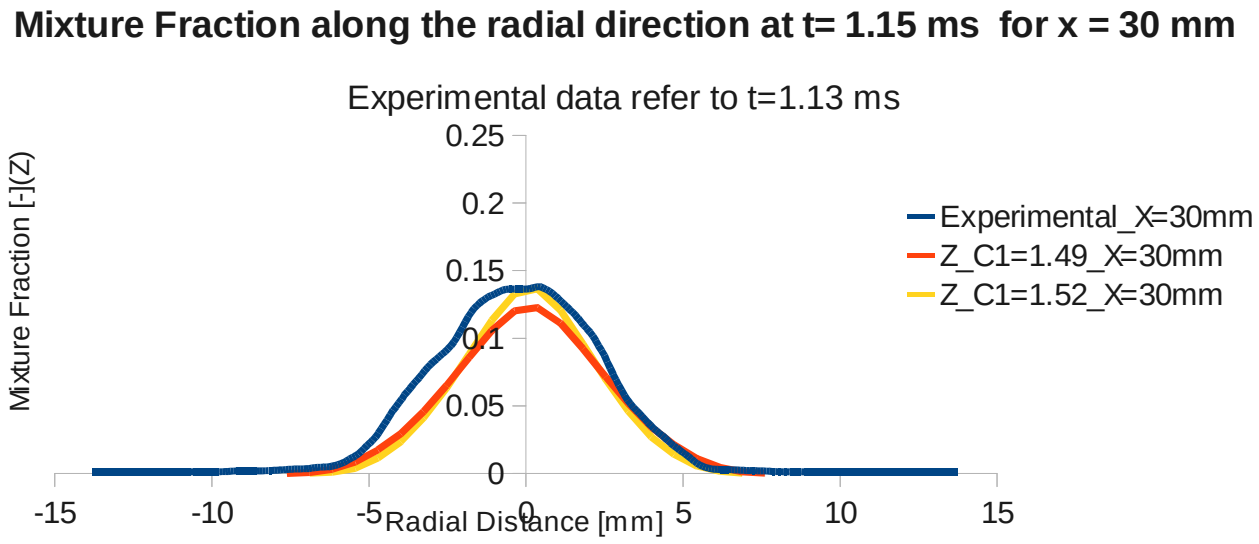

Figure: 5.9 [B]

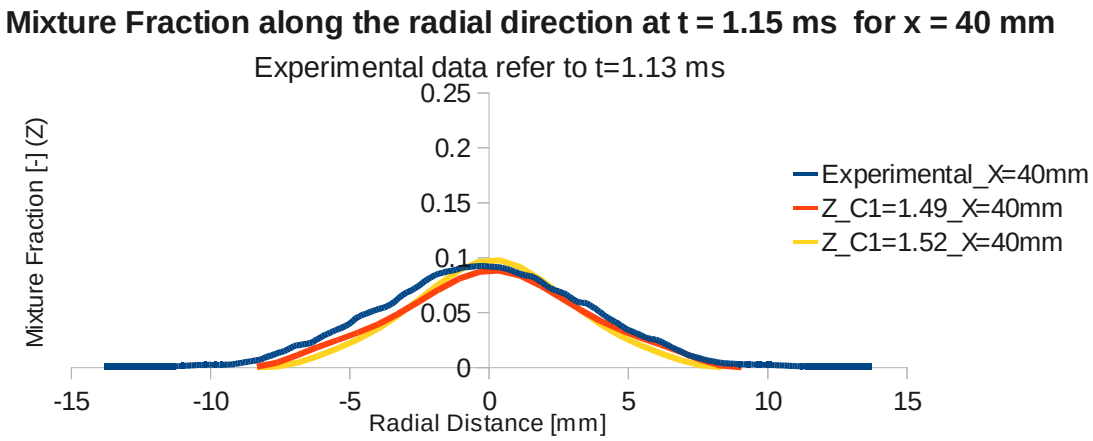

Figure: 5.9 [C]

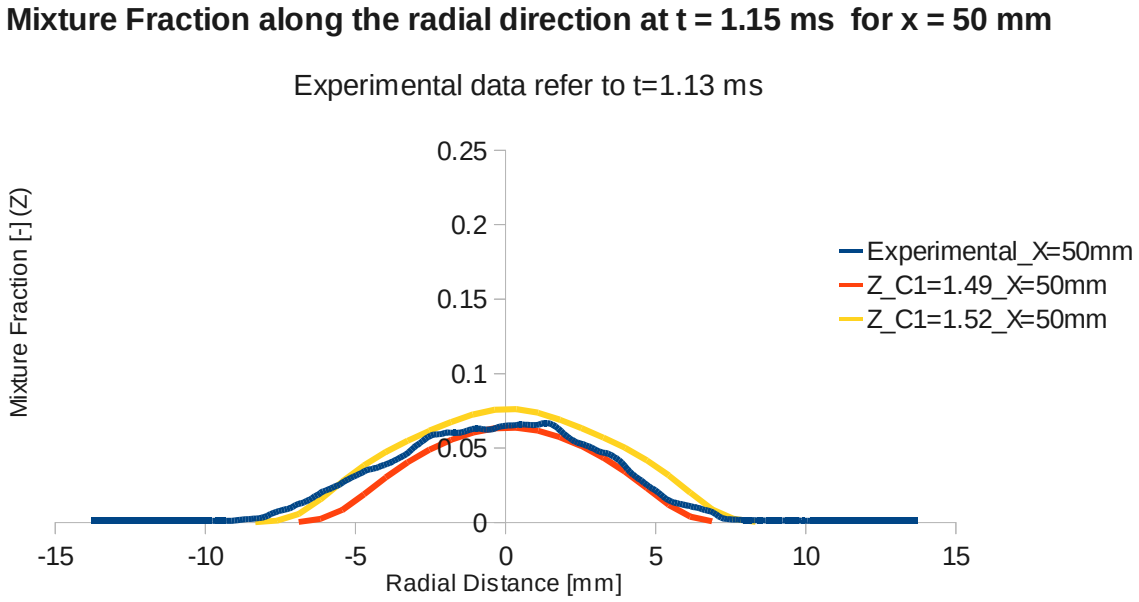

Figure: 5.9 [D]

Figure 5.9 : Radial Mass fraction comparison at time t = 1.15 ms for a distance of [A] X = 20 mm [B] X = 30 mm [C] X = 40 mm [D] = 50 mm

From figure 5.9 we can see, the mixture fraction for a steady spray in the radial direction. Along almost all the cases the simulated mixture fraction data with C_1=1.52 gives good matching with our available experimental data.

From the figure below, we may have an idea about the Spray and Vapor propagation through the combustion chamber

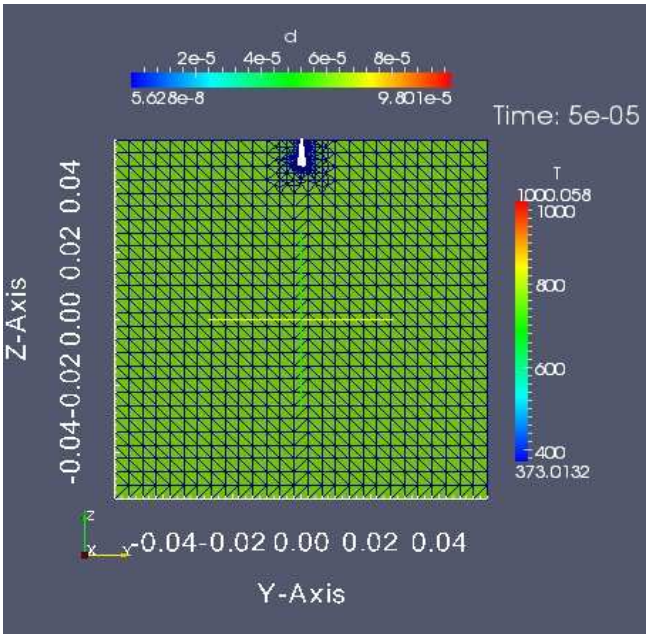

Figure-5.10 [A]

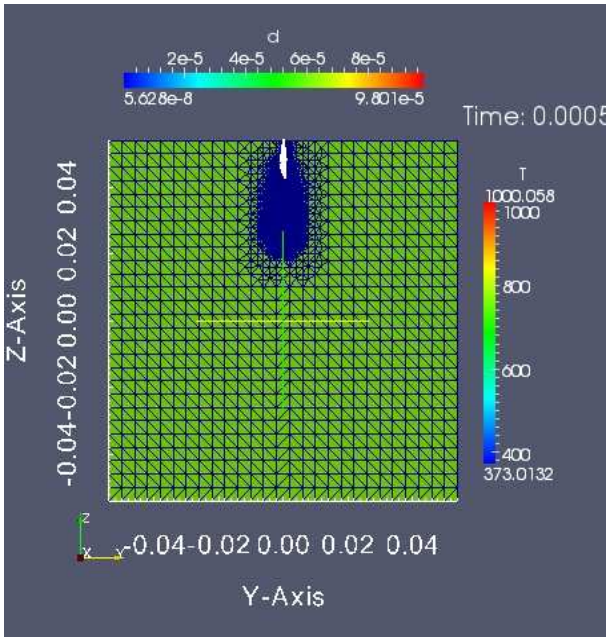

Figure- 5.10 [B]

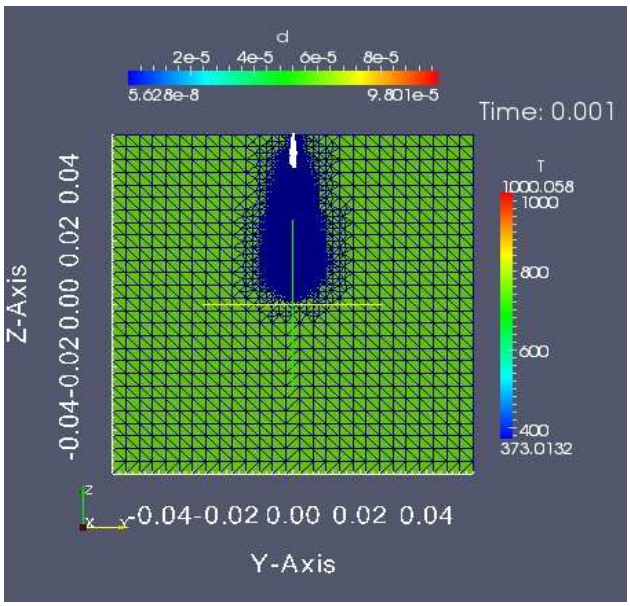

Figure-5.10 [C]

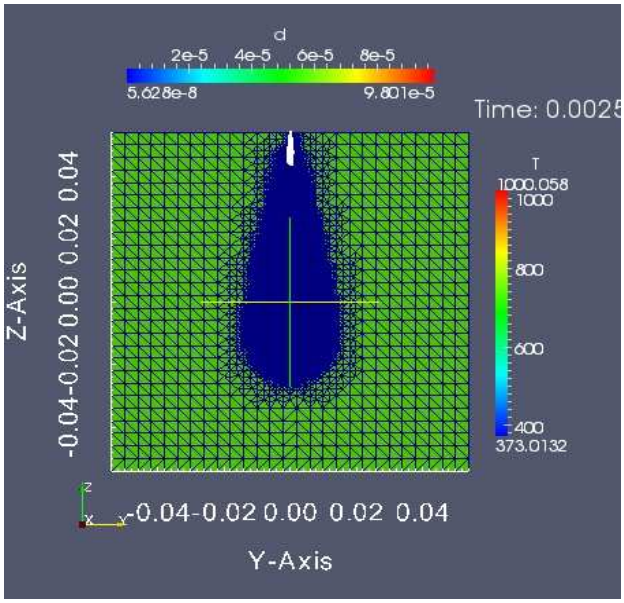

Figure- 5.10 [D]

Figure-5.10: Spray and Vapor Propagation inside the Cylinder using KHRT model (with model constant, C1 = 1.49) and blob injector for time, [A] t = 5e-5 sec, [B] t = 0.0005 sec, [C] t = 0.001 sec, [D] t = 0.0025 sec. This figure shows the change in the droplet diameter (in mm) and temperature (in K) of the particles throughout the propagation. (Fuel used = N-Heptane).

And the detailed view can be found in the following pictures:

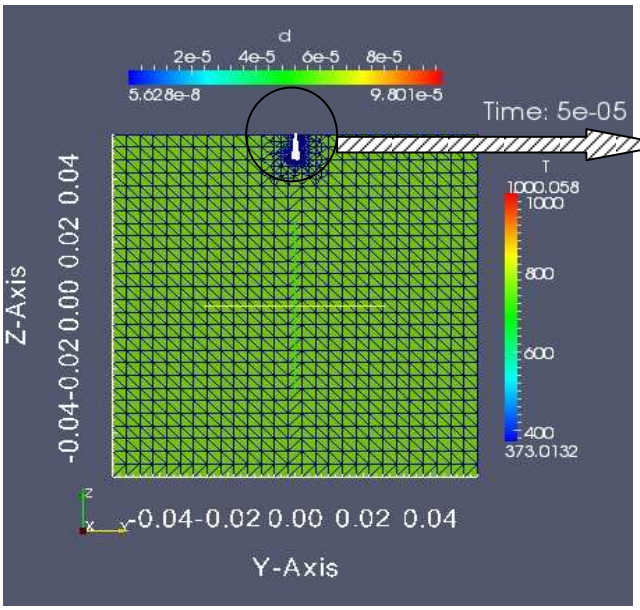

Figure-5.11[A]

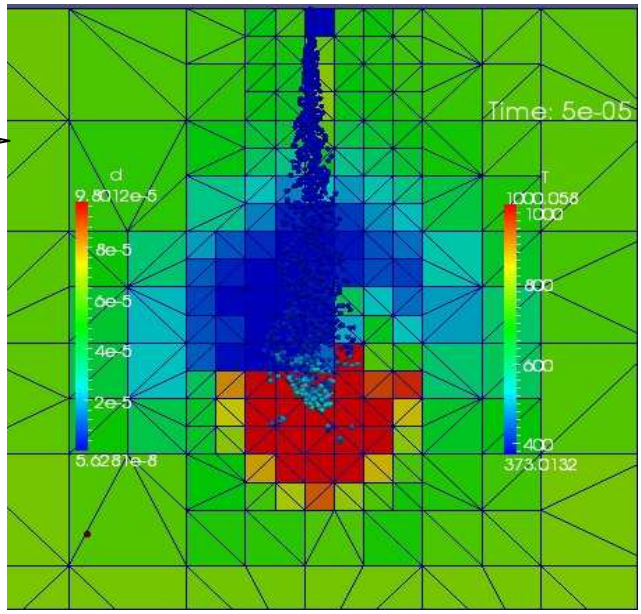

Figure-5.11 [B]

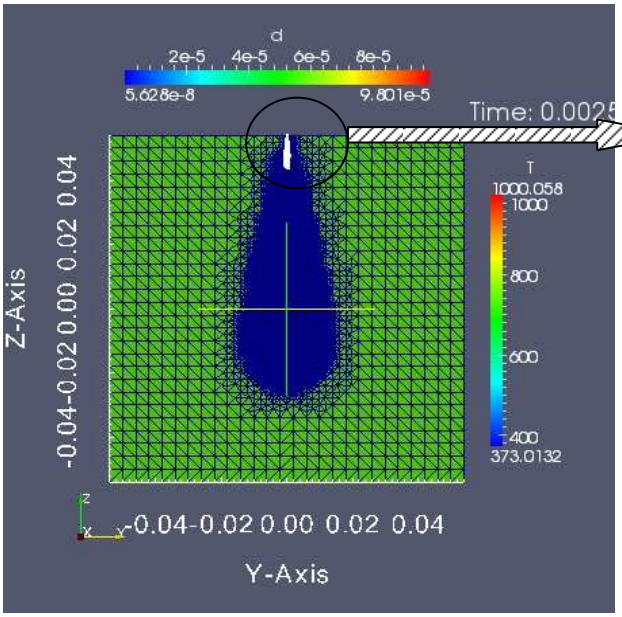

Figure-5.11[C]

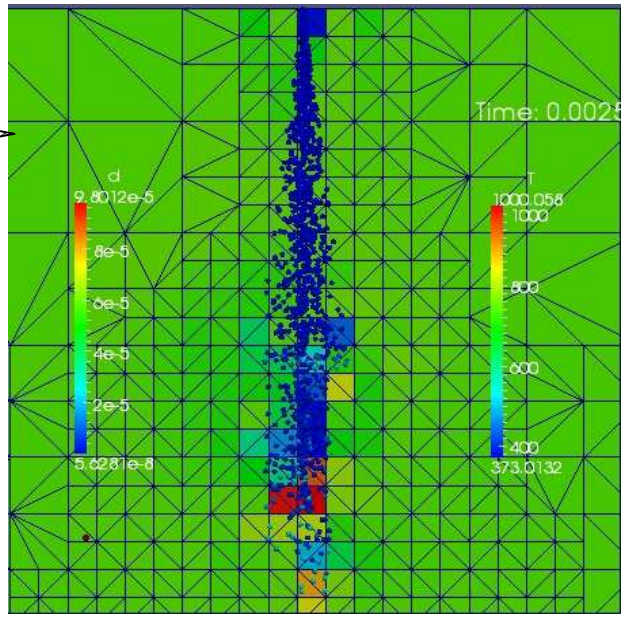

Figure-5.11 [D]

Figure-5.11: Deatil zoomed view of spray and nature of propagation using KHRT model (with model constant, C1 = 1.49) and blob injector for time, [A] & [B] t = 5e-5 sec, [C] & [D] t = 0.0025 sec. [B] and [D] are the zoomed view of spray corresponding to figure [A] and [C].

Considering C1 as 1.52 the simulated scenario can be illustrated as below:

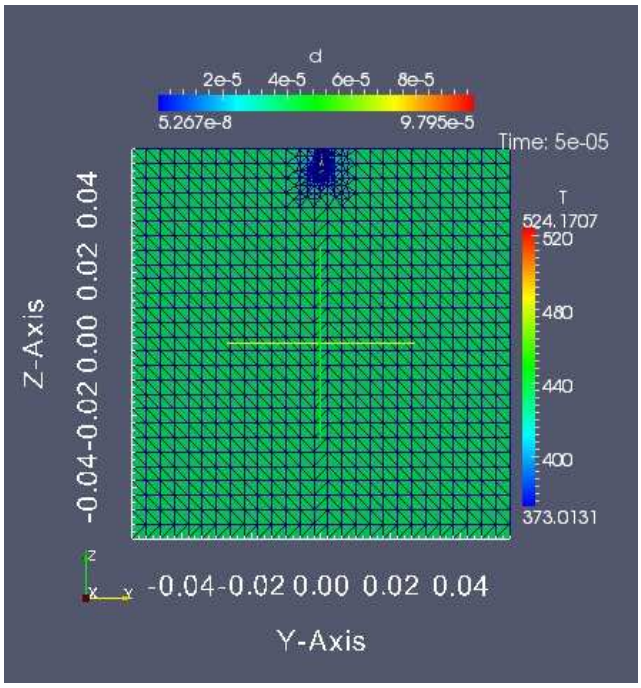

Figure-5.12 [A]

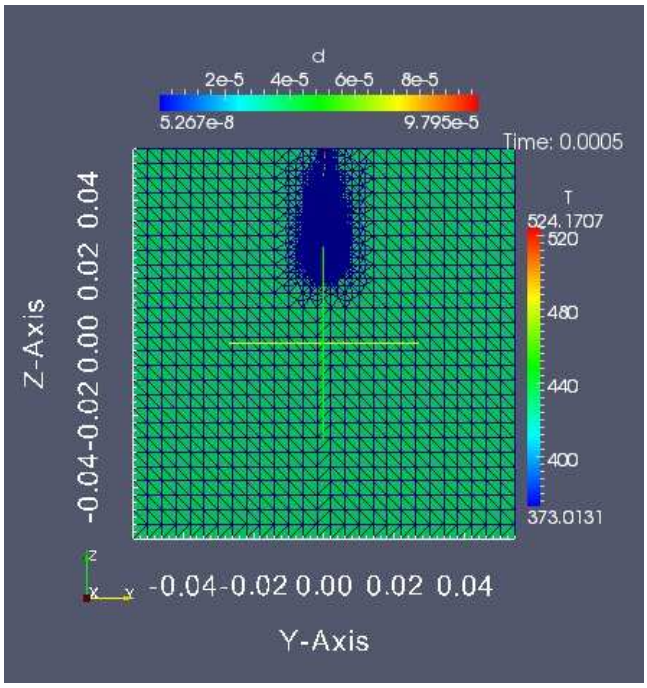

Figure- 5.12 [B]

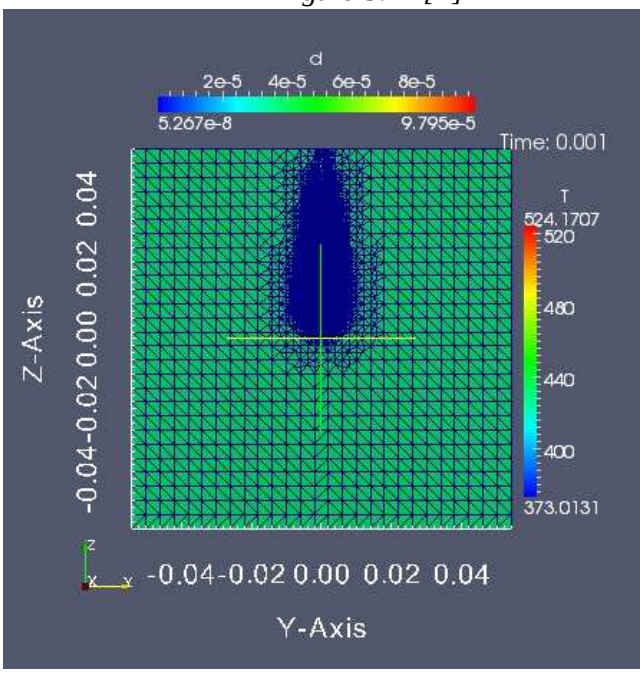

Figure-5.12 [C]

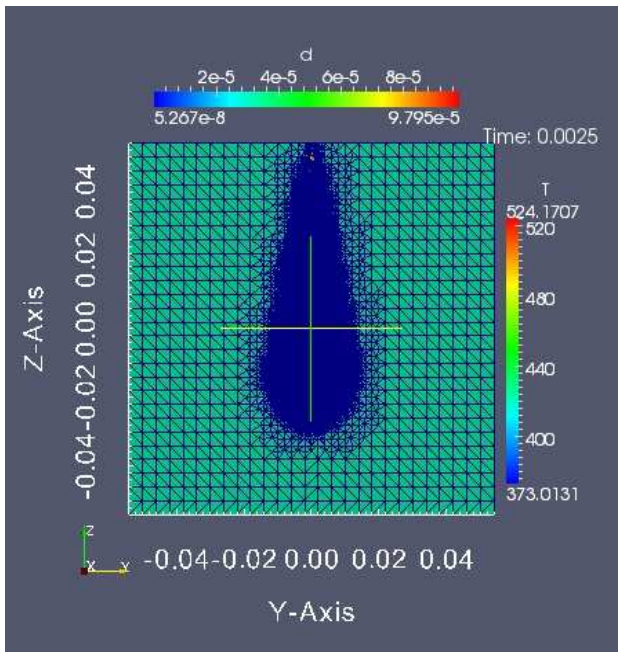

Figure- 5.12 [D]

Figure-5.12: Spray and Vapor Propagation inside the Cylinder using KHRT model (with model constant, C1 = 1.52) and blob injector for time, [A] t = 5e-5 sec, [B] t = 0.0005 sec, [C] t = 0.001 sec, [D] t = 0.0025 sec. This figure shows the change in the droplet diameter (in mm) and temperature (in K) of the particles throughout the propagation. (Fuel used = N-Heptane).

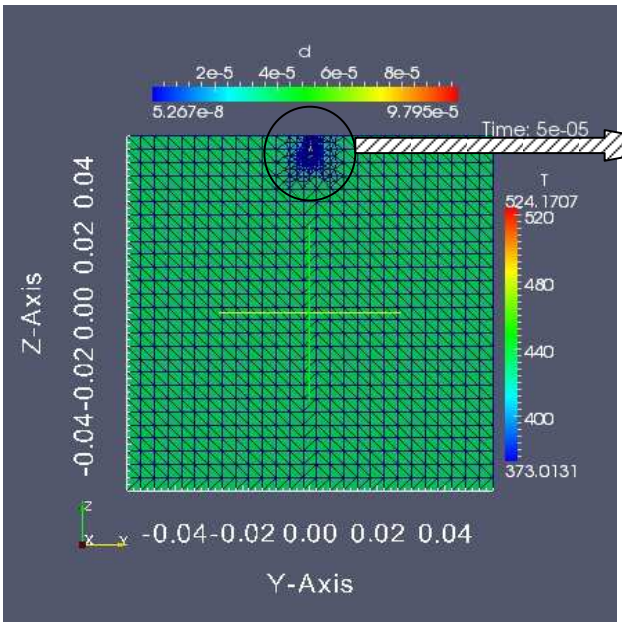

Figure-5.13[A]

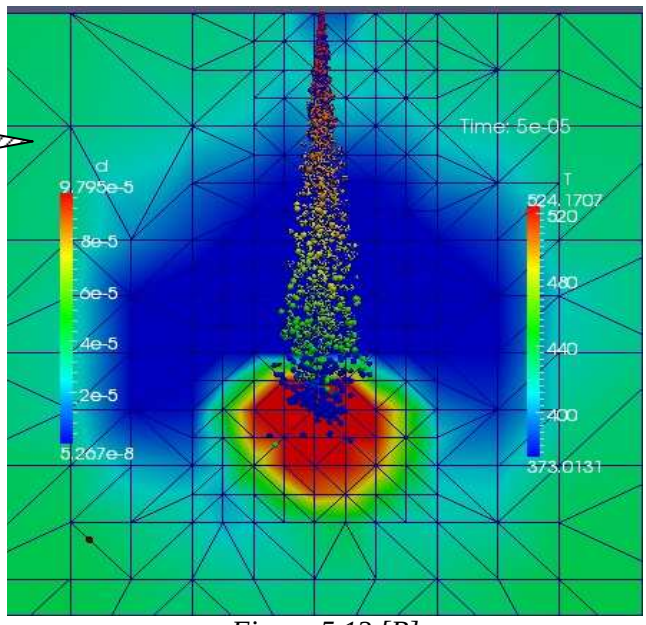

Figure-5.13 [B]

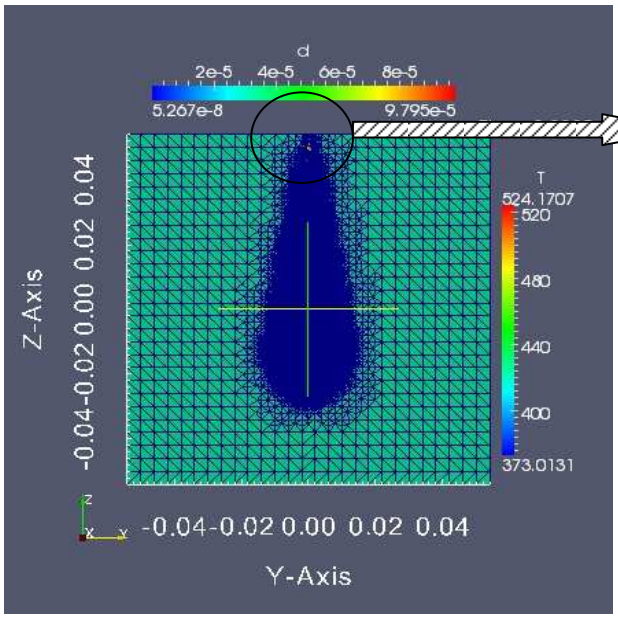

Figure-5.13[C]

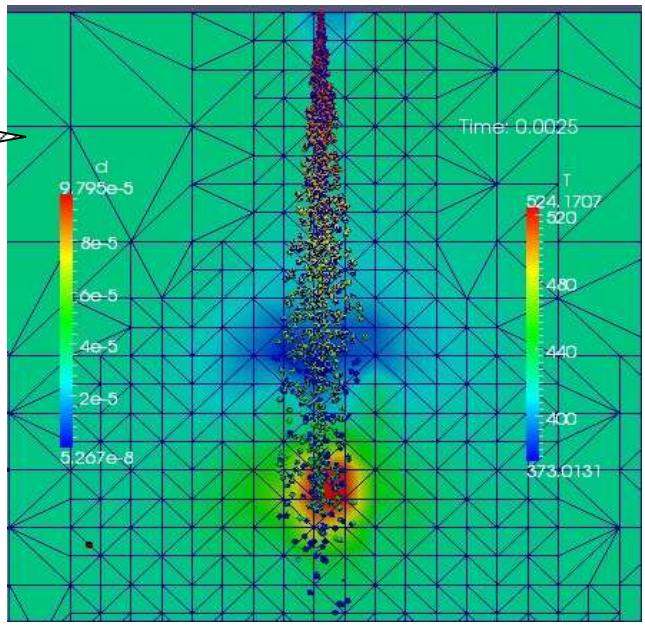

Figure-5.13[D]

Figure-5.13: Detail zoomed view of spray and nature of propagation using KHRT model (with model constant, C1 = 1.52) and blob injector for time, [A] & [B] t = 5e-5 sec, [C] & [D] t = 0.0025 sec. [B] and [D] are the zoomed view of spray corresponding to figure [A] and [C].

From figure 5.13 [B] and figure 5.13 [D] we can get a clear idea about KHRT breakup model. The blue particles are just about to disappear in the next stage. And the particles with some portion

covered with blue color are showing that, these blue parts are almost about to going in disappear condition.

Thus, by KHRT Blob model in this case we validate our model not only in terms of spray and vapor penetrations, but also considering mass fraction data in both axial and radial directions. The simulation data and spray pattern gives us a clear idea about the KHRT breakup model.

Same simulation and comparison was done for KHRT model but this time using Huh Injector istead of Blob injector. All the data were compared like before and here also we get the good matching of our model corresponding with the experimental data. In this section we will discuss further more for one case in transient condition i.e. when spray is not fully developed and one condition for steady state spray.

5.1.1.1.2 Using Huh Injector

We found the spray penetration data as follows:

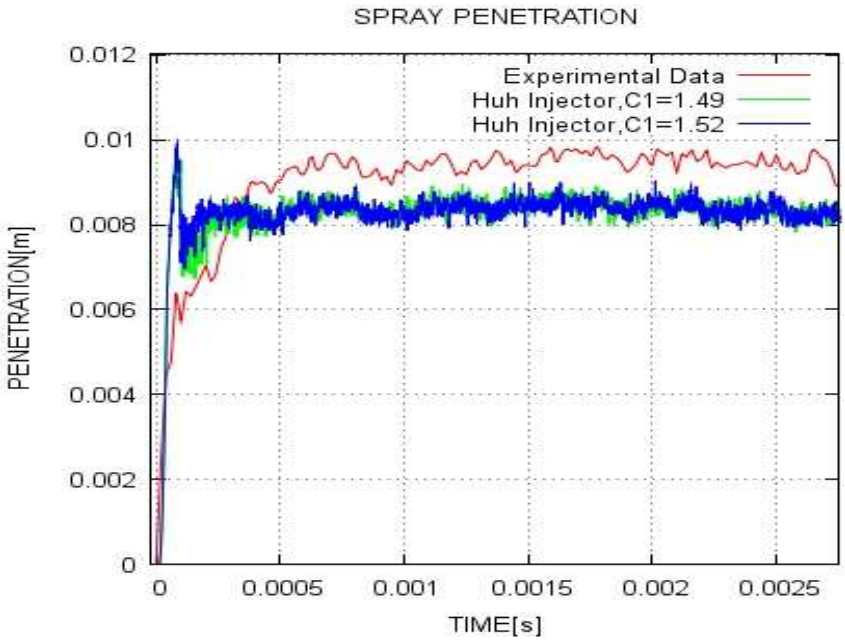

Figure 5.14: Comparison of Spray penetration comparing with experimental data (ECN Sandia [49]) and simulated data for Huh injector model with two different values of constant C1 of k–ϵ turbulence model.

Accordign to the figure 5.14 we can comment that, very initially we can see a peak in the simulated spray penetration data but after that it was all steady. These results were not exactly like

what we found in blob injector cases. Due to change of the injector our spray is now penetrating less distance than the experimental one and also if we compare with the data where blob injector was used. Here, for spray penetration, Turbulence model constant C_1 do not have any great effect. In the same way if we look to the vapor penetration data we will like below:

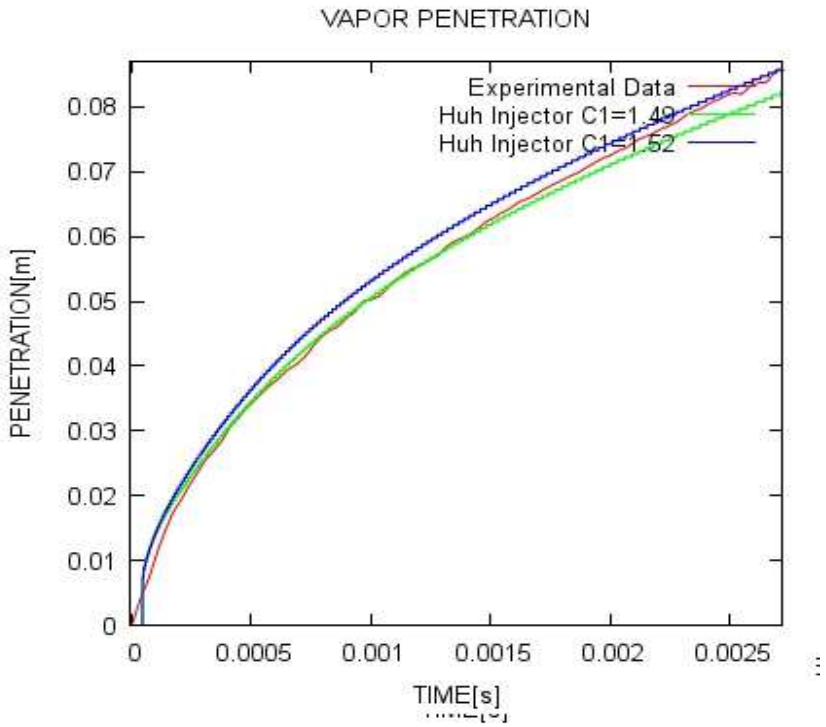

Figure 5.15 : Comparison of vapor penetration comparing with experimental data (ECN Sandia [49]) and simulated data for Huh injector model with two different values of constant C1 of k–ϵ model.

For the case of C_1 = 1.52, in figure 5.15 we can see the penetration profile is matching more with the experimental value. We can see the turbulence affect here for vapor penetration.

For discussing axial mixture fraction data lets take data for time t = 0.5 ms (transient condition) and t = 1.15 ms (steady spray condition). We will see form the following figure 5.16 that, at steady sondition simulation data giving good matching.

At time, t = 0.5 ms:

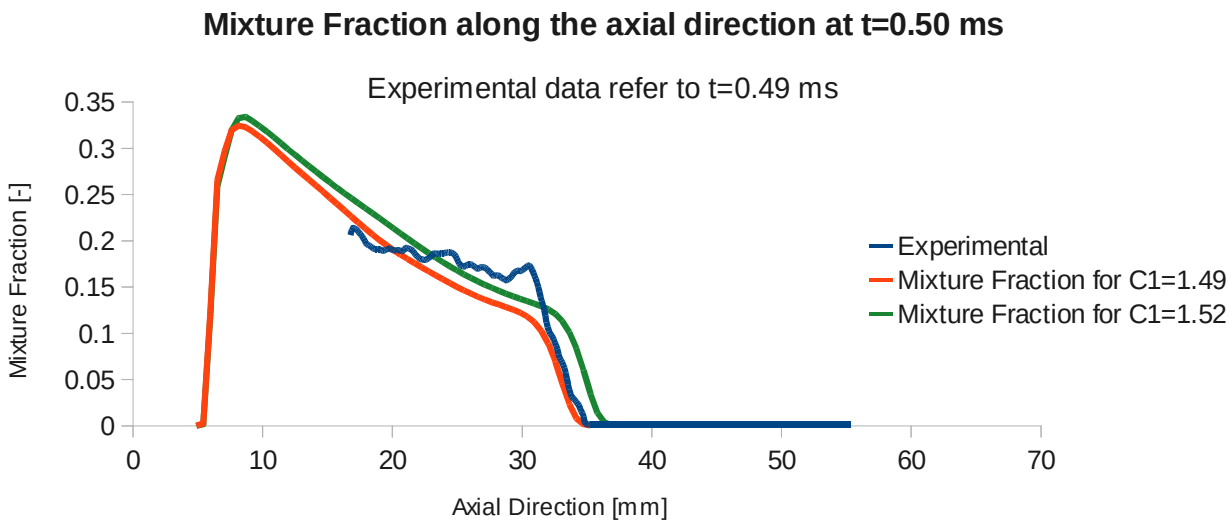

Figure :5.16 [A]

At time, t = 1.15 ms :

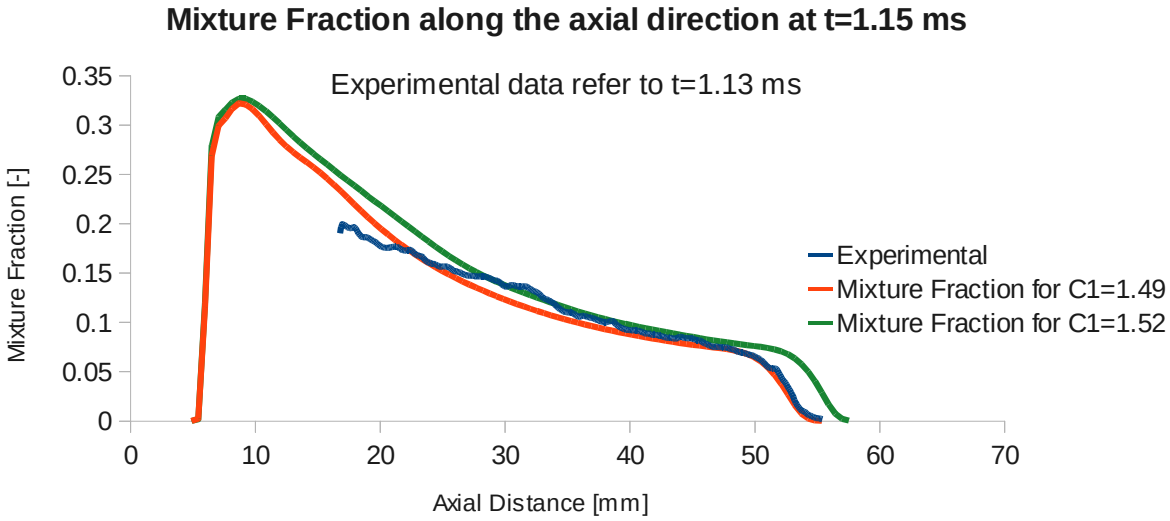

Figure 5.16 [B]

Figure 5.16: Validation of Mixture Fraction along axial direction in case of both values of C1 for [A] = 0.5 ms, [B] = 1.15 ms

Considering radial mixture fraction we can illustrate following situations

At time, t = 0.7 ms

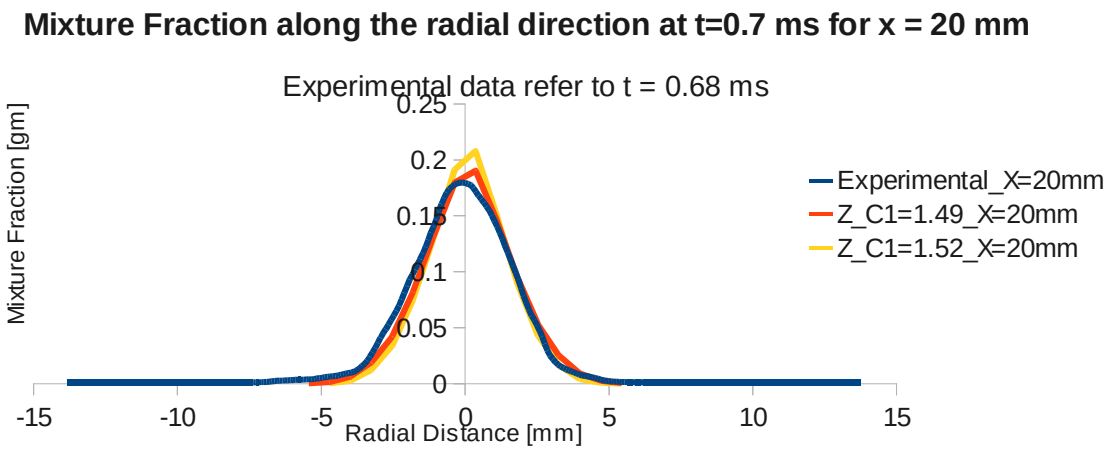

Figure : 5.17[A]

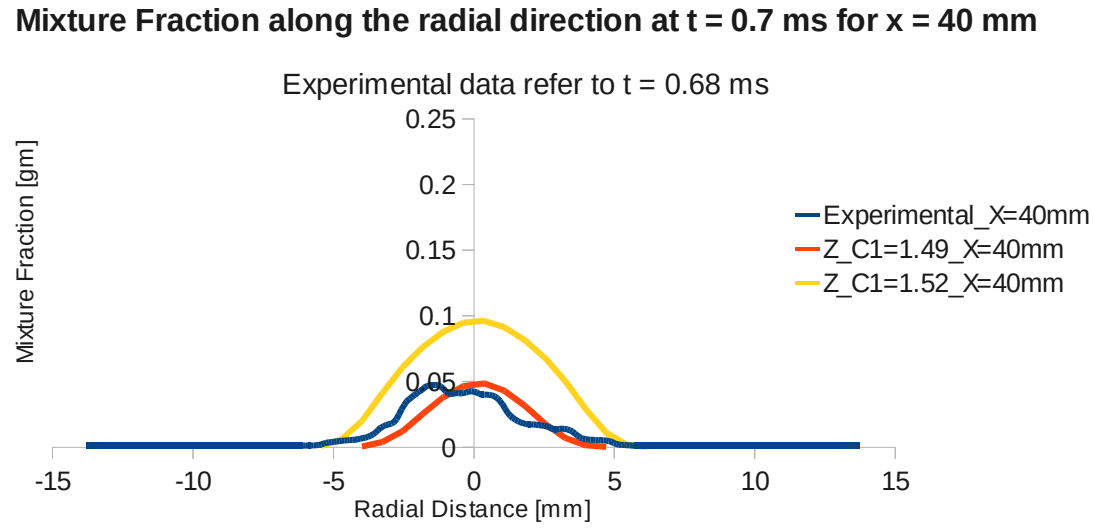

Figure : 5.17[B]

Figure : 5.17: Radial Mass fraction comparison at time t = 0.5 ms for a distance of [A] X = 20 mm [B] X = 40 mm

If we have a look on figure 5.17 (B) we can see the simulated data propagates much more with respect to experimental data. This difference is only due to the fact that in actual case fuel in this short period (0.7 millisecond) did not get enough time to propagate along radial direction. If we consider the steady spray (time t = 1.15 millisecond), then we will not observe this condition because there the spray get enough time to propagate in radial direction (Figure 5.18)

Mixture fraction in radial direction for steady spray:

At time, t = 1.15 ms

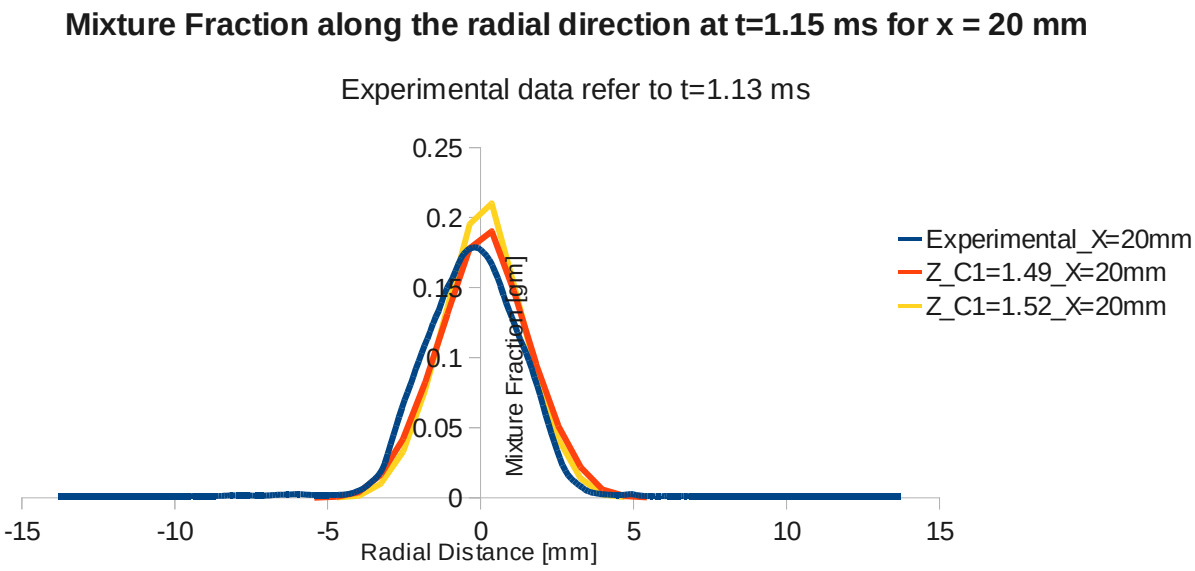

Figure: 5.18[A]

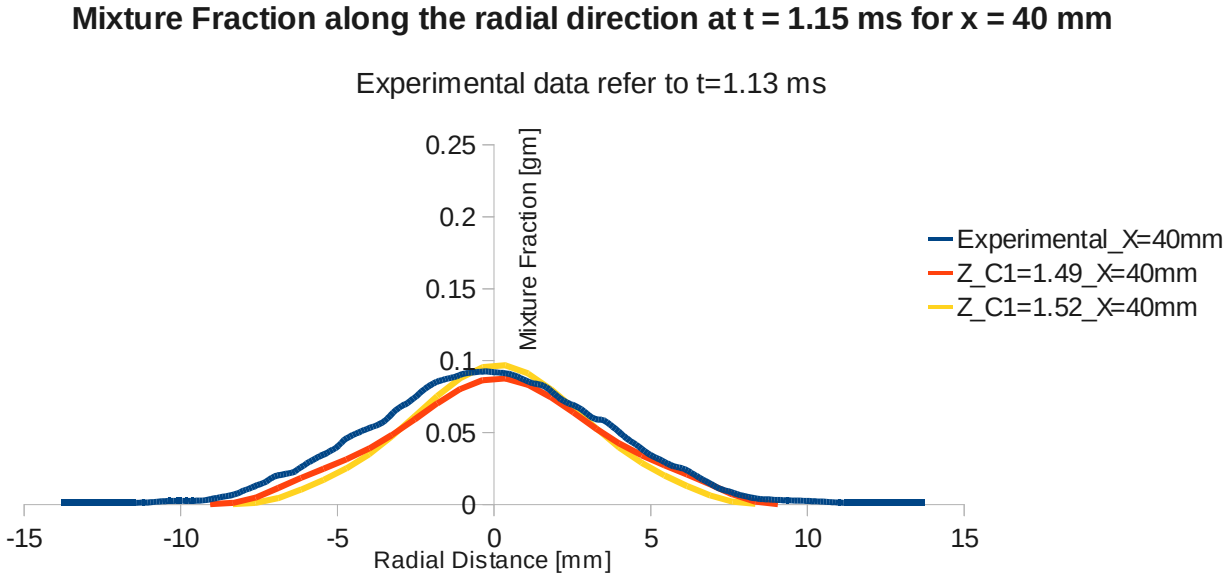

Figure : 5.18[B]

Figure : 5.18: Radial Mass fraction comparison at time t =1.15 ms for a distance of [A] X = 20 mm, [B] X = 40 mm.

The Spray and Vapor Propagation in the Combustion Chamber can be expressed throuth below simulated pictures (Considering Turbulence Constant C1 = 1.49):

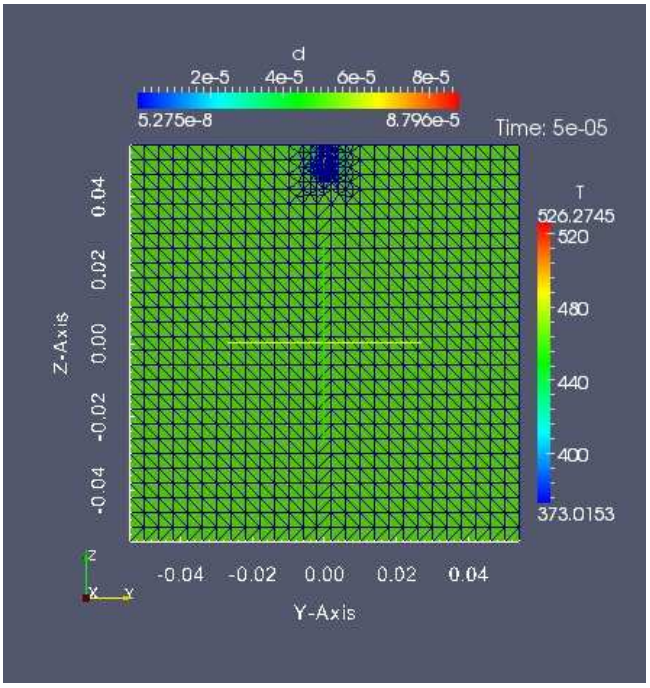

Figure- 5.19 [A]

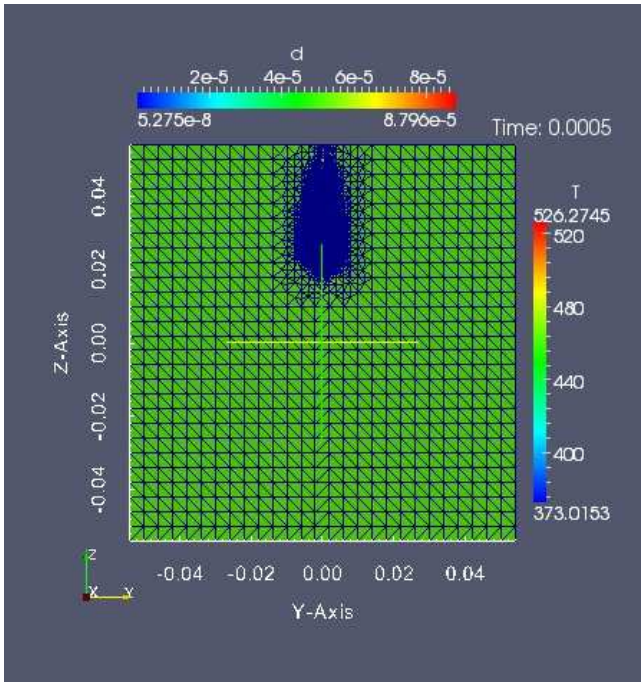

Figure- 5.19 [B]

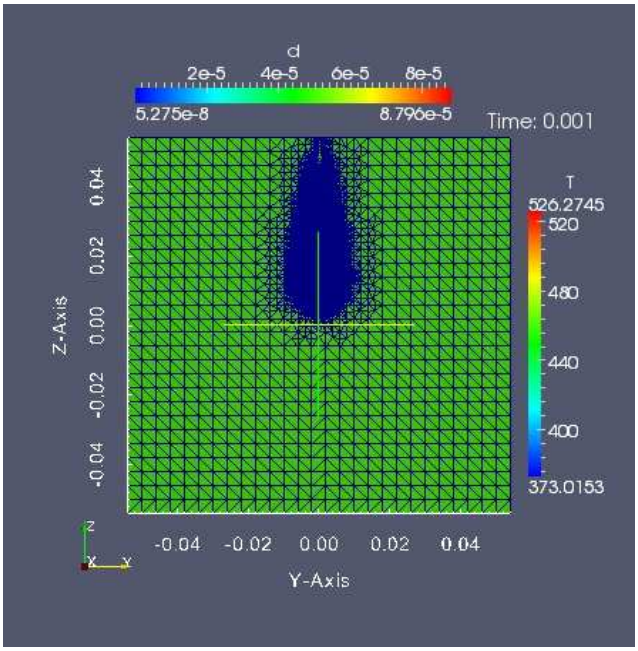

Figure-5.19 [C]

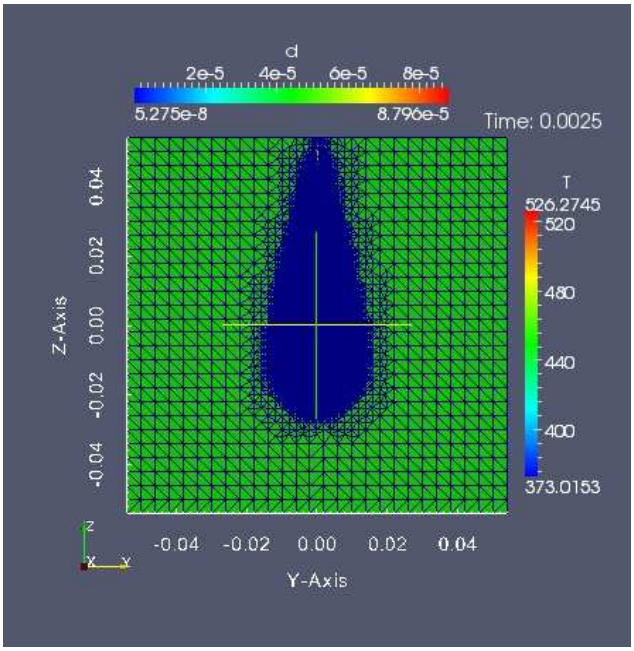

Figure- 5.19 [D]

Figure-5.19: Spray and Vapor Propagation inside the Cylinder using KHRT model (with model constant, C1 = 1.49) and Huh injector for time, [A] t = 5e-5 sec, [B] t = 0.0005 sec, [C] t = 0.001 sec, [D] t = 0.0025 sec. This figure shows the change in the droplet diameter (in mm) and temperature (in K) of the particles throughout the propagation. (Fuel used = N-Heptane).

And with the Zoomed view we can explain the situation like below (For C1 = 1.49):

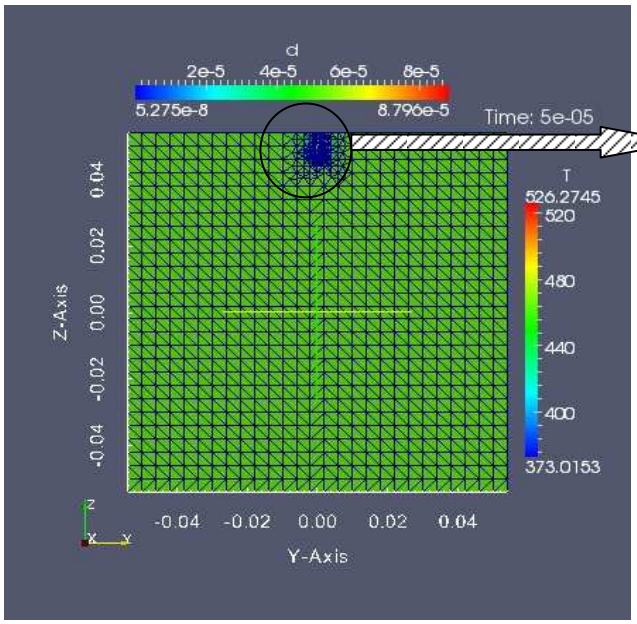

Figure-5.20 [A]

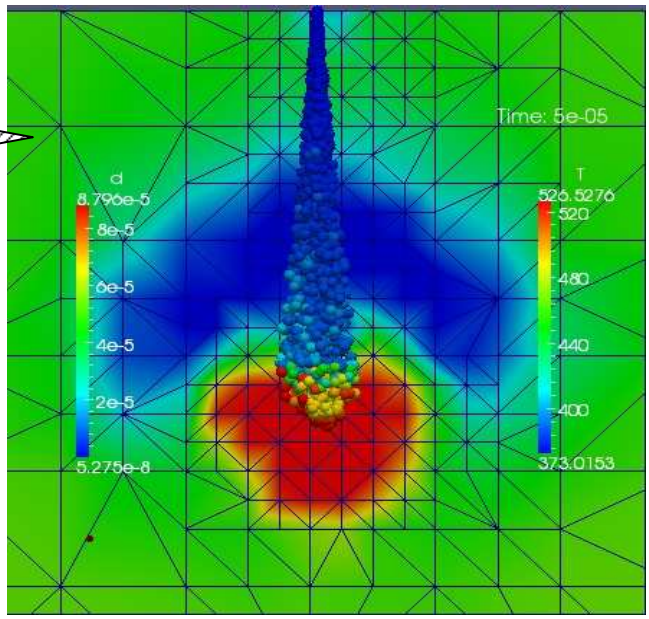

Figure-5.20[B]

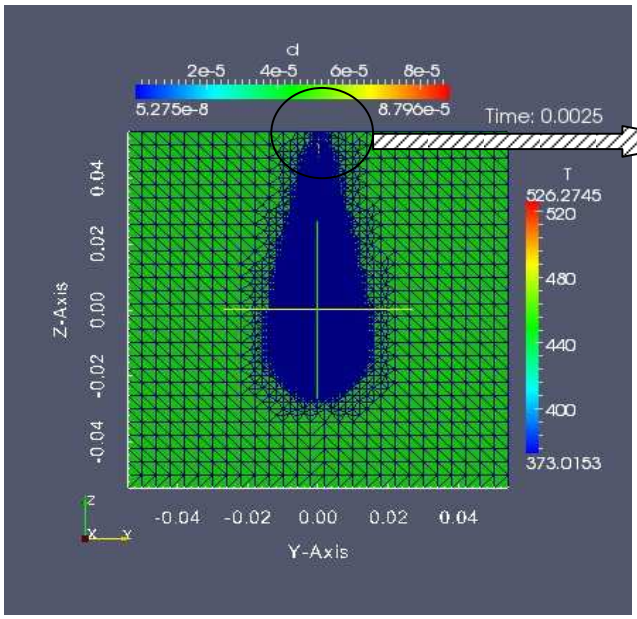

Figure-5.20[C]

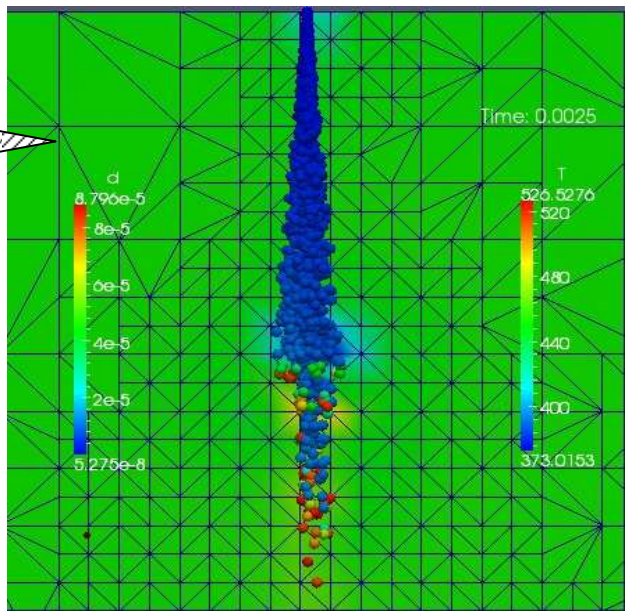

Figure- 5.20 [D]

Figure-5.20: Detail zoomed view of spray and nature of propagation using KHRT model (with model constant, C1 = 1.49) and Huh injector for time, [A] & [B] t = 5e-5 sec, [C] & [D] t = 0.0025 sec. [B] and [D] are the zoomed view of spray corresponding to figure [A] and [C]. N-haptain is used as fuel. [D] represents a fully developed spray.

Similarly using constant C1 = 1.52 we can illustrate our simulation like below:

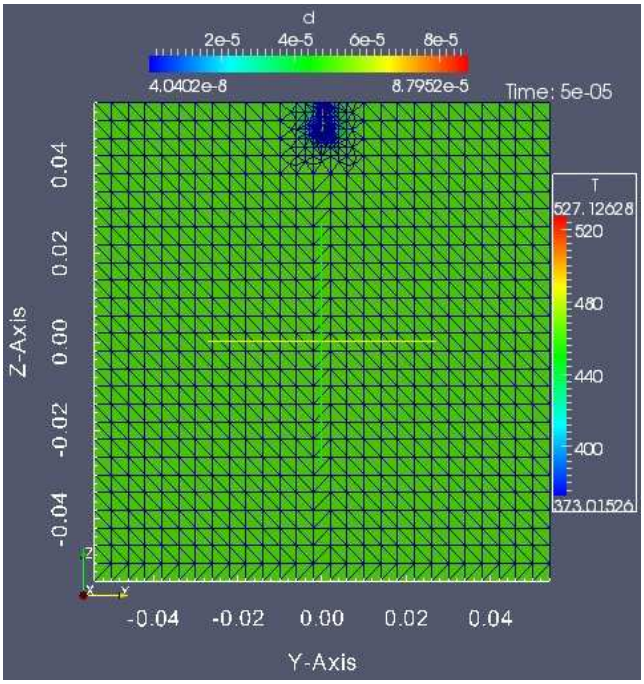

Figure-5.21 [A]

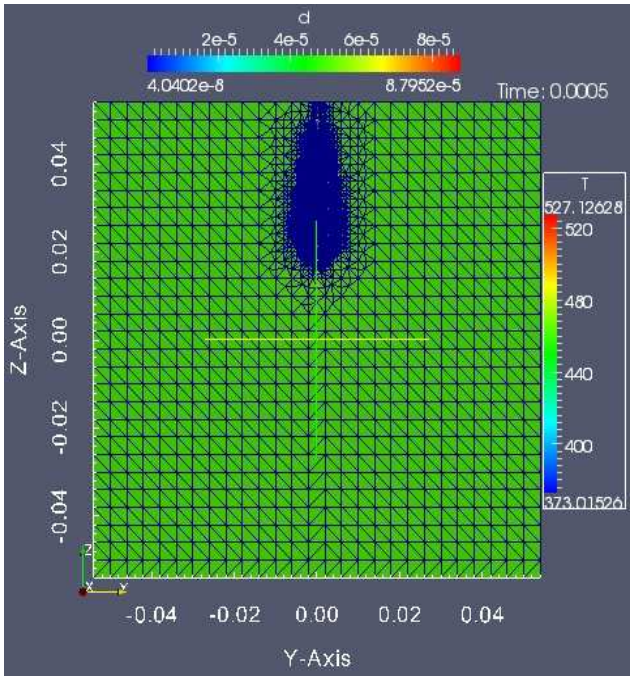

Figure-5.21 [B]

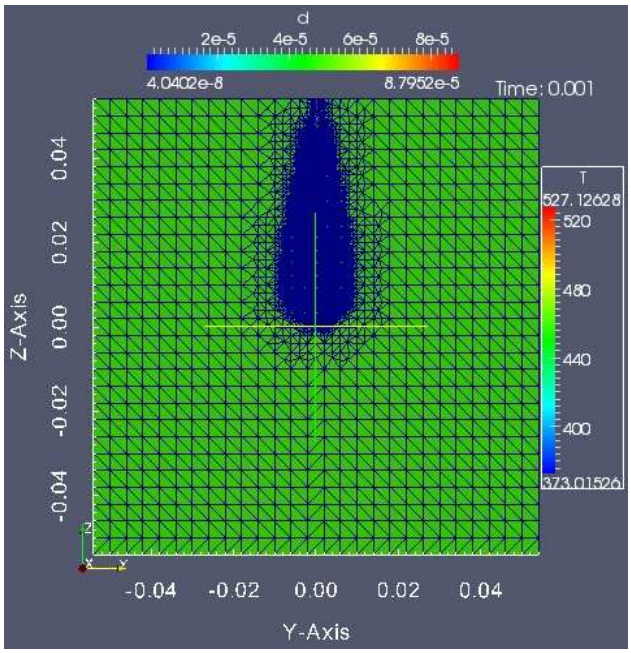

Figure-5.21 [C]

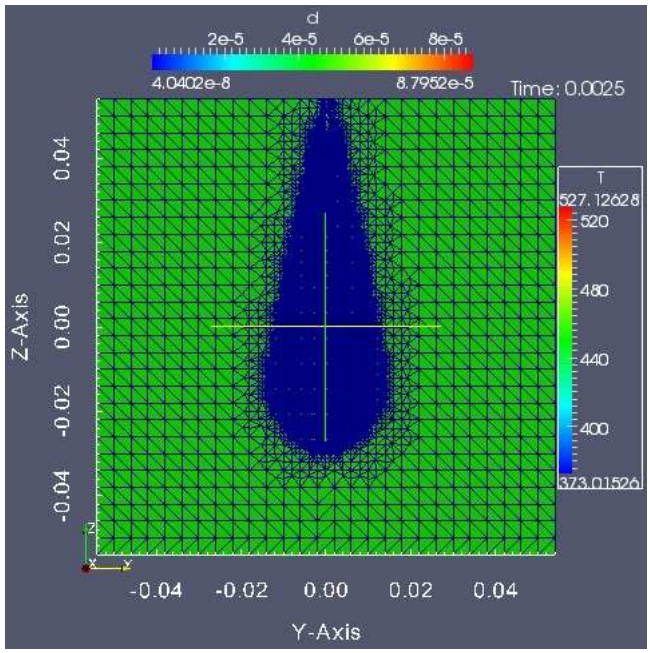

Figure-5.21 [D]

Figure-5.21: Spray and Vapor Propagation inside the Cylinder using KHRT model (with model constant, C1 = 1.52) and Huh injector for time, [A] t = 5e-5 sec, [B] t = 0.0005 sec, [C] t = 0.001 sec, [D] t = 0.0025 sec. This figure shows the change in the droplet diameter (in mm) and temperature (in K) of the particles throughout the propagation. (Fuel used = N-Heptane).

And the detailed zoomed view can be illustrated as below:

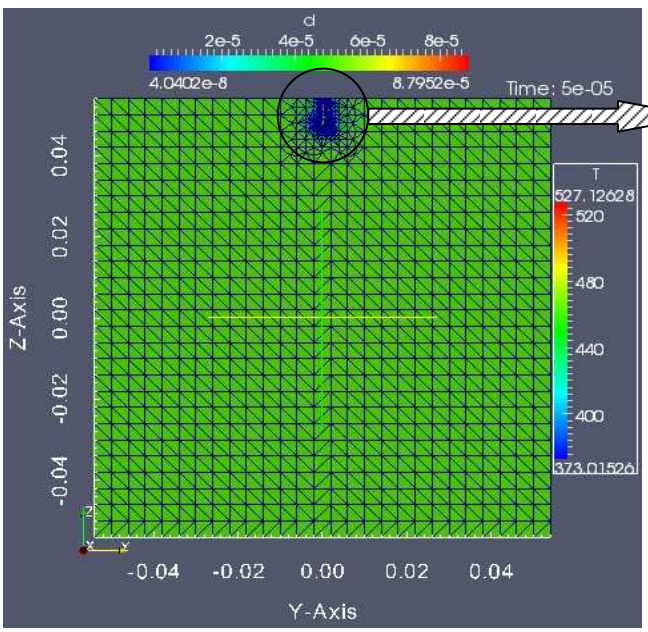

Figure-5.22 [A]

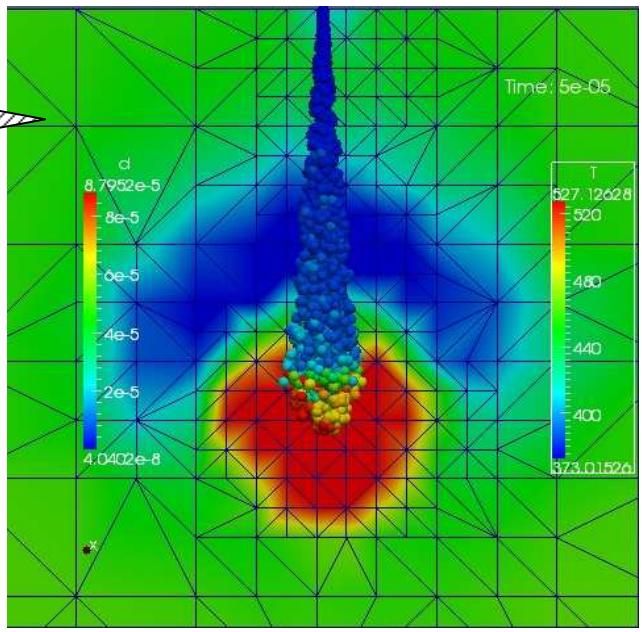

Figure-5.22 [B]

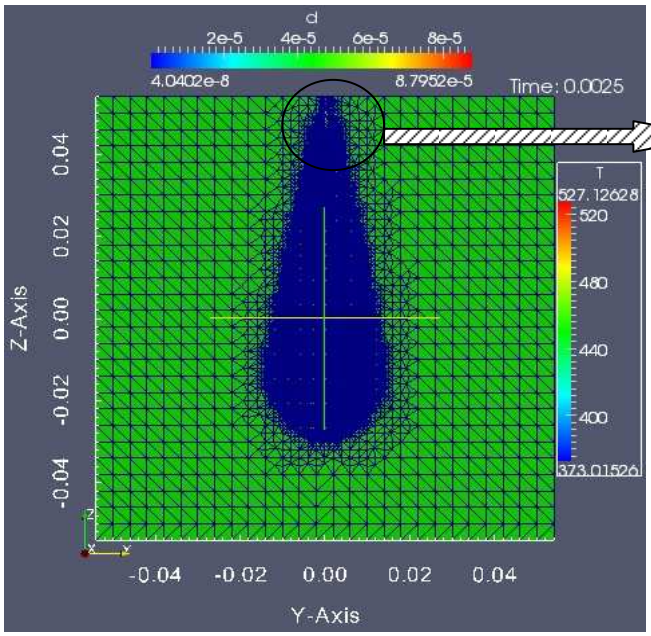

Figure-5.22[C]

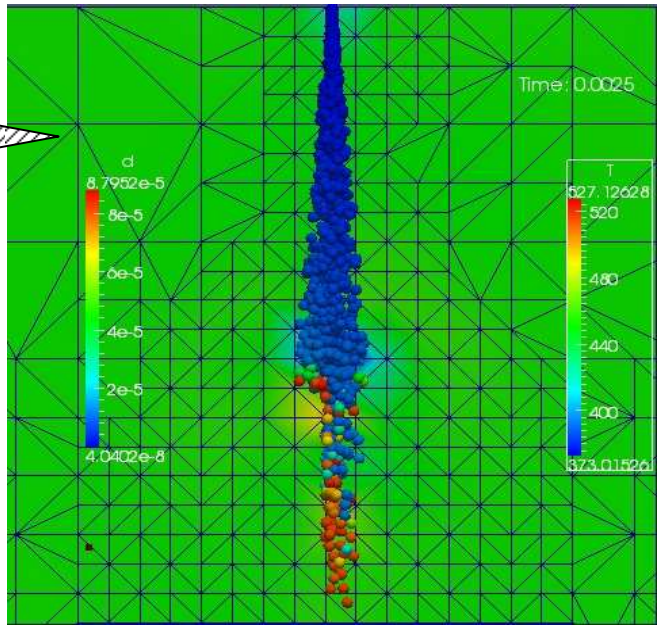

Figure-5.22[D]

Figure-5.22: Detail zoomed view of spray and nature of propagation using KHRT model (with model constant, C1 = 1.52) and Huh injector for time, [A] & [B] t = 5e-5 sec, [C] & [D] t = 0.0025 sec. [B] and [D] are the zoomed view of spray corresponding to figure [A] and [C]. N-haptain is used as fuel. [D] represents a fully developed spray.

Form figure 5.21 nd figure 5.22 here also we can see the KHRT breakup model from the spray pattern. Blue droplets has a small mass and as the time will pass, very soon these droplets will

convert in to secondary droplets which is shown by res color droplets.

We continue our simulation for another automization model known as HuH-Gosman Model. Below we are describing the finding using this method.

5.1.1.2 With Huh-Gosman Model

The spray penetration data is represented below:

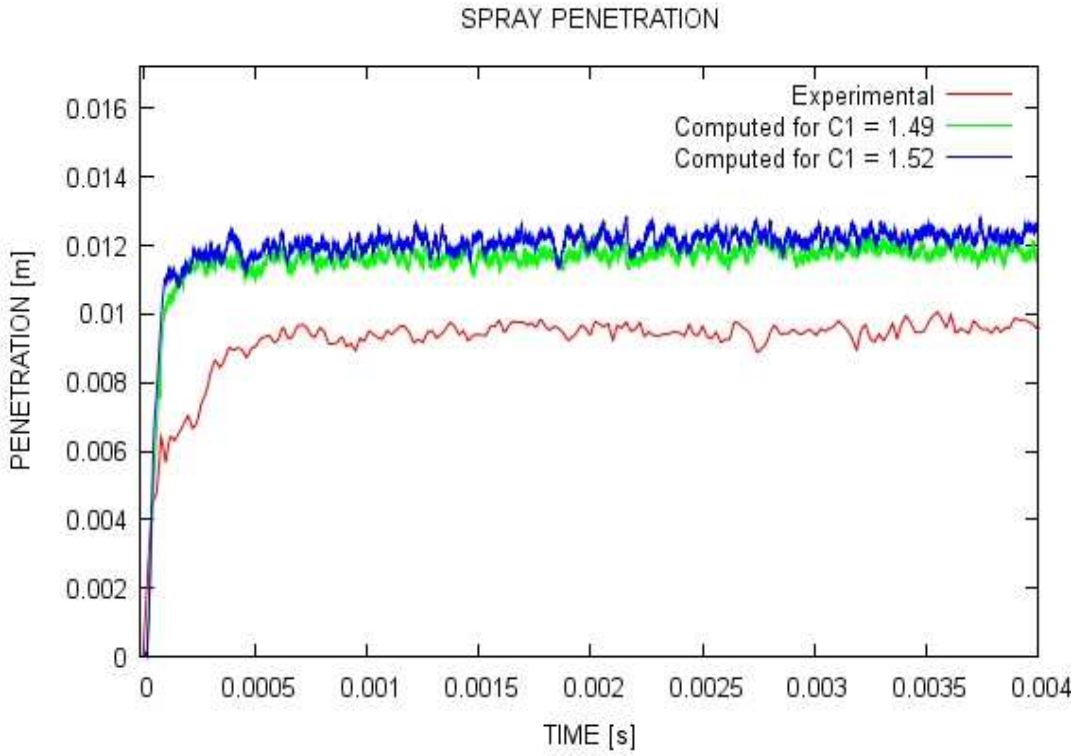

Figure-5.23: Comparison of Spray Penetration of the experimental data with the simulation one using Huh-Gosman methodology.

Here in the spray penetration data we can observe the penetration length is little bit more than the experimental data. The reason can be explained in the way that, we are introducing more larger fuel drops by this method compare to KHRT model. This may be able to produce a liquid penetration more than the previously discussed model.

Considering vapor penetration data we can figure out as below:

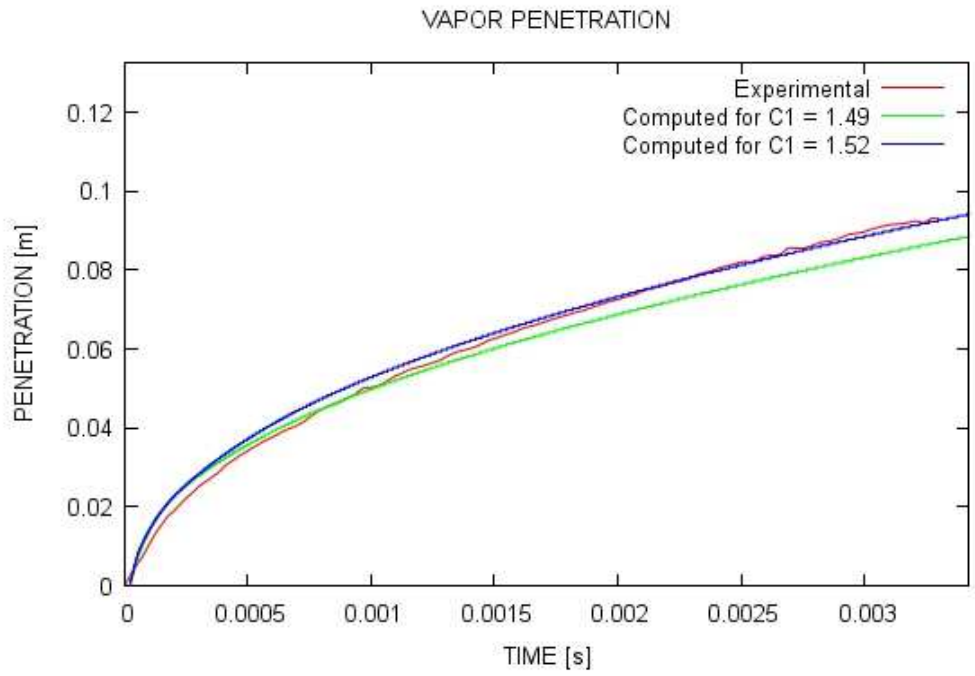

Figure-5.24: Comparison of Vapor Penetration of the experimental data with the simulation one using Huh-Gosman methodology.

Considering C_1 = 1.49 we are getting the simulation data somehow deviating a little bit from our experimental values in the fully developed steady state case of spray. Turbulence effect here is the issue. We are just modifying turbulence model with changing these model constant. As described above more turbulence in introduced by changing the value from 1.49 to 1.52 for C1. Simulation results for C1 = 1.52 give a good matching with the experimental values.

Considering axial fraction data in figure 5.25, like before what we found in KHRT model, in transient condition when the spray is not fully developed and in steady state condition the fully developed spray gives a real match with our experimental data. We can support our comment by showing one cases from transient cases (time, t = 0.05 millisecond) and one case from steady spray cases (time, t = 1.15 millisecond). All the other results for other different time steps can be found in the appendix section for further clarification of our observation.

At time, t = 0.5 ms

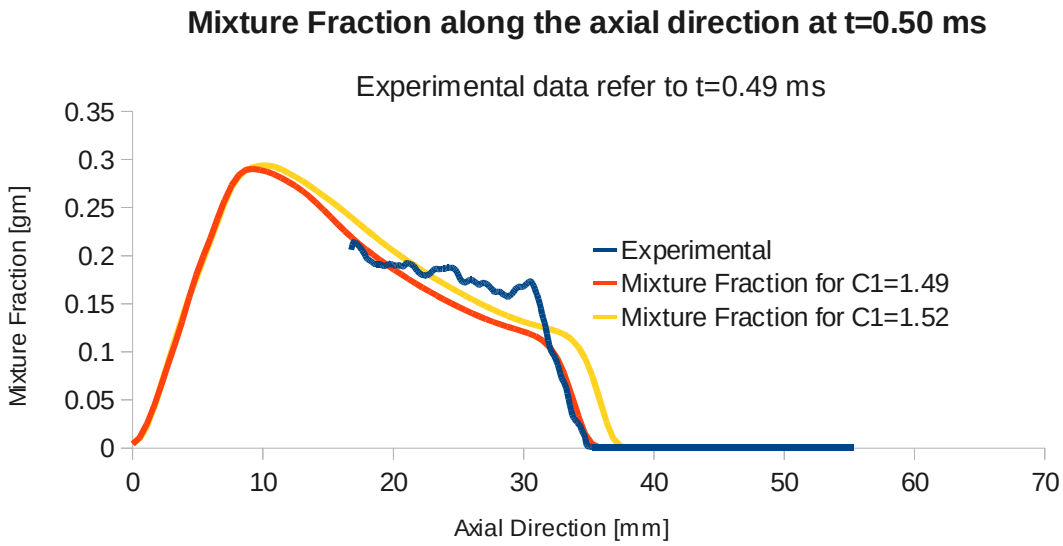

Figure-5.25 [A]

At time, t = 1.15 ms

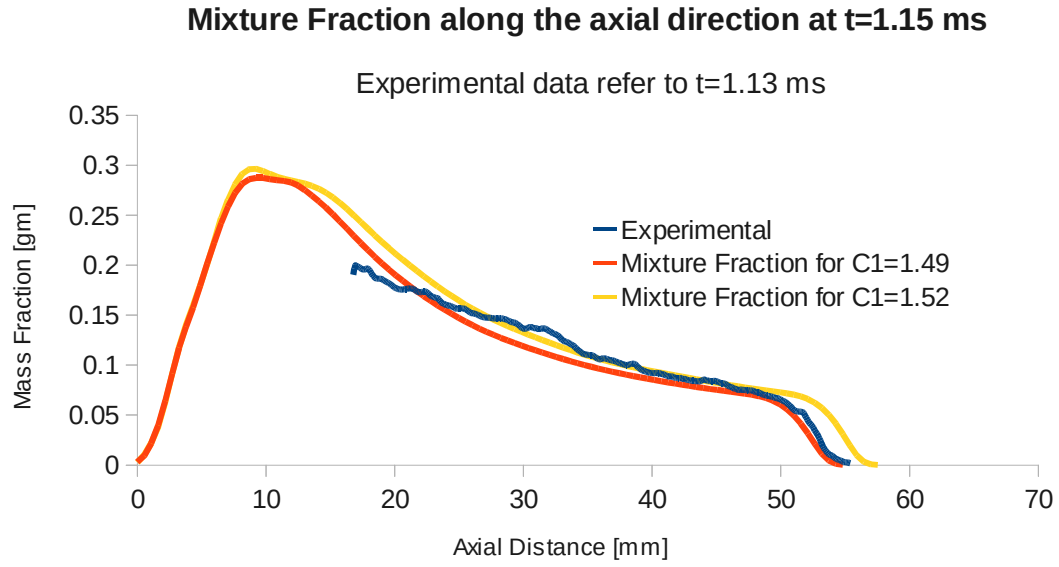

Figure-5.25 [B]

Figure-5.25-Validation of Mixture Fraction along axial direction in case of both values of C1 with Huh-Gosman Model for [A] = 0.5 ms,[B] = 1.15 ms

Mixture Fractions in Radial Direction:

Using Huh-Gosman model mixture fraction in radial direction were also checked and compared with the available experimental data.

At time, t = 0.7 ms:(transient condition)

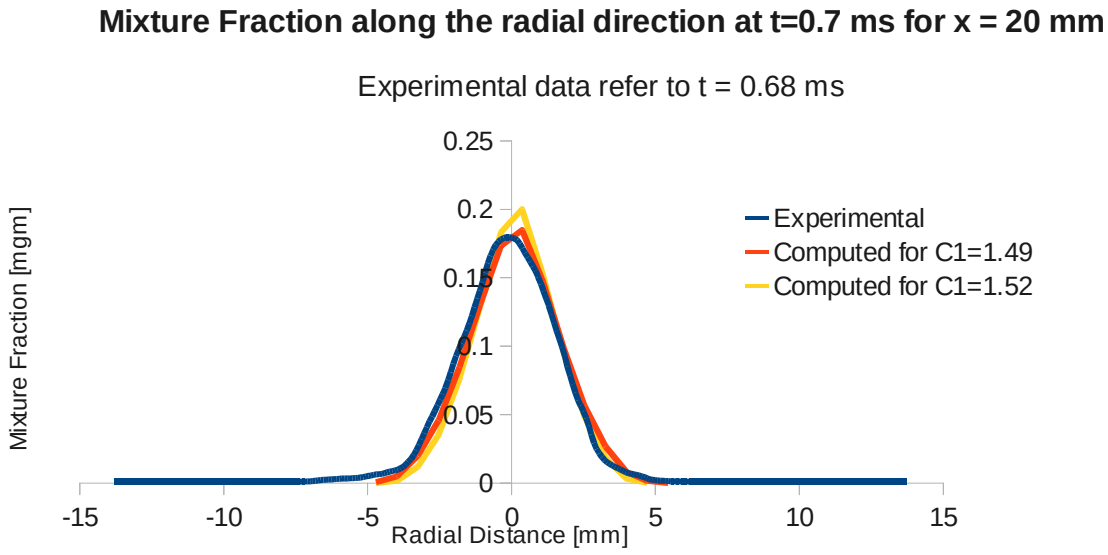

Figure-5.26 [A]

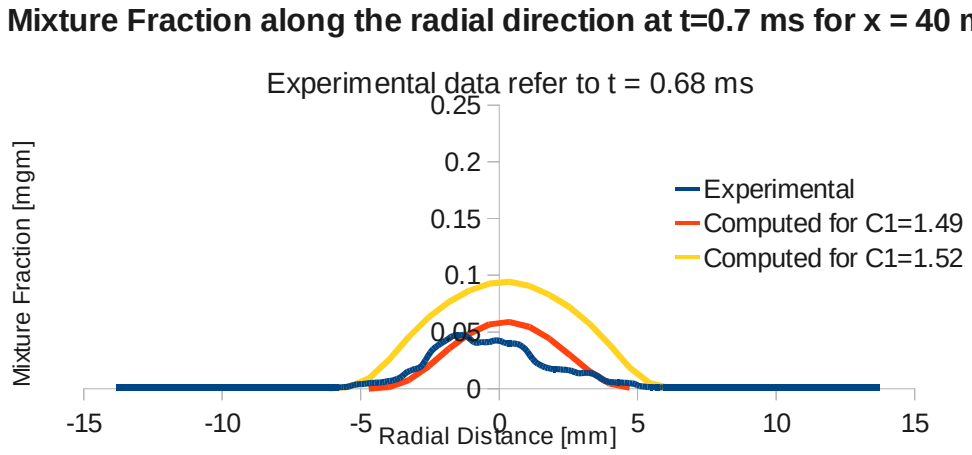

Figure-5.26 [B]

Figure-5.26: Mixture fraction comparison at time t = 0.7 ms for a distance of [A] X = 20 mm [B] X = 40 mm in radial direction.

At time, t = 1.15ms :(Steady Condition)

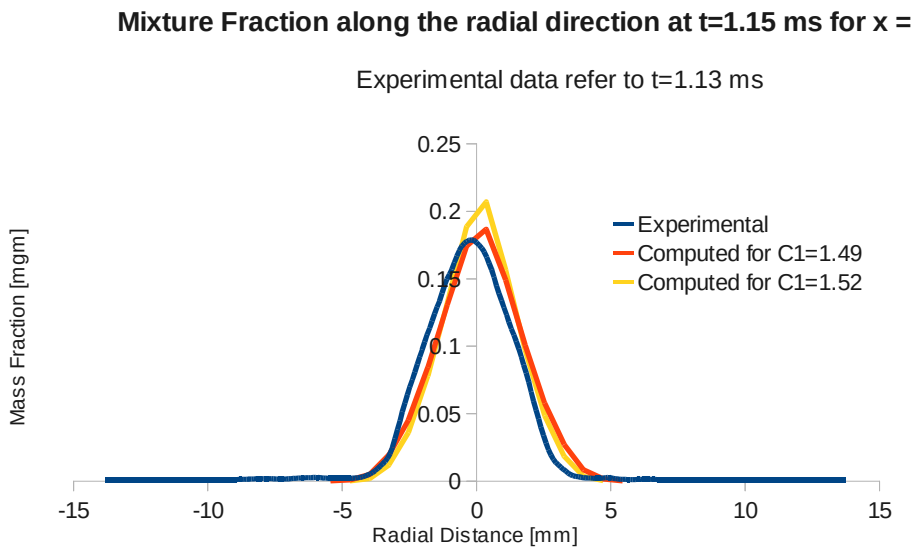

Figure -5.27 [A]

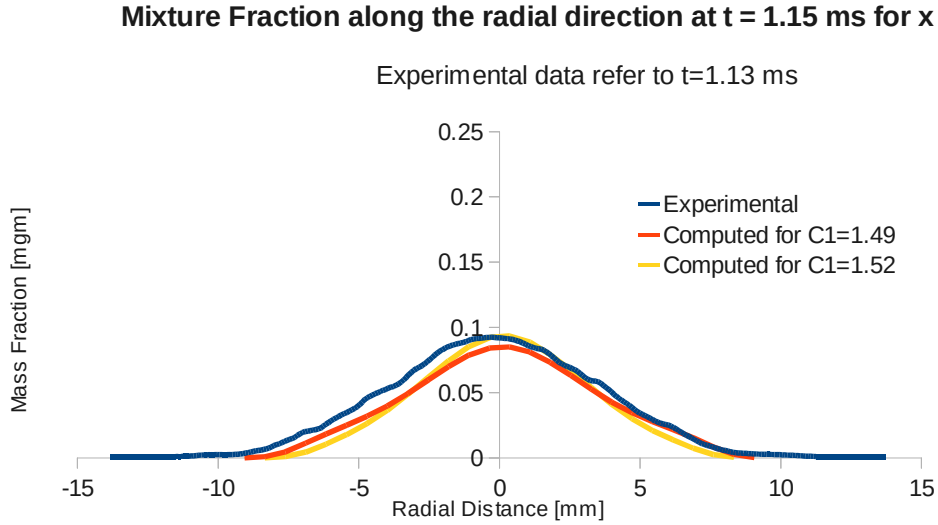

Figure- 5.27 [B])

Figure- 5.27: Mixture fraction comparison at time t = 1.15 ms for a distance of [A] X = 20 mm [B] X = 40 mm in radial direction.

Here we can found from figure 5.26 and figure 5.27 that, the mixture fraction in radial direction is also have a good match with the experimental data.

Spray Vapor penetration inside the cylinder can be using Huh-Gosman methodology is like below:

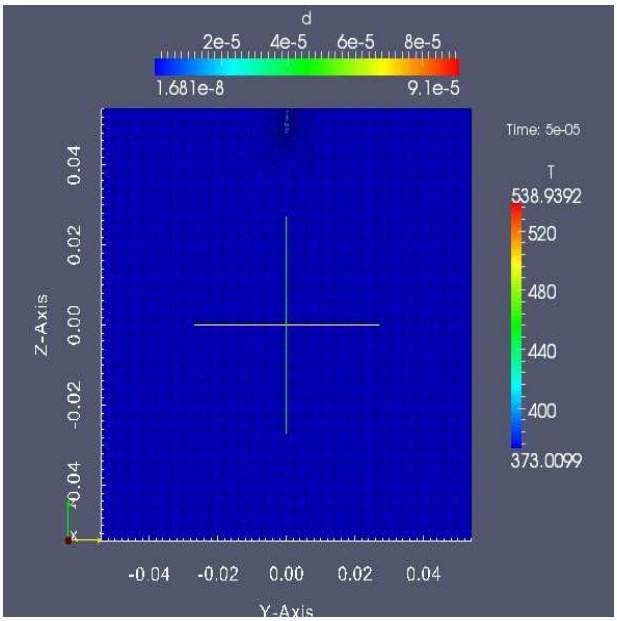

Figure 5-28 [A]

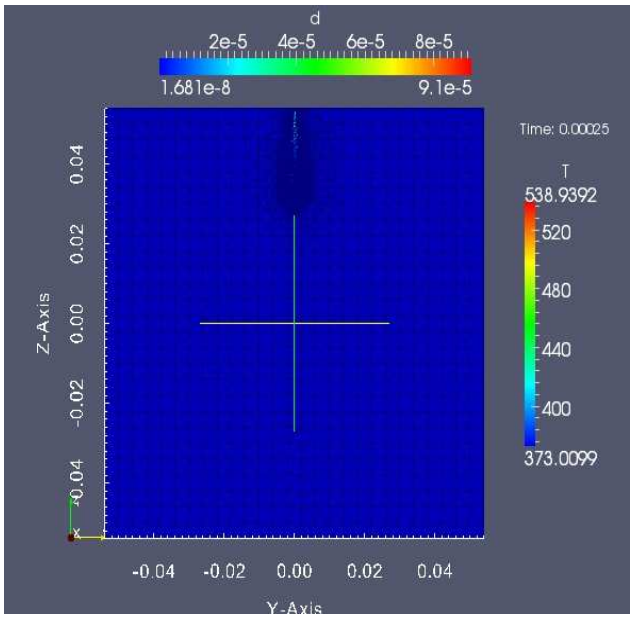

Figure 5-28 [B]

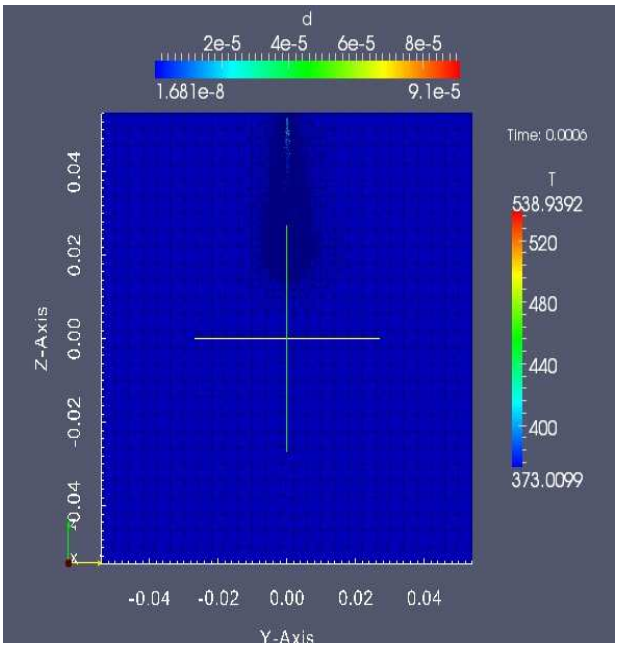

Figure 5-28 [C]

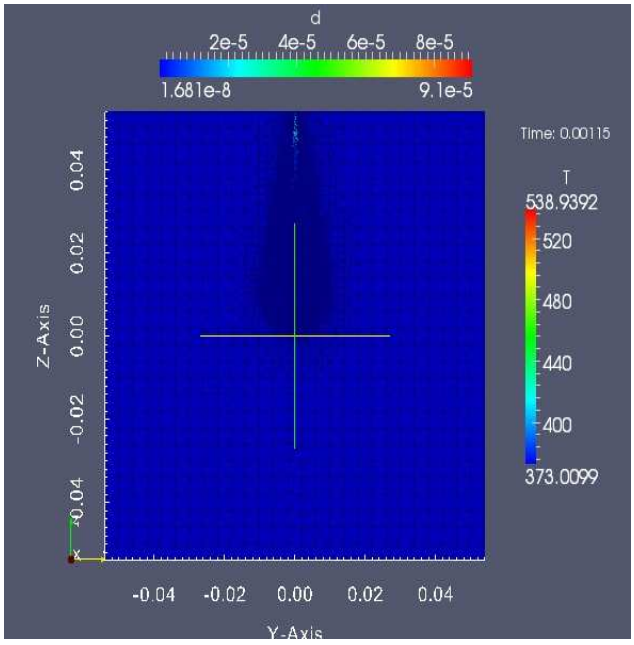

Figure 5-28 [D]

Figure 5-28: Spray and Vapor Propagation inside the Cylinder using Huh-Gosman model for time, [A] t = 5e-5 sec, [B] t = 0.00025 sec, [C] t = 0.0006 sec, [D] t = 0.0015 sec. This figure shows the change in the droplet diameter (in mm) and temperature (in K) of the particles throughout the propagation. (Fuel used = N-Heptane).

Form all the figure and writings above we can conclude that, for all the models (that we used here) we got a good similarity with the experimental results in terms of spray penetrations , vapor

penetrations and mixture fractions as well. Every case we can see that, as we move towards more time duration we will get a good mixture fractions, especially for further distance from the injector. Our results thus verify our model as a proper working model. We will use the model to verify it further with also another fuel which is known as Spray A or Dodecane. Like N-Heptane we will try to verify our model comparing with the experimental data. Here also we will use spray and vapor penetrations and mixture fractions both in axial and radial direction of the combustion chamber to proof our model as a faithful one. All the results using Spray A are illustrated below.

5.2 Spray A

The CFD analysis for Spary A also give some good matching result with the Spray and Vapor experimental data (ECN Sandia [49, 50]) as well as with the experimental data of mixture fraction in radial direction (Pickett et. Al, 2011 [54]). The injector nozzle is a Bosch CRIP 2.2 injector with a KS1.5/86 orifice and diameter equal to 0.090 mm. Fuel is pure n-dodecane at 90º C tip temperature. In the non-reacting conditions the oxygen concentration was equal to 0 and the ambient temperature and density were respectively equal to 900 K and 22.8 kg/m3. The detail specification of Spray-A can be found in the Index portion.

5.2.1 Using KHRT model with Blob injector:

Spray Penetrations:

If we look the spray penetration using this model for Spray A, it will be like below:

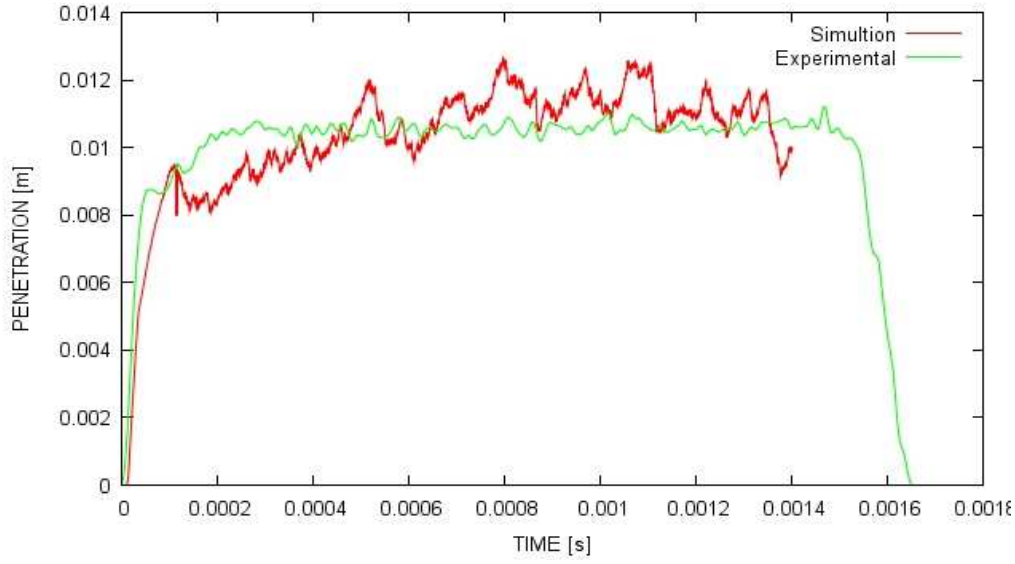

Figure 5-29: Comparison of Spray Penetration of the experimental data with the simulation one using KHRT methodology for spray A fuel.

Vapor Penetrations:

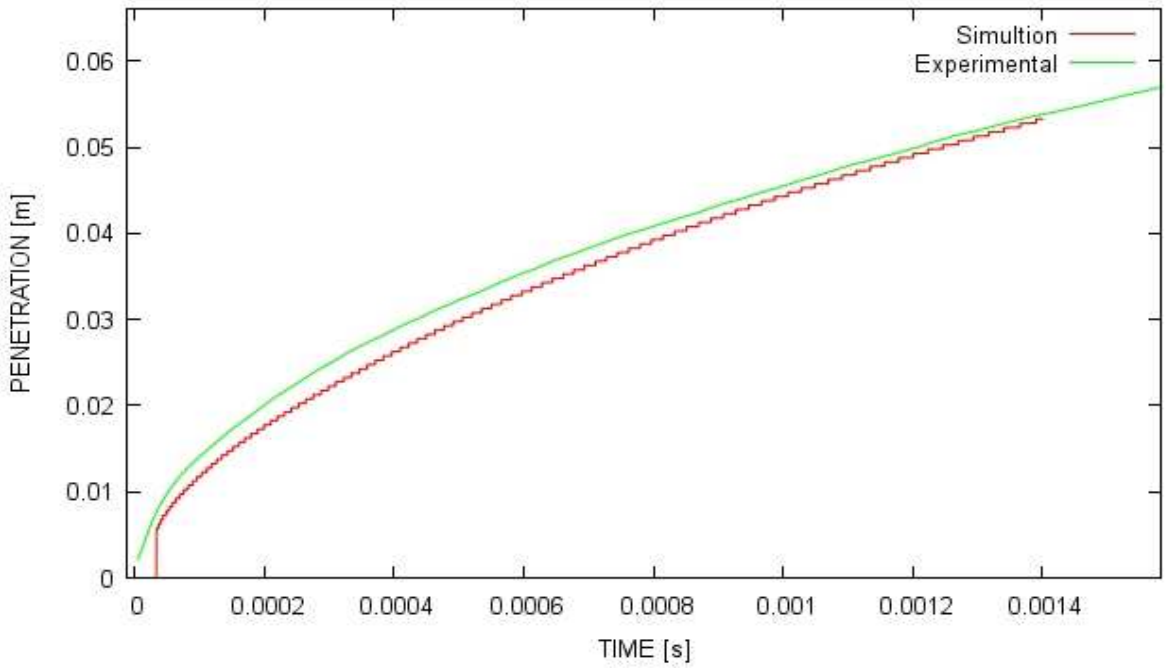

Figure 5-30: Comparison of Vapor Penetration of the experimental data with the simulation one using KHRT methodology for spray A fuel.

For both the cases of figure 5.29 and 5.30 we can see the spray liquid and vapor penetration gives a good approximation with the experimental data. In case of figure 5.28 in the simulated data we may found some fluctuation of data around the experimental data, but the overall trend of the curve is matching the experimental values. We have considered only for C1 = 1.52 in our Spray-A case data since we found a lot of perfect matching considering this value in the turbulence model of simulation.

Like KHRT model here also we compare our simulation data with corresponding axial and radial mixture fraction for different time and different position in the combustion chamber. Our simulations in this case also give a good matching for Spray-A fuel. Spray A fuel is much more importance as it has many similarity conditions with the real fuel we use. We consider always the steady flow data as for transient cases no experimental data was not available. And matching data with steady condition actually make more sense to work as good simulation. Below we are describing our findings regarding axial and radial mixture fraction simulations.

Axial Mixture Fraction:

Comparing axial mixture fraction for a fully developed spray we get the following result:

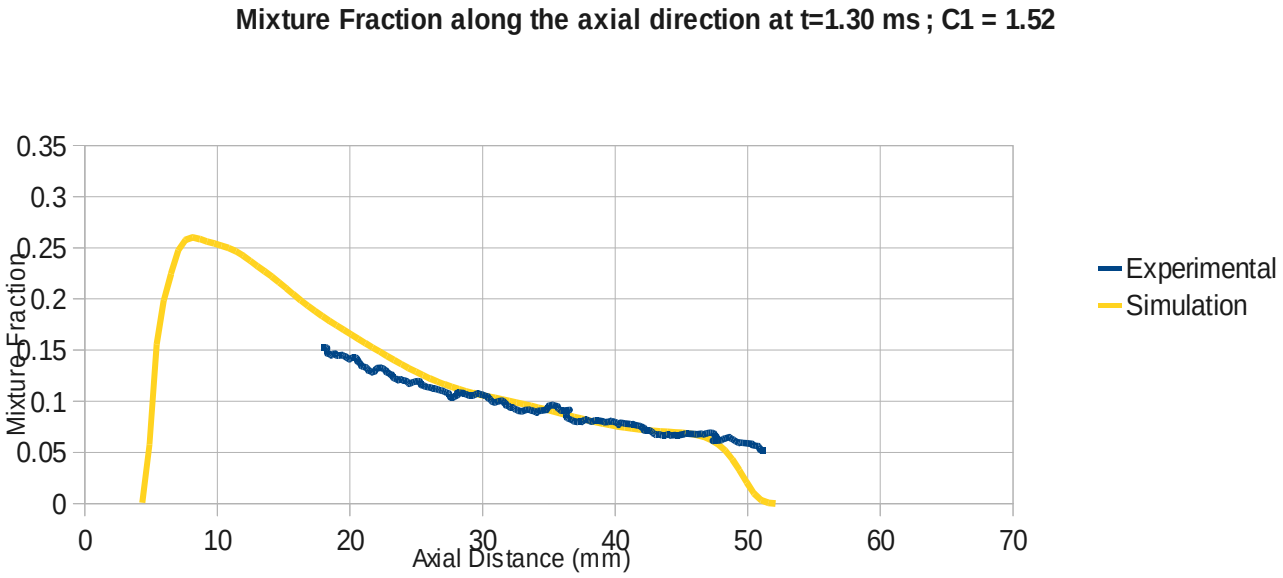

Figure5-31: Validation of Mixture Fraction along axial direction

Blue line in the figure 5.31 represents the experimental data. If we limit our simulation data from 15 mm to 55 mm axial distance (direction along the axis of injector) we can observe easily that how the simulation and experimental data are matching in good ways. On the basis of this data we can ensure about the validation of our model for this fuel also.

Now considering radial case and only for steady condition of fuel spray we found the following results.

Mixture Fraction in Radial Direction:

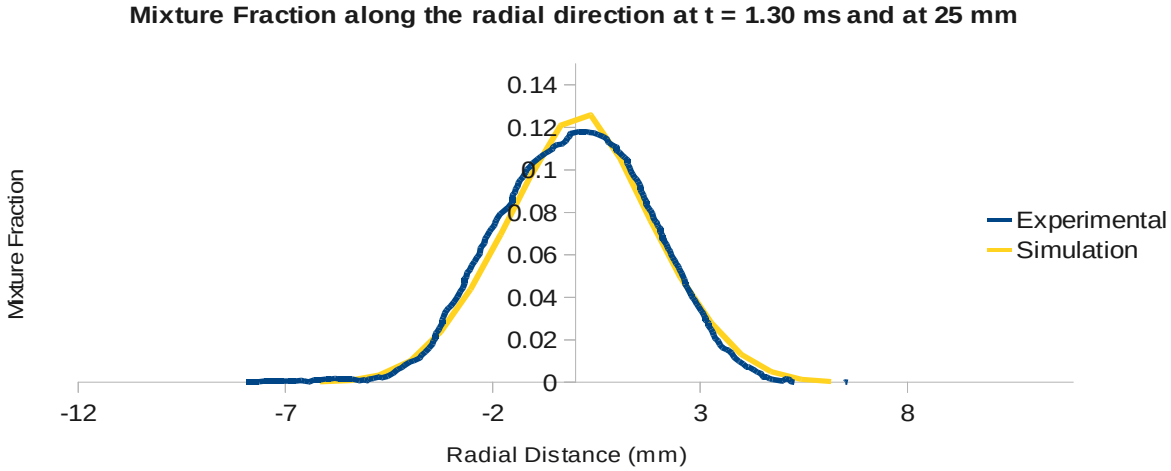

Figure 5-32 [A]

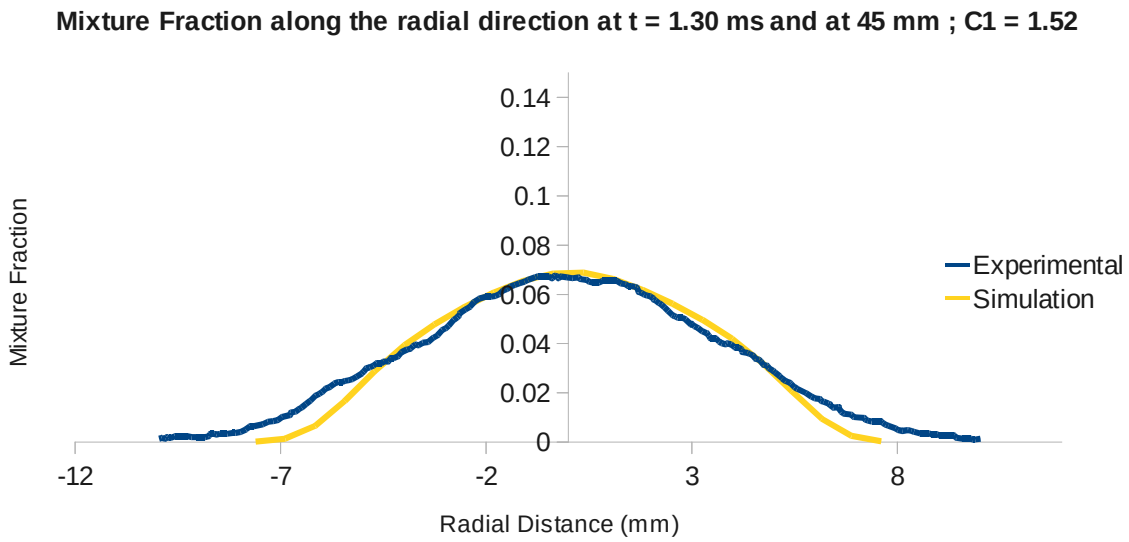

Figure 5-32 [B]

Figure 5-32: Validation of Mixture Fraction along radial direction for fully developed Spray (at time, t = 1.13 ms) [A] at distance 25 mm, [B] at distance 45 mm.

In the figure of 5.32 we represented the radial mixture fraction data of fuel spray for two cases. As shown figure 5.32 [A] represents data in 25 mm distance along the injector axis and figure 5.32 [B] represents radial mixture fraction data for 45 mm distance along the axis of injector. For both the cases, the spray is in steady condition i.e. got enough time to be steady. The matching between the experimental and experimental data is visible in these figures. We can conclude here that these radial and axial mixture fraction matching data as well as considering spray and vapor penetration, the simulation has a good reason validate.

Let us have a look with the spray penetration pattern inside the cylinder. We will cut a plane in the middle of the combustion chamber as well as through the middle of injector and we can observe the spray penetrating like as shown in figure 5.33. With the increase of the time the penetration of the spray is increasing.

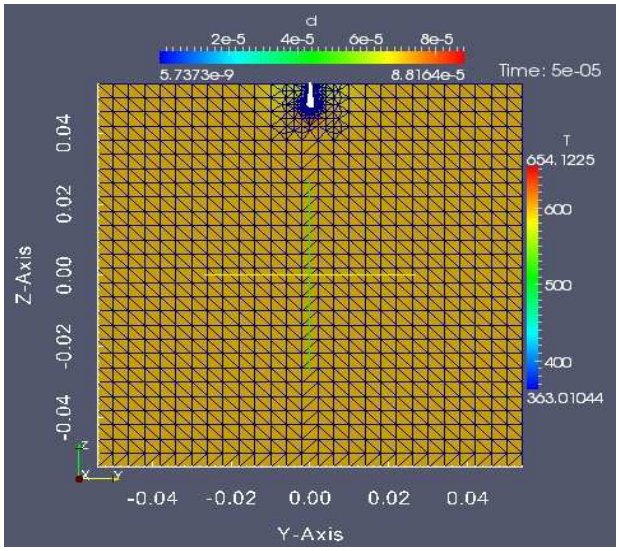

Figure 5-33 [A]

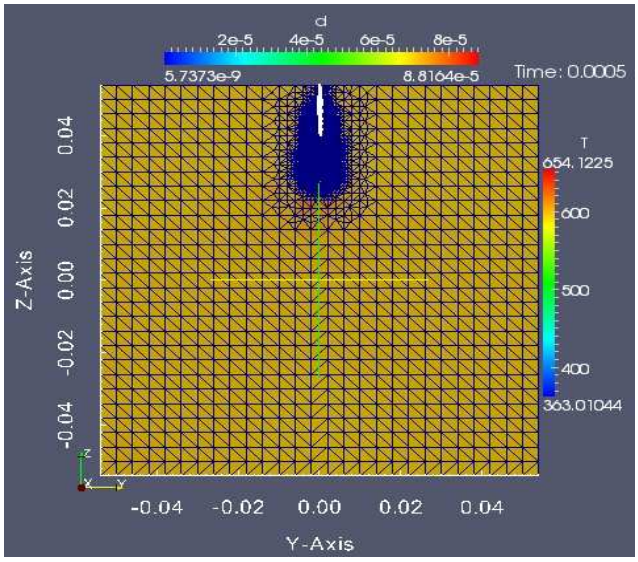

Figure 5-33 [B]

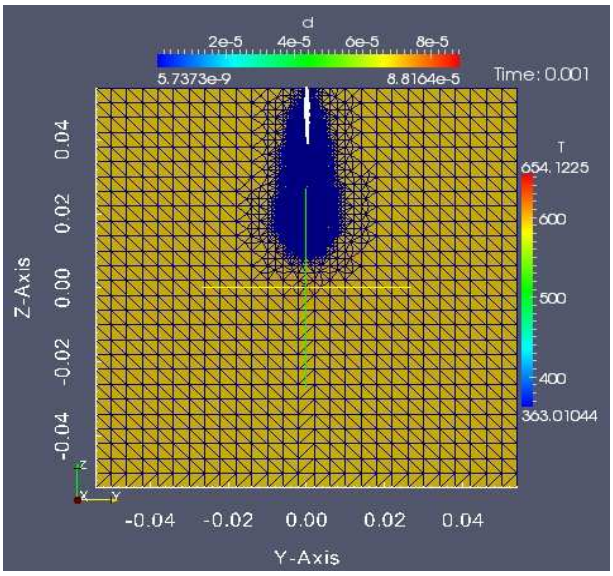

Figure 5-33 [C]

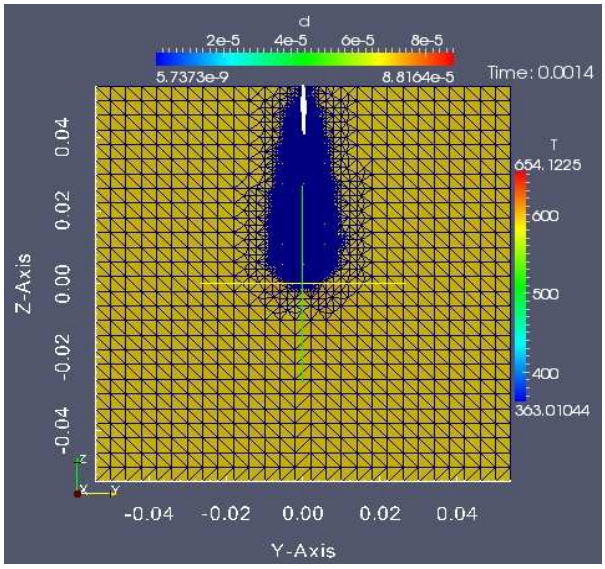

Figure 5-33 [D]

Figure 5-33: Spray and Vapor Propagation inside the Cylinder using KHRT model for time, [A] t = 5e-5 sec, [B] t = 0.0005 sec, [C] t = 0.001 sec, [D] t = 0.0014 sec. This figure shows the change in the droplet diameter (in mm) and temperature (in K) of the particles throughout the propagation. (Fuel used = Spray A i.e. Dodecane).

Spary pattern and detailed zoom view is represented here for a fully developed spray for time t = 0.00135 sec.

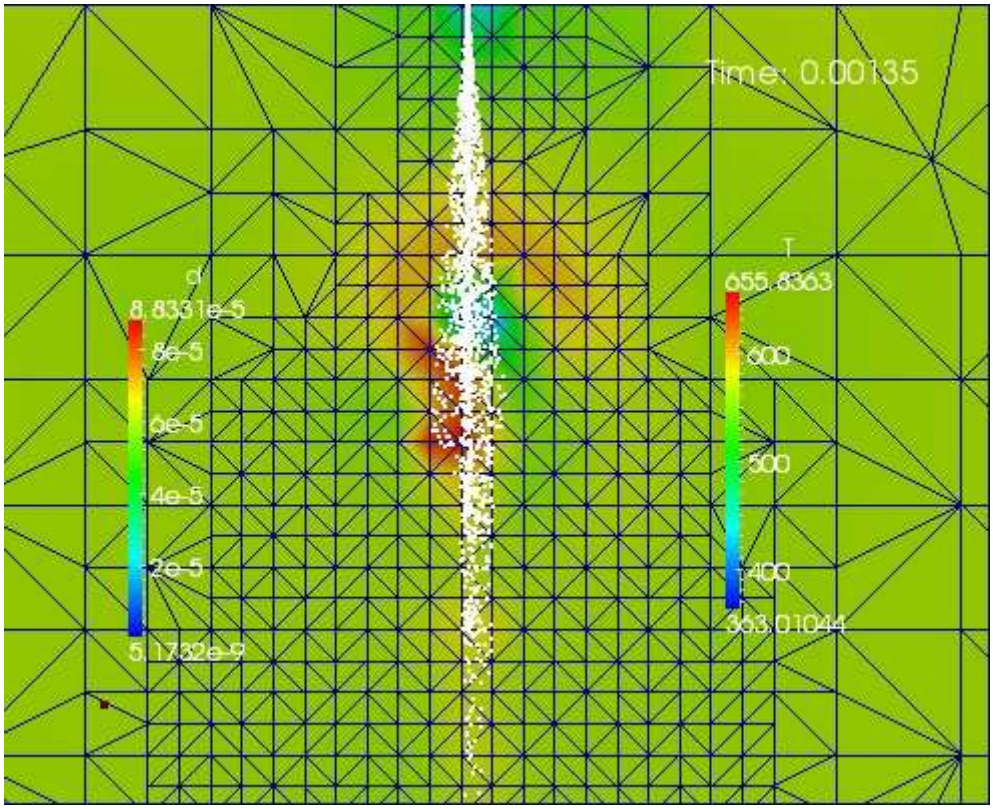

Figure 5-34: Spray pattern inside the cylinder. For spray-A using KHRT model.

5.2.2 Huh-Gosman Methodology

Our simulation is also tested using Spray A. And like other cases here also we got good matching with our experimental values. Here we are describing our results through below figures:

If we go through the figures of 5.35 and 5.36 where we represented the data of spray penetration and vapor penetration using Huh-Gosman Methodology for Spray-A fuel, we will see that both the spray and vapor penetration is actually penetrating little bit more than the experimental data. The same results also we found for the case of n-heptane fuel. The reason can be the same as described for n-heptane fuel. By using Huh-Gosman Model we actually introducing fuel with large droplet and this is a reason to penetrate a little-bit more than the experimental results.

Spray Penetration:

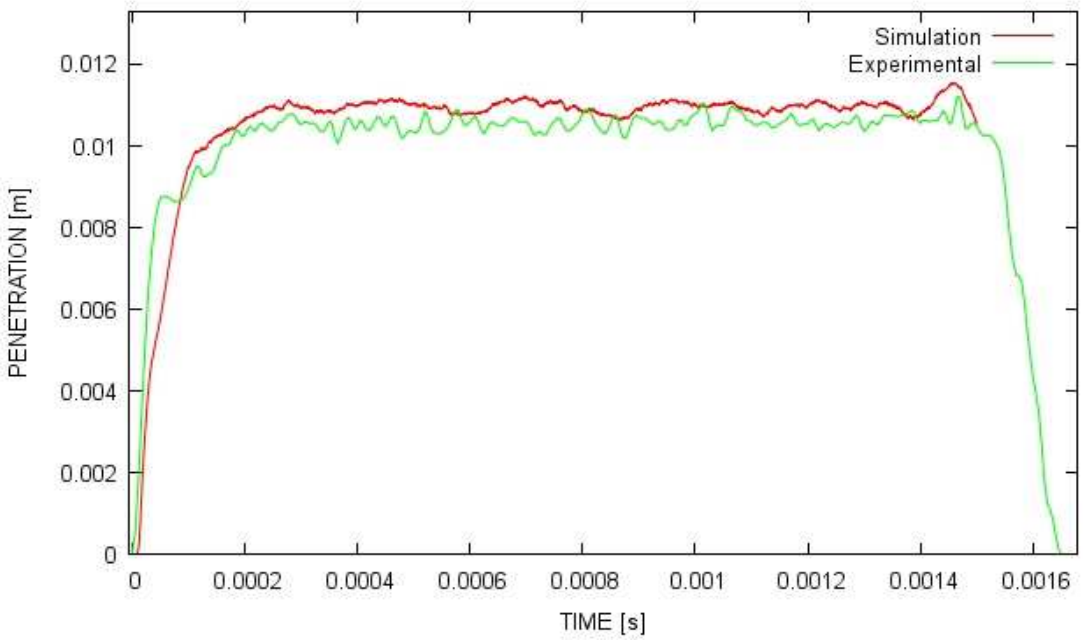

Figure 5-35: Comparison of Spray Penetration of the experimental data with the simulation one using Huh-Gosman methodology for spray A fuel.

Vapor Penetration:

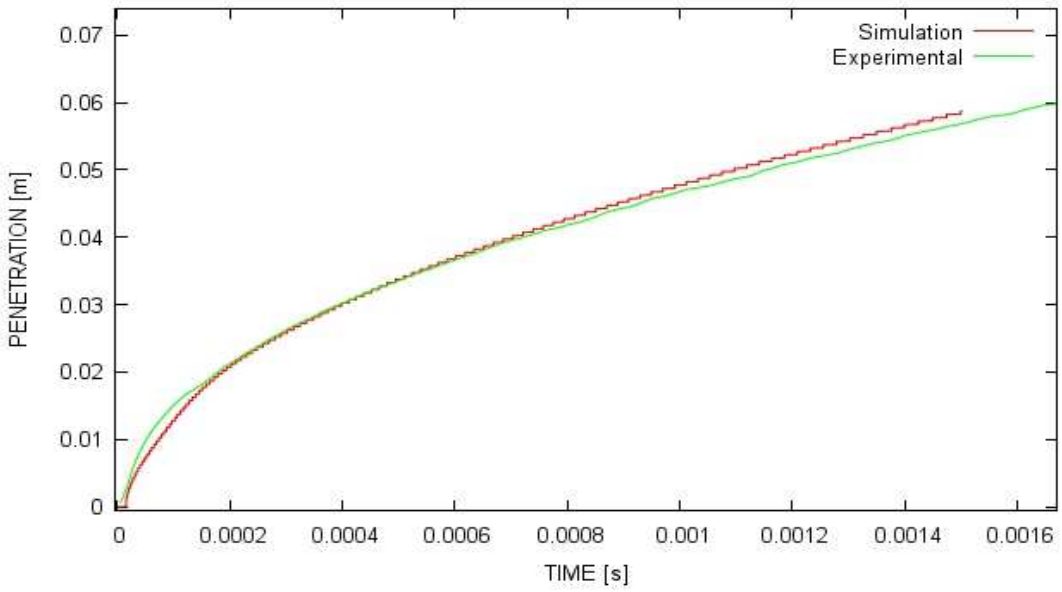

Figure 5-36: Comparison of Vapor Penetration of the experimental data with the simulation one using Huh-Gosman methodology for spray A fuel.

Mixture Fraction in Axial Direction:

We get following result comparing with the experimental data:

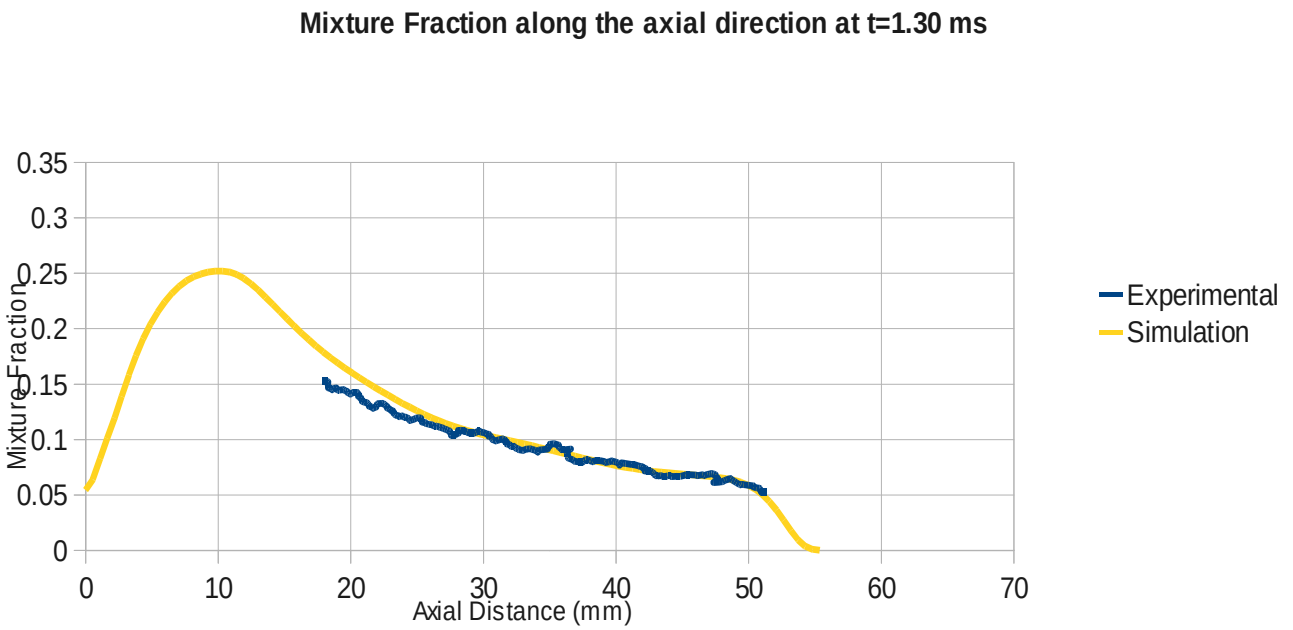

Figure 5-37: Comparison of Axial Mass Fraction data with the experimental data using Huh-Gosman methodology for fully developed spray A fuel.

Our experimental data is available only in the axial distance of 17 to 53 mm which is shown in figure 5.37. Limiting our simulated results in this section we can observe a good matching with the simulation and experimental results.

Considering figure 5.38 which gives an idea of radial mixture fraction data for a steady flow condition, we found that simulation data are slightly approaching above from the experimental data but overall showing a good matching with the experimental one. When we are moving far in the radial direction we are visualizing more deviation of the data. It means for actual cases, the mixture propagation is not smooth like simulated one as we move further from axial axis. In reality it can happen due to the turbulence effect and taking other factors in to consideration.

Mixture Fraction in Radial Direction:

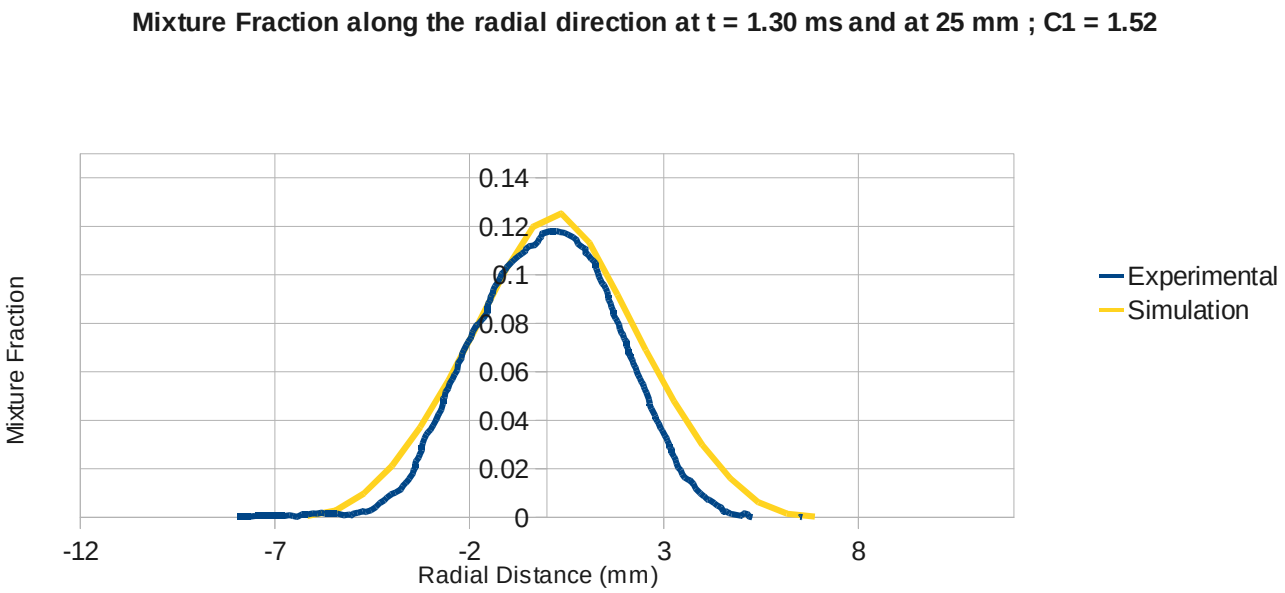

Figure 5-38 [A]

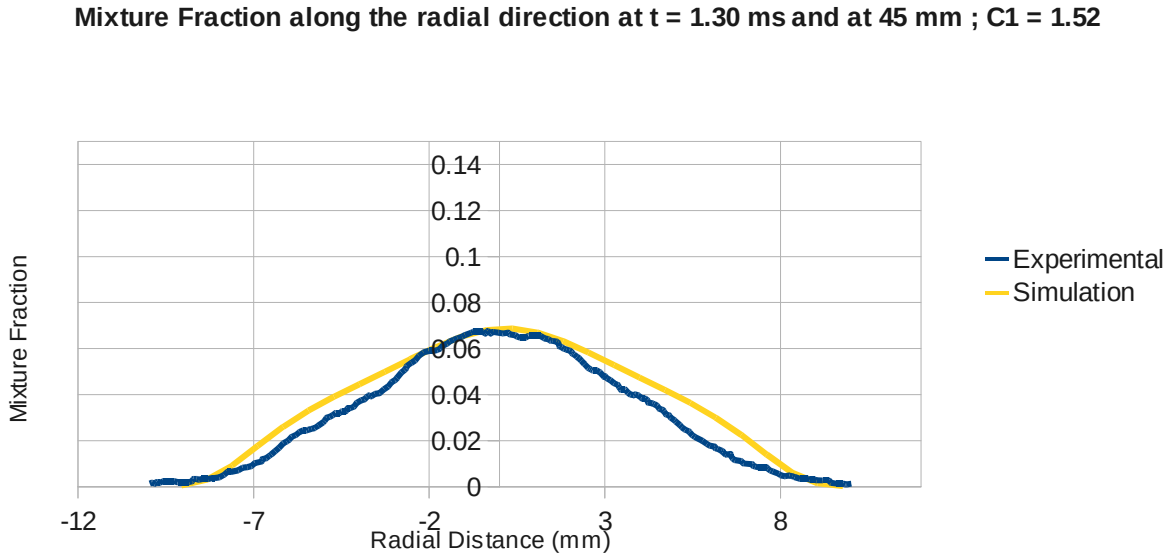

Figure 5-38 [B]

Figure 5-38: Validation of Mixture Fraction along radial direction for fully developed Spray (at time, t = 1.13 ms) [A] at distance 25 mm, [B] at distance 45 mm.

In this chapter we have discussed about all the simulation and corresponding experimental results to support the validation of our model. For all cases we have performed the simulation for non-reacting cases i.e. without any oxygen. The importance of non-reacting condition is that, non reacting case is the most important to understand the chemistry of the fuel spray inside the combustion chamber. To know the pattern and actual behavior of fuel spray non reacting condition is considered to have maximum significance.

Considering all the results that we got like spray and vapor penetration, mixture fraction data in both radial and axial direction we can conclude that our model has lots of reason for validation. In all cases we got good and acceptable results which make our model particular.

CHAPTER 6

6. Conclusion and Recommendation

6.1 Conclusion:

A theoretical investigation based on CFD modeling has been performed with the aim of Validation of atomization and evaporation models for fuel spray in constant-volume experiments under non-reacting conditions.

A comprehensive methodology to describe the liquid and vapor evolution of the fuel spray for Diesel applications was assessed in this work by simulating evaporating spray of pure n-heptane and n-dodecane in a constant volume chamber . Attention was mainly given on the evaluation of the models to predict the vapor penetrations and distributions in steady and transient conditions for non-reacting spray. This aspect is considered to be a fundamental prerequisite for any future investigation of the following combustion processes.

The developed spray model accounts for the physical phenomena of accelerative Rayleith-tailor type instability on the surface of the droplets as well as accounting for the Kelvin-Helmholz waves which form due to aerodynamic instabilities.

Despite the two atomization models lead to good matching results with the experimental values, some relevant differences can be observed in terms of primary and secondary breakup contributions to the overall process. Within Blob framework, droplet disintegration is demanded to secondary breakup, whose effect must be adequately enhanced to match the experimental measurements. On the other hand, the Huh-Gosman simulation produces very small droplets by the primary breakup itself and secondary breakup must be limited in order to avoid excessive droplets disintegration.

6.2 Further Recommendation:

Although the model predictions have been very successful, further following works can be done to shine it properly:

A] To develop our model for reacting conditions. Ours one used here for all cases was non-reacting

cases.

B] To assess the influence of intake flows on emissions and to test the model performance over wider ranges of engine operating conditions.

C] Additional model development is needed to improve the prediction of late injection cases which tend to underestimate combustion rates.

D] Future directions of research include improvements to the turbulence model and alternative flameletbased combustion models. Further development of emission models is needed for quantitative analysis of pollutant formation mechanisms. More predictive soot formation and oxidation models that account for soot particle size variations during combustion are being analyzed. With the combination of informative experiments and improved predictive models it will be possible to explore strategies for engine pollutant emission control more effectively in the future.

APPENDIX

A. Results for KHRT Model Using Huh Injector:

A1. Mixture Fractions in Axial Direction:

At time, t = 0.5 ms:

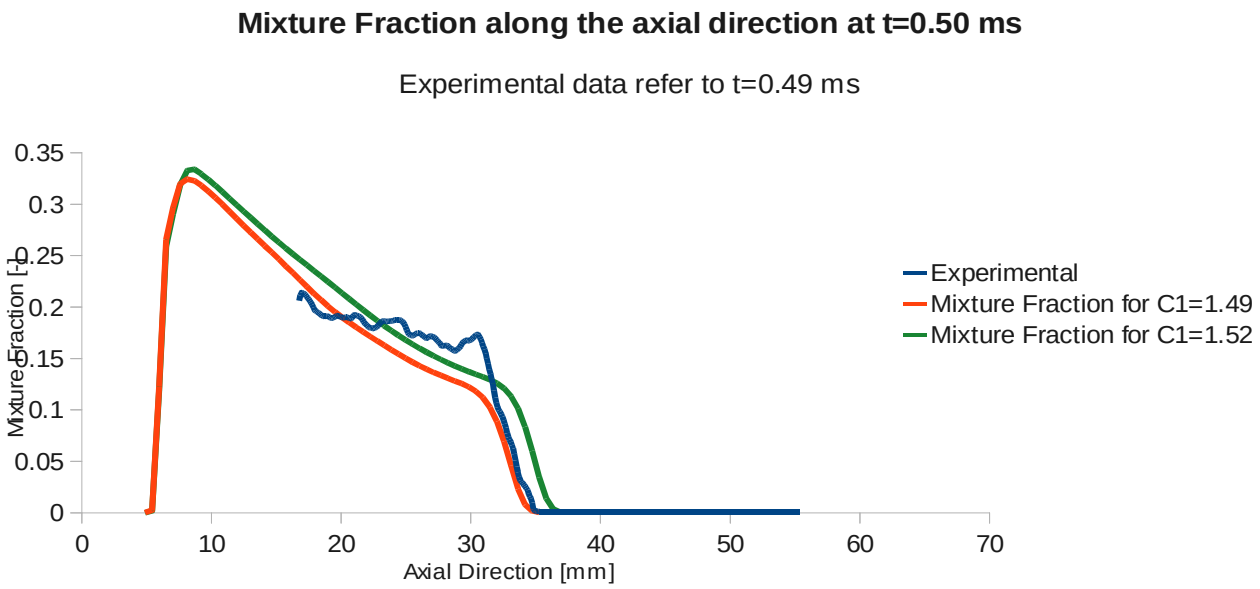

(A)

At time, t = 0.7 ms:

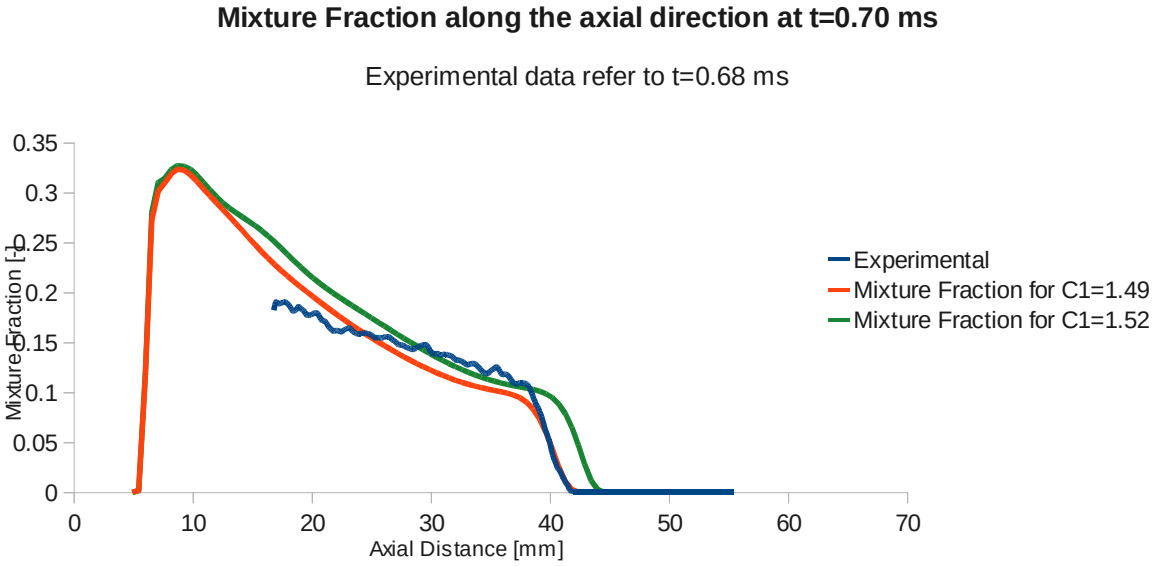

(B)

At time, t = 0.9 ms:

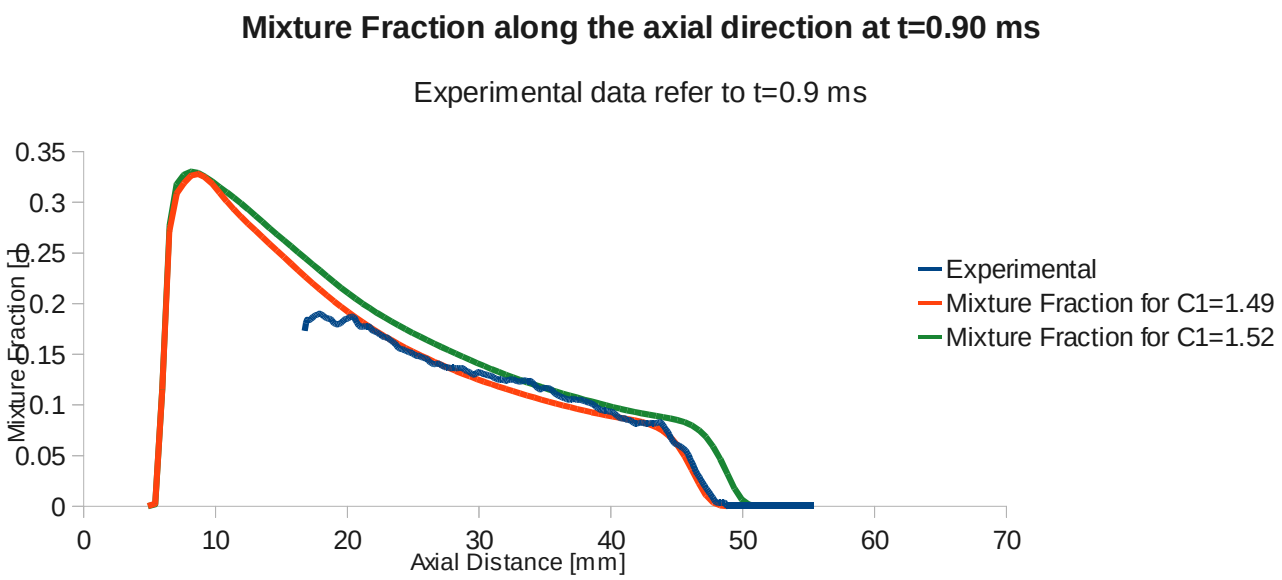

(C)

At time, t = 1.15 ms :

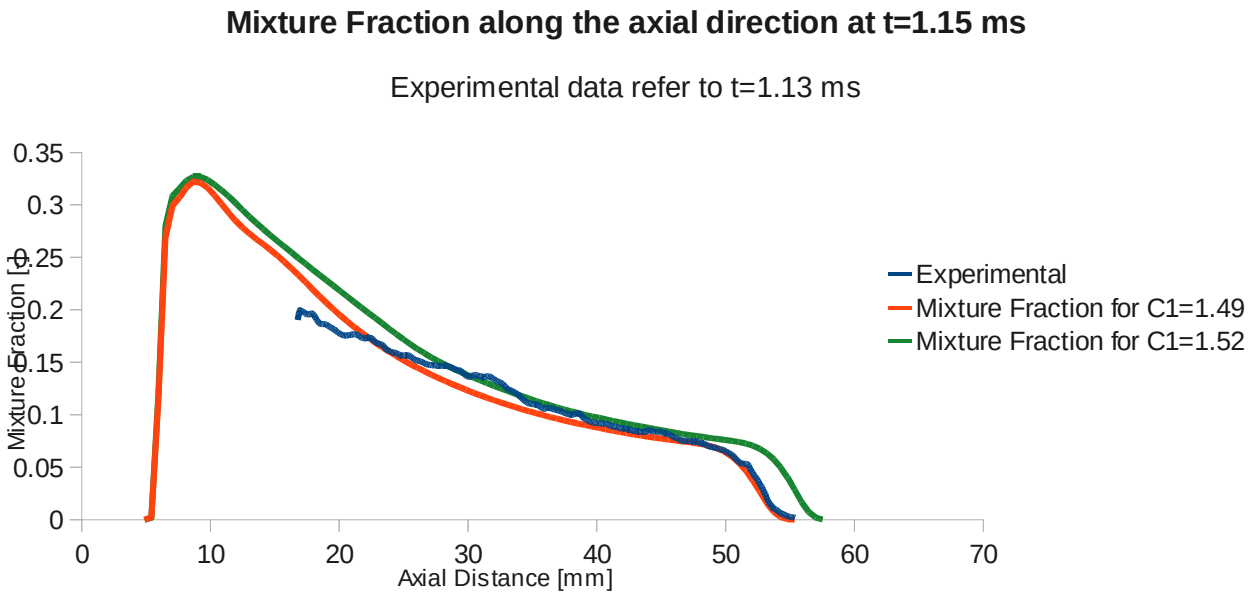

(D)

Figure A1 : Validation of Mixture Fraction along axial direction in case of both values of C1 for (A) = 0.5 ms, (B) = 0.7 ms, (C) = 0.9 ms, (D) = 1.15 ms

A2. Mixture Fractions in Radial Direction:

A2.1: At Time, t = 0.5 ms

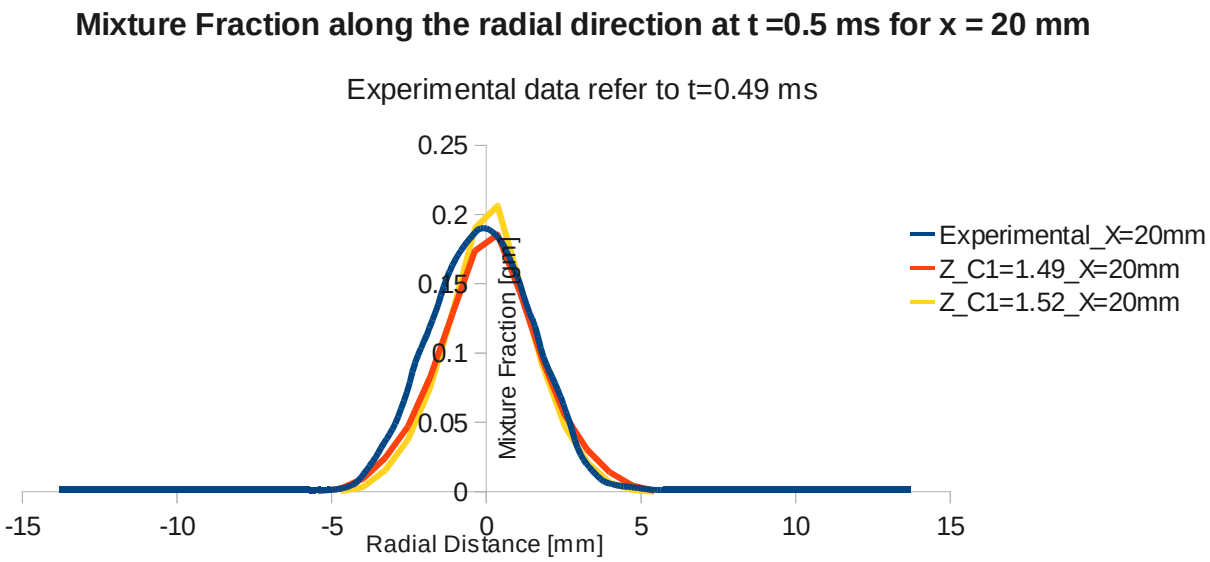

(A)

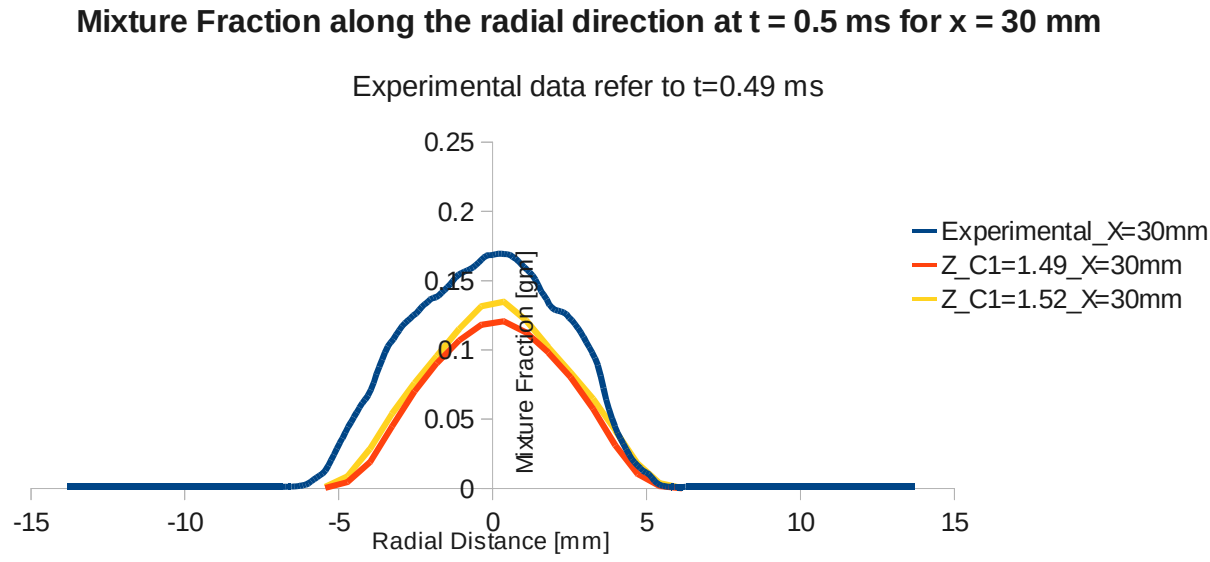

(B)

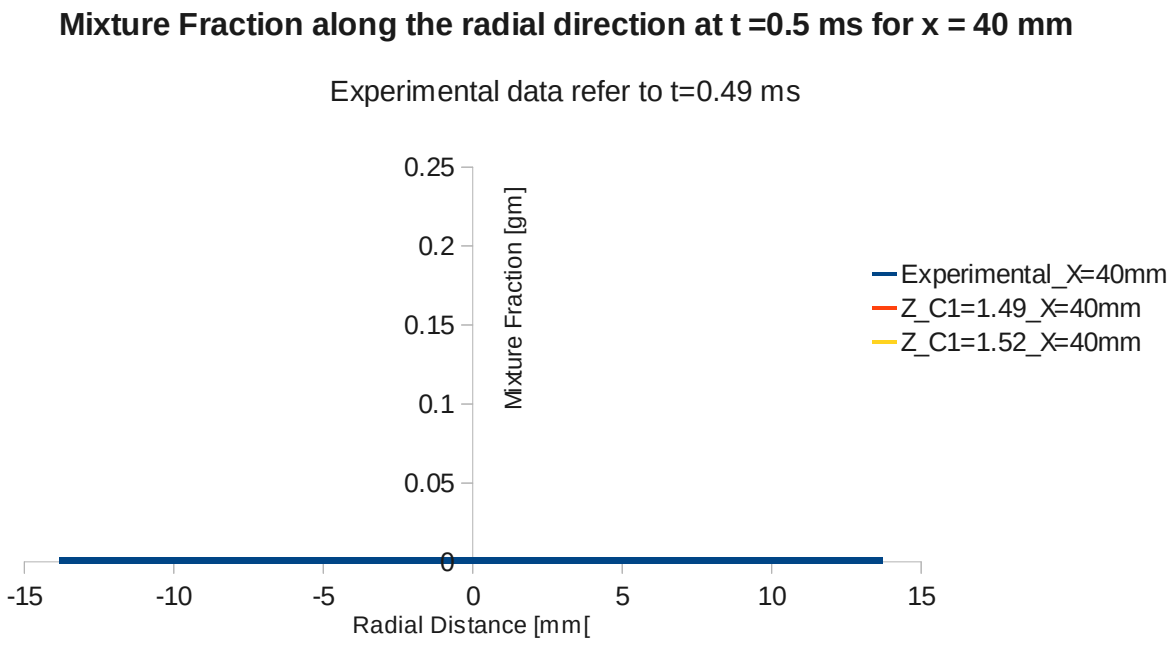

(C)

Figure A2.1: Radial Mass fraction comparison at time t = 0.5 ms for a distance of (A) X = 20 mm (B) X = 30 mm (C) X = 40 mm

A 2.2: At Time, t = 0.7 ms

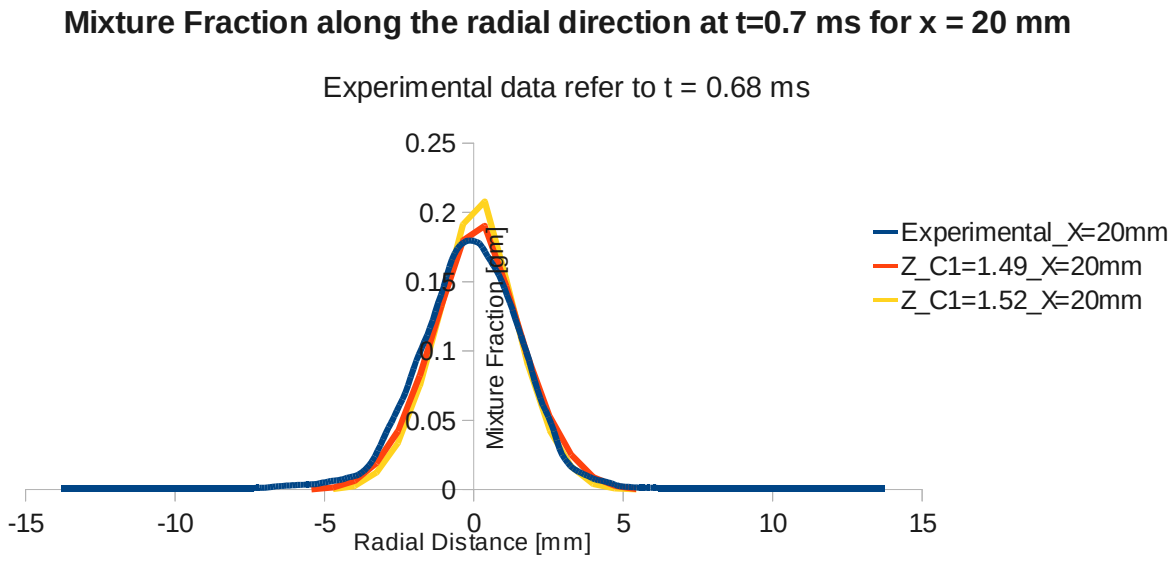

(A)

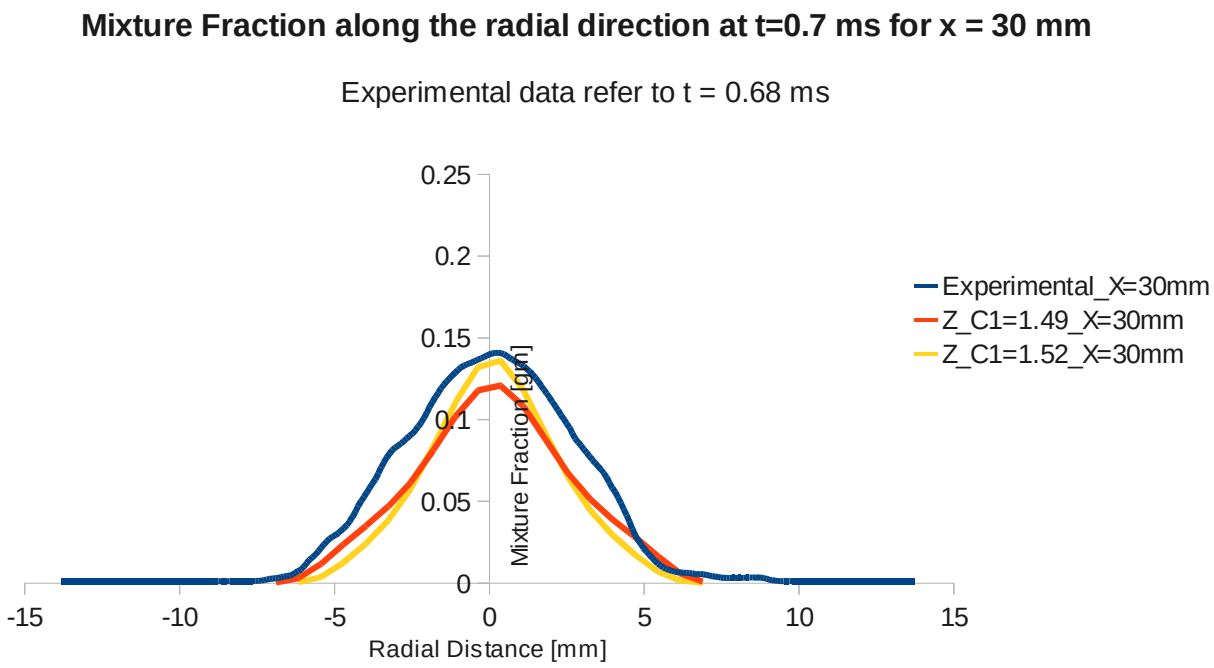
Mixture Fraction along the radial direction at t=0.7 ms for x = 30 mm
Experimental data refer to t = 0.68 ms
0.25
0.2
0.15
0.1
0.05
0
Mixture Fraction [gm]
-15
-10
-5
0
5
10
15
Radial Distance [mm]
Experimental_X=30mm
Z_C1=1.49_X=30mm
Z_C1=1.52_X=30mm

(B)

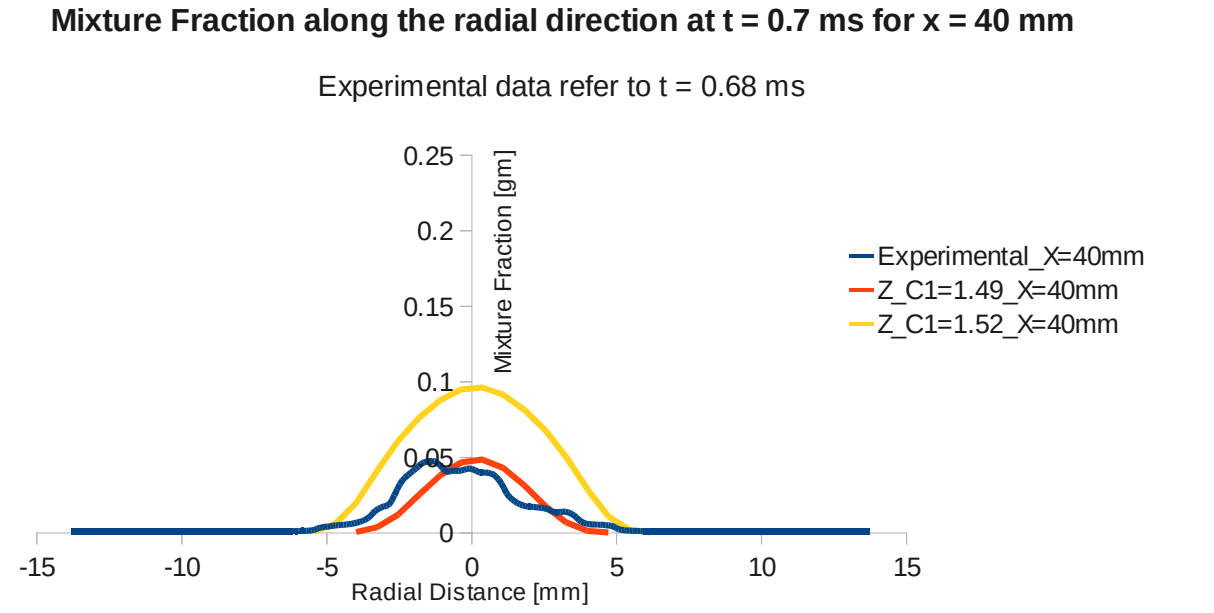
Mixture Fraction along the radial direction at t = 0.7 ms for x = 40 mm
Experimental data refer to t = 0.68 ms
0.25
0.2
0.15
0.1
0.05
0
Mixture Fraction [gm]
-15
-10
-5
0
5
10
15
Radial Distance [mm]
Experimental_X=40mm
Z_C1=1.49_X=40mm
Z_C1=1.52_X=40mm

(C)

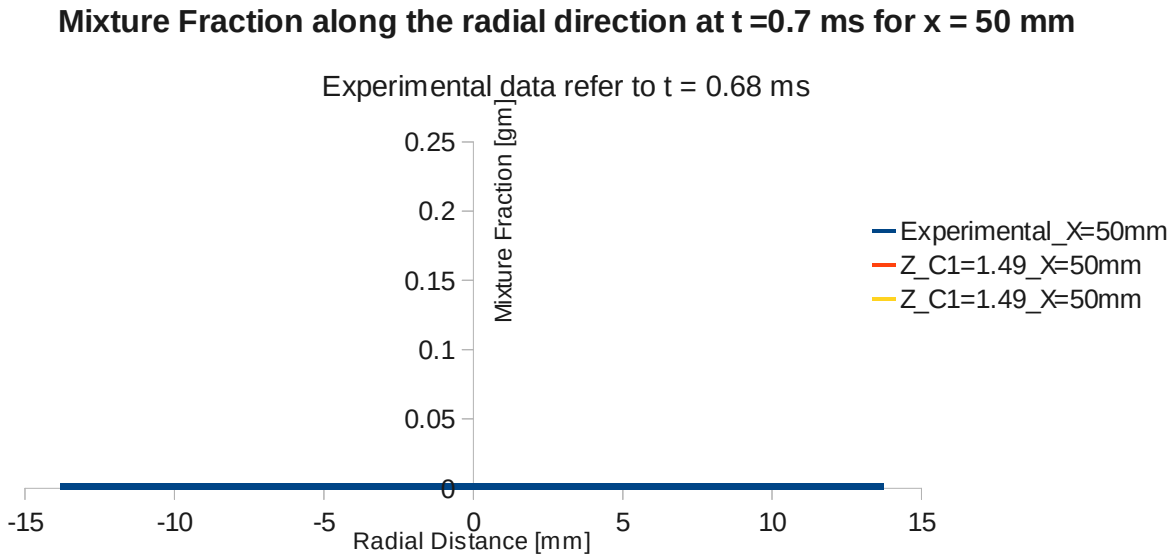

(D)

Figure A2.2 : Radial Mass fraction comparison at time t = 0.7 ms for a distance of (A) X = 20 mm (B) X = 30 mm (C) X = 40 mm (D) X = 50 mm

A2.3: At time, t = 0.9 ms:

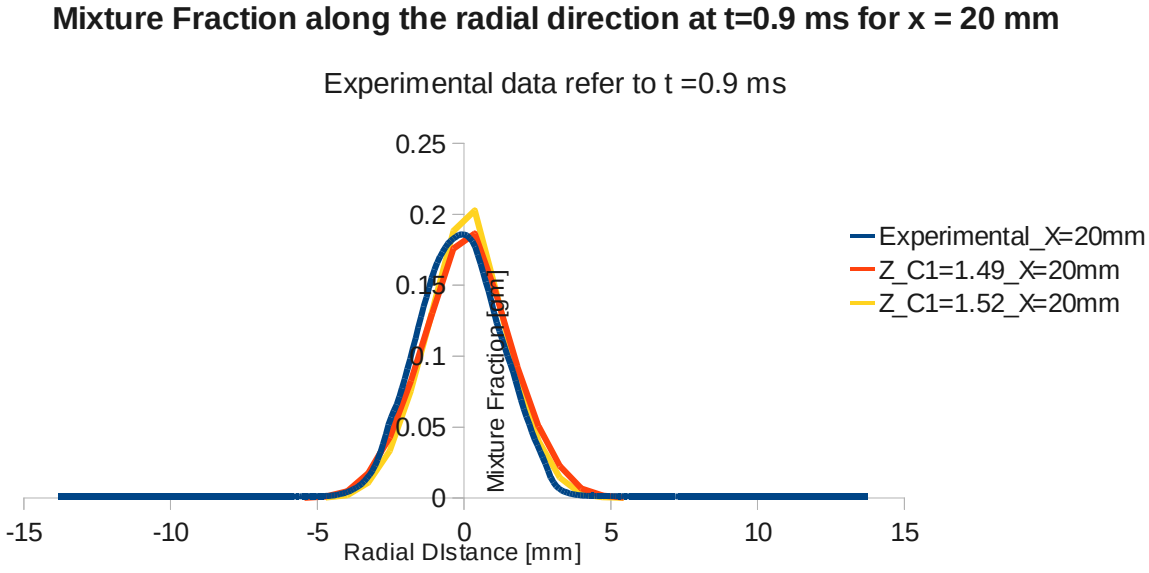

(A)

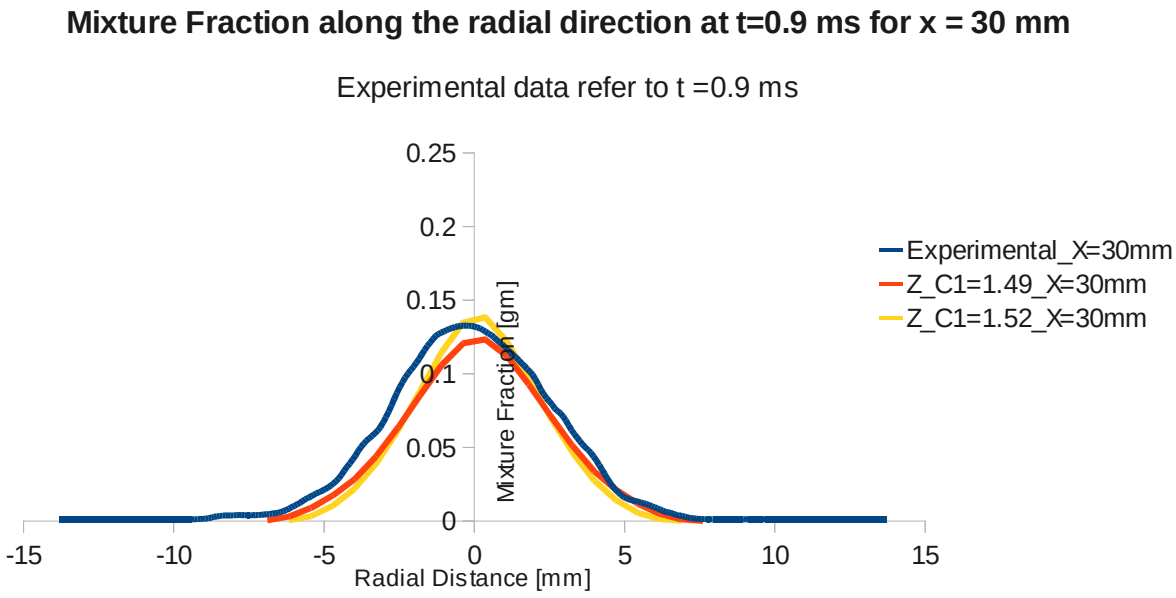
Mixture Fraction along the radial direction at t=0.9 ms for x = 30 mm
Experimental data refer to t =0.9 ms
0.25
0.2
0.15
0.1
0.05
0
Mixture Fraction [gm]
-15
-10
-5
0
5
10
15
Radial Distance [mm]
Experimental_X=30mm
Z_C1=1.49_X=30mm
Z_C1=1.52_X=30mm

(B)

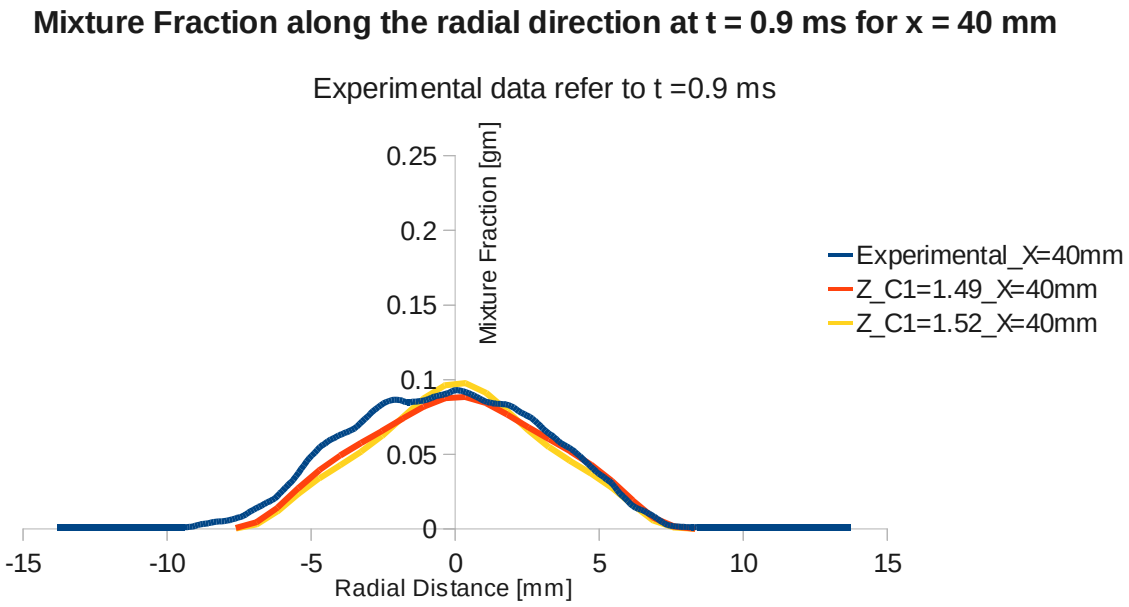
Mixture Fraction along the radial direction at t = 0.9 ms for x = 40 mm
Experimental data refer to t =0.9 ms
0.25
0.2
0.15
0.1
0.05
0
Mixture Fraction [gm]
-15
-10
-5
0
5
10
15
Radial Distance [mm]
Experimental_X=40mm
Z_C1=1.49_X=40mm
Z_C1=1.52_X=40mm

(C)

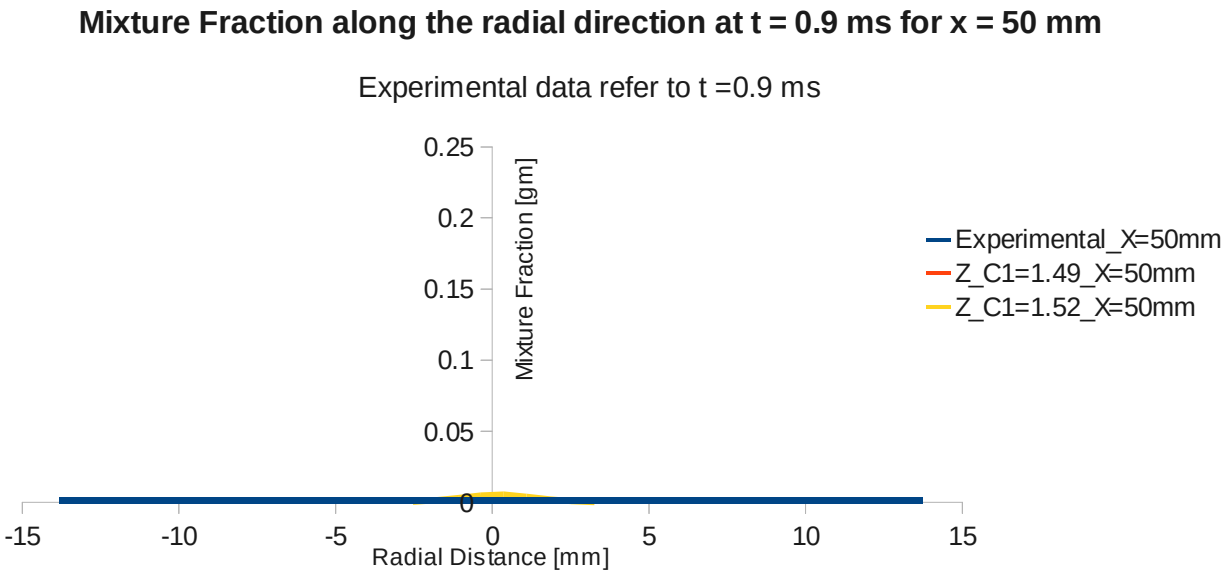

(D)

Figure A2.3: Radial Mass fraction comparison at time t = 0.9 ms for a distance of (A) X = 20 mm (B) X = 30 mm (C) X = 40 mm (D) X = 50 mm

A 2.4:At time, t = 1.15

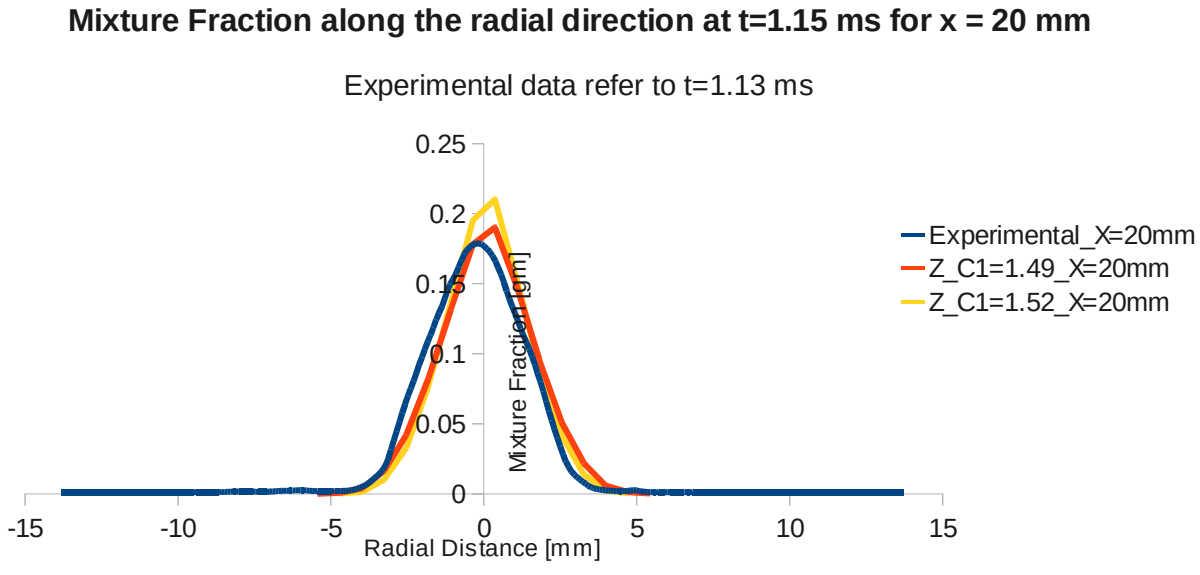

(A)

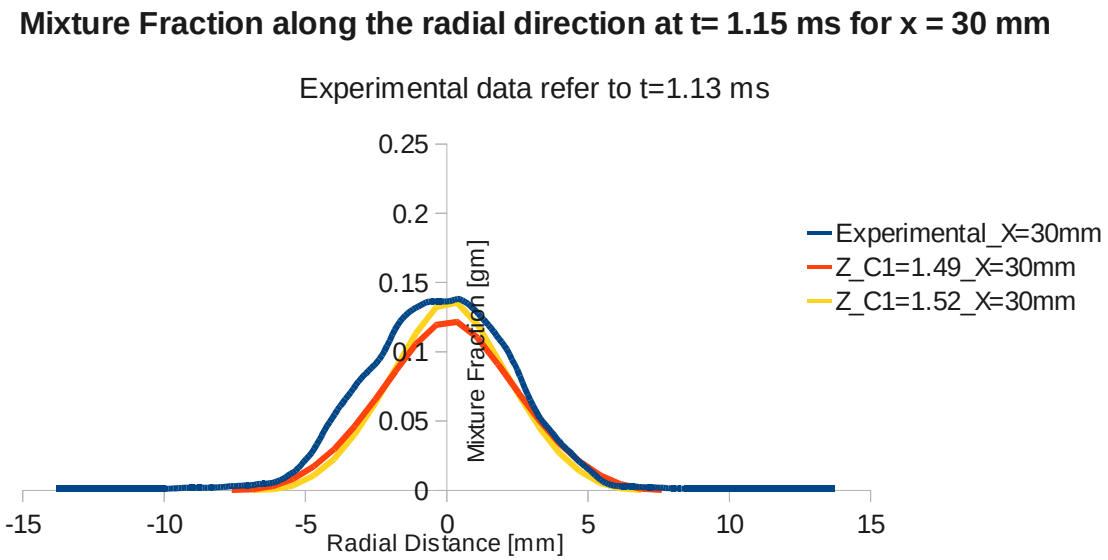
Mixture Fraction along the radial direction at t= 1.15 ms for x = 30 mm
Experimental data refer to t=1.13 ms
0.25
0.2
0.15
0.1
0.05
0
Mixture Fraction [gm]
-15
-10
-5
0
5
10
15
Radial Distance [mm]
Experimental_X=30mm
Z_C1=1.49_X=30mm
Z_C1=1.52_X=30mm

(B)

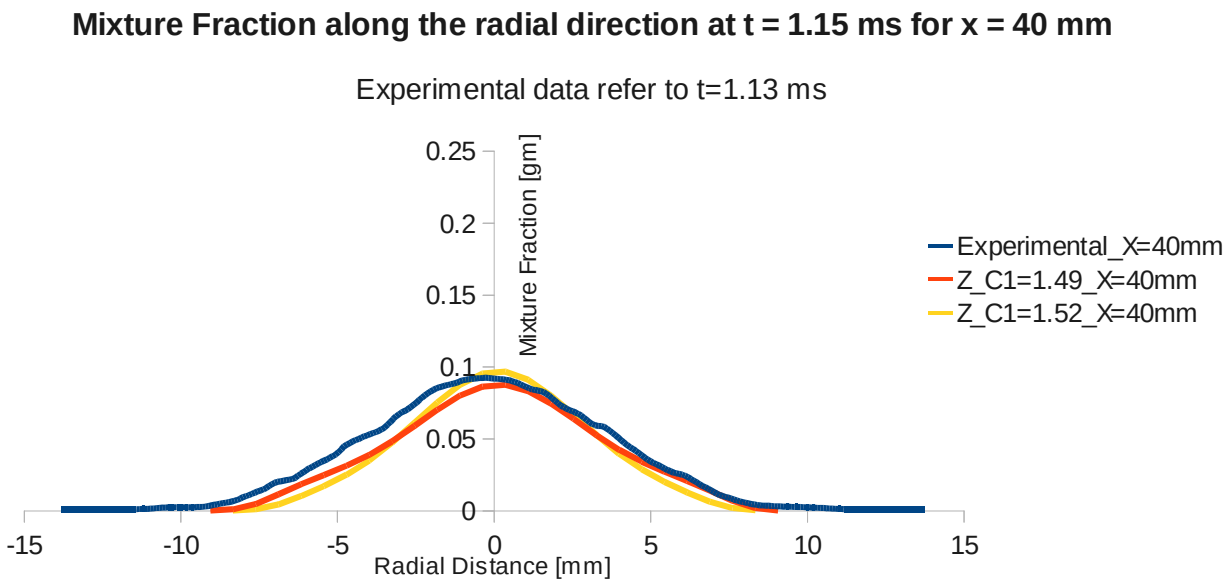
Mixture Fraction along the radial direction at t = 1.15 ms for x = 40 mm
Experimental data refer to t=1.13 ms
0.25
0.2
0.15
0.1
0.05
0
Mixture Fraction [gm]
-15
-10
-5
0
5
10
15
Radial Distance [mm]
Experimental_X=40mm
Z_C1=1.49_X=40mm
Z_C1=1.52_X=40mm

(C)

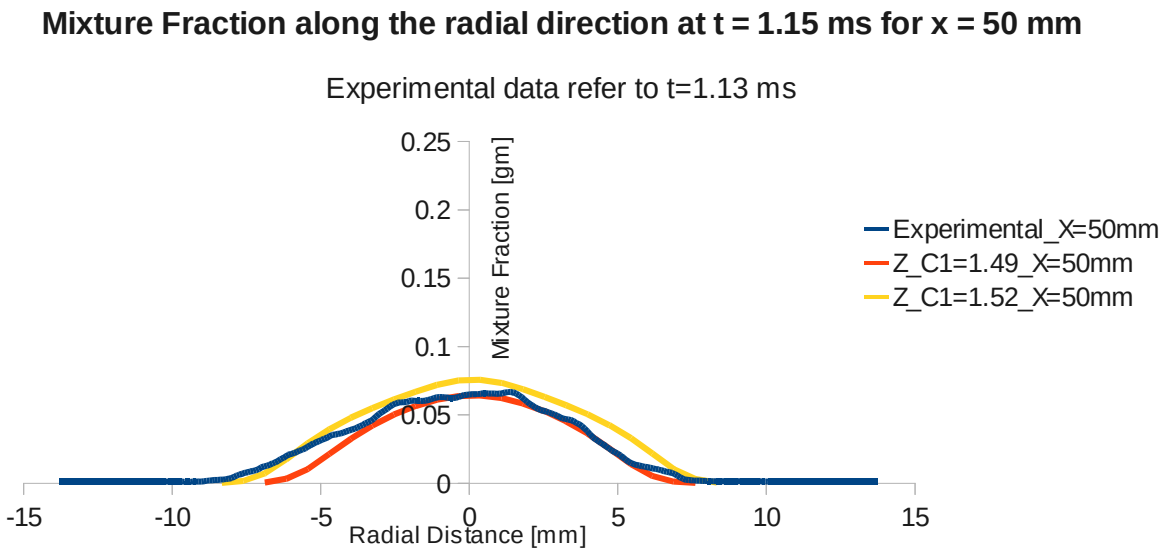

(D)

Figure A2.4:: Radial Mass fraction comparison at time t = 1.15 ms for a distance of (A) X = 20 mm (B) X = 30 mm (C) X = 40 mm (D) X = 50 mm

B: Specifications for Spray-A: Operating Condition of the Engine Combustion Network

Ambient gas temperature	900 K
Ambient gas pressure	near 6.0 MPa
Ambient gas density	22.8 kg/m^3
Ambient gas oxygen (by volume)	15% O_2 (reacting); 0% O_2 (non-reacting).
Ambient gas velocity	Near-quiescent, less than 1 m/s
Common rail fuel injector	Bosch solenoid-activated, generation 2.4
Fuel injector nominal nozzle outlet diameter	0.090 mm
Nozzle K factor	K = (d_{inlet} - d_{outlet})/10 [use µm] = 1.5
Nozzle shaping	Hydro-eroded
Mini-sac volume	0.2 mm^3
Discharge coefficient	C_d = 0.86, using 10 MPa pressure drop and diesel fuel
Number of holes	1 (single hole)
Orifice orientation	Axial (0° full included angle)
Fuel injection pressure	150 MPa (1500 bar), prior to start of injection
Fuel	n-dodecane
Fuel temperature at nozzle	363 K (90°C)
Common rail	GM Part number 97303659. Used by 2005-2006 Duramax engines.
Common rail volume/length	22 cm^3/28 cm
Distance from injector inlet to common rail	24 cm
Tubing inside and oustide diameters	Inside: 2.4 mm. Outside: 6-6.4 mm.
Fuel pressure measurement	7 cm from injector inlet / 24 cm from nozzle
Injection duration	1.5 ms
Injection mass	3.5 - 3.7 mg
Approximate injector driver current	18 A for 0.45 ms ramp, 12 A for 0.345 ms hold

BIBLIOGRAPHY

[1] LEFEBVRE, G. (1989). “Atomization and Sprays”. Hemisphere Publishing Corporation, New York, ISBN 0-89116-603-3.

[2] REITZ, R. D. (1987). “Modeling atomization processes in high-pressure vaporizing sprays”. Atomization and Spray Technology, vol. 3, pp. 309-337.

[3] SIRIGNANO, W. A. (1999). “Fluid dynamics and transport of droplets and sprays”. Cambridge University Press, Cambridge.

[4] PILCH, M., ERDMANN C. A. (1987). “Use of breakup time data and velocity history data to predict the maximum size of stable fragments”. International Journal of Multiphase Flow, vol. 13, Nr.6, pp. 741-757.

[5] LEFEBVRE, ARTHUR HENRY (1989). “Atomization and Sprays”. ISBN 987-0-89116-603-0. OCLC 18560155. New York and Washington, D.C.: Hemisphere Publishing Corp.

[6] OHNESORGE, W (1936). "Formation of drops by nozzles and the breakup of liquid jets". Journal of Applied Mathematics and Mechanics 16: 355–358.

[7] REITZ, R. D. (1978). “Atomization and other breakup regimes of a liquid jet”. Ph.D. Thesis; Mechanical and Aerospace Department, Princeton University, Princeton, NJ, USA.

[8] BAUMGARTEN, C. (1996). “Mixture Formation in Internal Combustion Engines”. ISBN -10 3-540-30835 -0 Springer-Verlag Berlin Heidelberg New York.

[9] TORDA TP (1973). “Evaporation of Drops and Breakup of Sprays”. Astronautica Acta, vol 18, p 383.

[10] HIROYASU H, ARAI M (1990). “Structures of Fuel Sprays in Diesel Engines”. SAE-paper 900475.

[11] RAYLEIGH LORD FRS (1878). “On the Stability of Liquid Jets”. Proc. of the Royal Society London.

[12] YUEN MC (1968). “Non-linear Capillary Instability of a Liquid Jet”. J Fluid Mech, vol 33, p 151.

[13] NAYFEY AH (1968). “Nonlinear Stability of a Liquid Jet” . Physics of Fluids, vol 13, no 4, pp 841–847.

[14] RUTLAND DF JAMESON GJ (1970). “Theoretical Prediction of the Size of Drops Formed in the Breakup of Capillary Jets”. Chem Eng Science, vol 25, p 1689.

[15] REITZ RD, BRACCO FV (1986). “Mechanisms of Breakup of Round Liquid Jets”. In

Enzyclopedia of Fluid Mechanics, Gulf Pub, NJ, 3, pp 233–249.

[16] SCHNEIDER, B. M. (2003). “Experimentelle Untersuchung zur Spraystruktur in transparenten, verdampfenden und nicht verdampfenden Brennstoffstrahlen unter Hochdruck”. Ph.D. Thesis, Eidgenössische Technische Hochschule Zürich.

[17] KADOCSA A. (2007). “Modeling of Spray Formation in Diesel Engine”. Ph.D. Thesis, Budapest University of Technology and Economics.

[18] FAETH, G. M., HSIANG, L.-P., WU, P.-K. (1995). “Structure and break-up properties of sprays”. International Journal of Multiphase Flow, Suppl. Pp 99-127.

[19] BAYVEL, L., ORZECHOWSKI, Z. (1993). “Liquid atomization”. Taylor & Francis, London, ISBN 0-89116-959-8.

[20] LIU, A. B., MATHER, D., REITZ, R. D. (1993). “Modeling the effect of droplet drag and breakup on fuel spray”. SAE Technical Papers Series, 930072.

[21] LIU, A. B., REITZ, R. D. (1993). “Mechanisms of air-assisted liquid atomization”. Atomization and Spray, vol. 3, pp. 55-75.

[22] WIERZBA A (1993). “Deformation and Breakup of Liquid Drops in a Gas Stream at Nearly Critical Weber Numbers”. Experiments in Fluids, vol 9, pp 59–64.

[23] KRZECZKOWSKI SA (1980). “Measurement of Liquid Droplet Disintegration Mechanisms”. Int J Multiphase Flow, vol 6, pp 227–239.

[24] ARCOUMANIS C, GAVAISES M, FRENCH B (1997). “Effect of Fuel Injection Process on the Structure of Diesel Sprays”. SAE paper 970799.

[25] X. JIANG, G.A. SIAMAS, K. JAGUS, T.G. KARAYIANNIS (2009). “Physical modelling and advanced simulations of gasliquid two-phase jet flows in atomization and sprays”. International Journal of Progress in Energy and Combustion Science 36 (2010) 131-167.

[26] STEGEMANN J, SEEBODE J, BALTES J, BAUMGARTEN C, MERKER GP (2002). “Influence of Throttle Effects at the Needle Seat on the Spray Characteristics of a Multihole Injection Nozzle”. ILASS-Europe 2002, Zaragoza, Spain.

[27] HOMBURG A (2002). “Optische Untersuchungen zur Strahlausbreitung und Gemischbildung beim DI-Benzin- rennverfahren”. Ph.D. Thesis, University of Braunschweig, Germany.

[28] GINDELE J (2001). “Untersuchung zur Ladungsbewegung und Gemischbildung im Ottomotor mit Direkteinspritzung”. Ph.D. Thesis, University of Karlsruhe, Germany, Logos- Verlag, Berlin, ISBN 3-89722-727-4.

[29] REITZ RD, DIWAKAR R (1987). “Structure of High-Pressure Fuel Sprays”. SAE-paper 870598.

[30] SCHUGGER C, MEINGAST U, RENZ U (2000). “Time-Resolved Velocity Measurements in the Primary Breakup Zone of a High Pressure Diesel Injection Nozzle”. ILASS Europe 2000.

[31] WALTHER J, SCHALLER JK, WIRTH R, TROPEA C (2000). “Characterization of Cavitating Flow Fields in Transparent Diesel Injection Nozzles using Fluorescent Particle Image Velocimetry (FPIV)”. ILASS Europe 2000.

[32] MEINGAST U, REICHELT L, RENZ U, MÜLLER D HEINE B (2000). “Nozzle Exit Velocity Measurements at a Multi-Orifice CR-Nozzle”. ILASS Europe 2000.

[33] HIROYASU H, ARAI M (1990). “Structures of Fuel Sprays in Diesel Engines”. SAE-paper 900475.

[34] KUENSBERG SARRE C, KONG SC, REITZ RD (1999). “Modeling the Effects of Injector Nozzle Geometry on Diesel Sprays”. SAE-paper 1999-01-0912.

[35] NURICK WH (1976). “Orifice Cavitation and its Effect on Spray Mixing”. Journal of Fluids Engineering, 98, pp. 681–687.

[36] REINHARD TATSCHL, CHRISTOPHER V. KÜNSBERG SARRE AND EBERHARD V. BERG (2002). “IC-Engine Spray Modeling – Status And Outlook”. International Multidimensional Engine Modeling User’s Group Meeting at the SAE Congress 2002.

[37] V. KÜNSBERG SARRE, CH., TATSCHL, R. (1998). “Spray Modelling / Atomisation – Current Status of Break-Up Models”. ImechE Seminar on Turbulent Combustion of Gaseous and Liquids, Lincoln.

[38] HUH KY, GOSMAN AD (1991). “A Phenomenological Model of Diesel Spray Atomization”. Proc Int Conf on Multiphase Flows ’91, Tsukuba, Japan.

[39] NISHIMURA A., ASSANIS DN (2000). “A Model for Primary Diesel Fuel Atomization Based on Cavitation Bubble Collapse Energy”. 8th Int Conf on Liquid Atomization and Spray Systems (ICLASS), pp 1249–1256.

[40] RICART LM, XIN J, BOWER GR, REITZ RD (1997). “In-Cylinder Measurement and Modeling of Liquid Spray Penetration in a Heavy-Duty Diesel Engine”. SAE-paper 971591.

[41] PATTERSON MA, REITZ RD (1998). “Modelling the Effect of Fuel Spray Characteristics on Diesel Engine Combustion and Emission”. SAE-Paper 980131.

[42] HWANG SS, LIU Z, REITZ RD (1996). “Breakup Mechanisms and Drag Coefficients of High-Speed Vaporizing Liquid Drops”. Atomization and Sprays, vol 6, pp 353–376.

[43] TAYLOR GI (1963). “The Instability of Liquid Surfaces when Accelerated in a Direction Perpendicular to their Planes”. In Batchelor GK (1963) The Scientific Papers of Sir Geoffery Ingram Taylor. vol 3, pp 532–536, Cambridge University Press.

[44] CHANG SK (1991). “Hydrodynamics in Liquid Jet Sprays”. Ph D Thesis, University of Wisconsin-Madison.

[45] BELLMAN R, PENNINGTON RH (1954). “Effects of Surface Tension and Viscosity on Taylor Instability”. Quarterly of Applied Mathematics, 12, pp 151–162.

[46] SU TF, PATTERSON M, REITZ RD (1996). “Experimental and Numerical Studies of High Pressure Multiple Injection Sprays”. SAE-paper 960861.

[47] G. D’ERRICO, T. LUCCHINI (2011). “Validation of spray and combustion models for Diesel engines using constant-volume experiments”. ILASS-Americas 23rd Annual Conference on Liquid Atomization and Spray Systems, Ventura, CA.

[48] http://www.openfoam.org

[49] http://www.sandia.gov/ecn/index.php

[50] http://crf.sandia.gov/

[51] R. NOVELLA , A. GARCÃA, J.M. PASTOR, V. DOMENECH (2011). “The role of detailed chemical kinetics on CFD diesel spray ignition and combustion modelling”. Mathematical and Computer Modelling 54 (2011) journal 1706–1719.

[52] J. DUKOWICZ, (1980). “A particle-fluid numerical model for liquid sprays”. Journal of Computational Physics 35 (2) 229–253.

[53] IDICHERIA, C. A., PICKETT, L. M., (2007). “Effects of EGR on Diesel Premixed-Burn Equivalence Ratio”. Proceedings of the Combustion Institute 31, 2931-2938.

[54] PICKETT, L.M., MANIN, J., GENZALE, C.L., SIEBERS, D.L., MUSCULUS, M.P.B., IDICHERIA, C.A. (2011). “Relationship between diesel fuel spray vapor penetration/dispersion and local fuel mixture fraction”. SAE Paper 2011-01-0686.

----------X----------